An investigation into the deformation of direct metal laser sintered parts

A Olwagen
13073133

Dissertation submitted in partial fulfilment of the requirements for the degree *Magister* in Mechanical Engineering at the Potchefstroom Campus of the North-West University

Supervisor: Prof J Markgraaff

May 2015

ABSTRACT

Direct Metal Laser Sintering (DMLS) is a rapid prototyping technique that allows for direct and rapid manufacturing of complex components. DMLS is however an intricate process and the quality of the final product is influenced by multiple manufacturing parameters (or DMLS settings) and powder characteristics. The effect which each of these manufacturing parameters and powder characteristics has on the final parts is not well understood and the success of process manufacturing mainly relies on empirical knowledge. Consequently high dimensional deformation and relatively poor mechanical properties are still experienced in many DMLS products, in particular in copper-based laser sintered parts.

A need therefore exists to systematically examine the effect of process parameters on the quality of final parts in order to determine the most appropriate manufacturing parameters for specific applications of copper-based laser sintered parts.

This document summarises the effect of different process parameters on the quality of Direct Metal 20 laser sintered parts produced with a EOSINT M250 Xtended laser sintering machine from powder consisting of Ni5Cu, Cu15Sn – Cu5Sn and Cu8P – Cu2P material grains.
The quality of the sintered parts is defined in terms of the microstructures, porosities and dimensional deformations obtained.

The effects of three different geometric sintering strategies currently in standard use namely *Solid Skin*, *Skin Stripes* and *Skin Chess* were examined, and the more appropriate process parameters and scanning technique for the available set-up is presented.

Keywords: *Direct Metal Laser Sintering, porosity, dimensional deformation, manufacturing parameters*

ACKNOWLEDGEMENTS

I want to give all praise and glory to my Heavenly Father who blessed me with the intelligence and perseverance to complete this study.

Thank you to my study leader and mentor, Professor Johan Markgraaff that set aside many Fridays to patiently give me guidance and often much needed encouragement.

To my dear husband and loving son, thank you for your patience when this study demanded much of our family time. Thank you for your support and joyful laughs that brightened my every hard-worked day.

A special word of thank you to the following people that allowed me to make use of their equipment and facilities and assisted me in completing this study without any funding:

Gerrie Booysen at the Centre for Rapid Prototyping (CRPM), Central University of Technology

Melanie Smit at Mintek's Analytical Services and

Freddie Roelofse at the University of the Free State's Department of Geology.

Lastly, I want to thank my family and friends who always encouraged me and showed interest in my studies.

TABLE OF CONTENTS

LIST OF FIGURES

LIST OF TABLES

ABBREVIATIONS

BET	-	Brunauer, Emmett and Teller, 1938
BH	-	Brinell Hardness
BSE	-	Backscatter Electron
CAD	-	Computer Aided Design
CMM	-	Coordinate Measuring Machine
CRPM	-	Centre for Rapid Prototyping
CUT	-	Central University of Technology
cm^3/g	-	cubic centimetre per gram
CO_2	-	Carbon Dioxide
Cu	-	Copper
Cu_3P	-	Copper phosphate
DMLS	-	Direct Metal Laser Sintering
DLS	-	Direct Laser Sintering
DM 20	-	Direct Metal 20
EDS	-	Energy Dispersive System
FE	-	Finite Element
FEA	-	Finite Element Analysis
$FeCl_3$	-	Iron Chloride
FEM	-	Finite Element Method
HCl	-	Hydrochloric acid
HRB	-	Rockwell B hardness measurement
HV	-	Vickers hardness measurement
kV	-	Kilo Volt
mm/s	-	Millimetre per second
m^2/g	-	Square meters per gram
Ni	-	Nickel
nm	-	Nanometre
NS	-	Near Spherical
P	-	Phosphorus
Pd	-	Pore diameter
ppm	-	Parts per million
P_2O_5	-	Phosphorus pentoxide

PV	-	Pore volume
rpm	-	Revolutions per minute
SA	-	Surface Area
SEM	-	Scanning Electron Microscope
SLS	-	Selective Laser Sintering
Sn	-	Tin
W	-	Watt
XRF	-	X-ray Fluorescence
2D	-	Two Dimensional
3D	-	Three Dimensional
µm	-	micrometre

LIST OF SYMBOLS

η	-	Energy density by volume
P	-	Power
v	-	Laser scan speed
h	-	Scan line spacing
d	-	Layer Thickness
%	-	Percentage

CHAPTER 1: INTRODUCTION

1.1 BACKGROUND

Direct Metal Laser Sintering (DMLS) is a rapid prototyping process that utilises of a focused laser beam to build three dimensional (3D) components directly from computer aided design (CAD) data. Prior to the manufacturing process, computer software is used to slice a 3D CAD model of the prototype into thin layers of a few micrometres thickness (EOS, 2007a). During manufacturing the first thin layer of metal powder is distributed over a building platform, where after the laser follows the profile of the applicable computer layer and sinters the metal powder into a solid layer through the process of liquid phase sintering. The second layer of powder is then distributed and fused onto the first layer. The process is repeated until the final 3D model is manufactured. This technique allows for the direct manufacturing of complex metal components while ensuring minimum material wastage and machining. Although this method of manufacturing was originally used to manufacture prototypes, the modern aim is to produce functional components with high accuracy, good surface quality and mechanical properties for a broad range of applications required in modern manufacturing (Ning *et al., 2005).*

Copper-based material powders are attractive for this manufacturing purpose, in particular, and are often used in injection moulding tooling and inserts as it has good thermal conductivity and mechanical properties and is relatively low in cost (Zhu *et al.,* 2005).

The dimensional accuracy of direct laser sintered (DLS) parts is, however, still inferior to conventional shaped parts because high dimensional deformation is experienced over a wide range of DLS powders varying from plastic (Senthilkumaran *et al.*, 2009) to ceramics and metals such as iron (Simchi, 2006) and Cu-based powders (Gu *et al.*, 2007, Zhu *et al.,* 2005, Tang et al., 2003 and Ning *et al., 2005*).

Due to the complexity of the DLS process the accuracy and attributes of the sintered part is dependent on multiple variable process parameters, the detail of which is not readily available in open literature for different manufactured machine systems. The effect of these process parameters is not well understood and the accuracy of the sintered parts often depends on the experience of the machine operator (Simchi, 2006 and Senthilkumaran *et al.*, 2009) who is sometimes forced to run several trials of a part to obtain the required dimensions or is left to settle for a part with dimensions that vary somewhat from the desired CAD model.

1.2 PROBLEM STATEMENT

For certain machine systems dimensional deformation of Cu-based DLS parts has been improved through empirical knowledge and post processing techniques of the green sintered parts. This is, however, often obtained through compromising some of the parts' mechanical properties as the effect that each of the different scanning parameters has on the density and deformation of sintered parts is not well understood. The effect of different sintering strategies (comprising of variable process parameters) on the quality of the final sintered parts has only partially been investigated, in particular the reasons for the dimensional deformation in Cu-based DLS parts.

1.3 AIM

The aim of this study is to verify and characterise the material powder used for sintering, as well as to understand the operation of the direct laser sintering process; in particular what effect the different sintering scanning parameters may have on deformation of a sintered part. It is the aim that a correlation be made between the deformation and the material characteristics of the green sintered part manufactured through different scanning strategies currently in standard use at the Centre for Rapid Prototyping and Manufacturing (CRPM) at the Central University of Technology (CUT). Based on the deformation and material characteristics, the best of three different scanning strategies will be selected.

CHAPTER 2: LITERATURE REVIEW

2.1 SINTERING

Sintering is a method used to create objects from powders. Generally sintering is defined as a process whereby a powder or compact is held in a mould and heated in a controlled-atmosphere to a temperature below the melting point of the main constituent but to a temperature high enough to allow bonding of the individual particles. It is stated that the sintering mechanisms are complex and dependent on material variables as well as processing parameters (Kalpakjian & Schmid, 2006; Ma & Lim, 2002; Kang, 2005).

The main process parameters are the sintering temperature, sintering time, pressure and the atmosphere in which the sintering is done (Kumar, 2009; Kalpakjian & Schmid, 2006; Kang, SJL, 2005). The sintering temperature is dependent on the material variables and is normally in the range of 60 to 90% of the melting point of the particular metal or alloy (Kumar, 2009; Kalpakjian & Schmid, 2006) while sintering times can vary from a minimum of about 10 minutes for copper alloys to about 8 hours for tungsten (Kalpakjian & Schmid, 2006). An oxygen-free sintering atmosphere is important in order to prevent oxidation of the powder particles during sintering. Protective gasses most commonly used to prevent oxidation during sintering are hydrogen, burned ammonia, partially combusted hydrocarbon gases and nitrogen (Kalpakjian & Schmid, 2006).

The major material variables are the chemical compositions of the powders, the powder particles' shape, particle size and size distribution as well as the degree of powder agglomeration and homogeneity of powder mixture.

At the sintering temperature neighbouring particles begin to weld together through atomic diffusion, leading to an increase in the compact's strength, density and ductility. The increase in density leads to shrinkage, which can lead to unacceptable dimensional changes (Kumar, 2009).

Sintered tin-bronze in particular, is frequently used as a material for self-lubricating bearings and filters as the porosity allows lubricants to flow through it or remain captured within it (ASM International, 1995).

2.2 DIRECT METAL LASER SINTERING PROCESS

A laser sintering machine uses a focused laser beam to build 3D models directly from CAD data. At the start of the DMLS process the building platform is heated and a thin layer of metal powder is distributed evenly over the metal building platform by means of a re-coater blade. The layer gets exposed to a computer-controlled laser beam which first exposes the contours of the current layer based on the part data given and then the enclosed areas. A metallurgical joint between the steel platform and the first layer of the model to be built is formed at the first exposure. A second layer of metal powder is then applied and exposed to the laser beam and this process is repeated layer by layer until the final product is produced (EOS, 2007b).

Liquid phase sintering is one of the processes used by the laser sintering machines to build 3D parts layer by layer through the exposure of metal powders to the focused laser beam. If the material powder consists of different components (compounds or pure metals) such that one particle has a lower melting point than the other, the particle with the lower melting point (known as the binder) will melt when exposed to the laser beam and surround the higher melting-point particle (structural component) and this process is known as liquid-phase sintering (Kalpakjian & Schmid, 2006 and Gu *et al.,* 2007). Liquid-phase sintering is a complex metallurgical process that is subjective to numerous effects including wetting, viscosity, the flow of liquid, phase changes and in some cases chemical reactions (Zhu *et al*., 2005; Gu *et al.,* 2007).

The laser sintering machine possesses a number of adjustable manufacturing parameters which influence the sintering behaviour of the metal powder on exposure (EOS, 2007b). These include but are not limited to the laser power, wavelength, building speed, powder layer thickness, laser type, laser focus diameter, laser scan overlap and the compressed air supply (Gu *et al*., 2006).

It is generally suggested that the laser power be set at a maximum to obtain the lowest building time possible (EOS, 2007b).

Exposure of a layer of the metal powder to the laser beam usually happens in three steps, namely: 1) exposure of the layer contour, 2) hatching of the inner area and 3) a second exposure of the layer contour. It is allowed that a distinction be made between the *skin* and the *core* of a part. The operator can therefore assign different sintering parameters to the *skin* and the *core* respectively. Typically for metal prototypes in which accuracy is important, but the part strength is not critical, the *skin* would be sintered with high resolution building parameters for good surface finishing and maximum physical properties, while the *core* will be sintered with thicker layers and faster exposure parameters that should result in minimum stresses and most probably more porosity (EOS, 2007b).

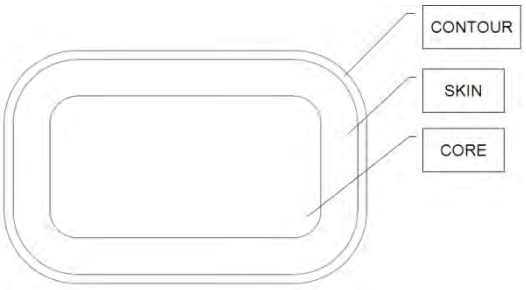

Figure 1: Representation of contour, skin and core of a part

The laser speed of the first contour exposure is usually set to be fairly low to ensure an optimal bond to the layer below while obtaining high mechanical part strength. In an effort to ensure that the contours of the final product correspond exactly to the 3D CAD model, the outside edge of the curing zone must match up with the contour. To avoid that the actual part is bigger than desired, the centre point of the laser is sometimes shifted from the contour to the inside with some distance (EOS, 2007b). Figure 2 illustrates the difference in part size when the centre point of a beam is on the contour and when it is offset with some distance from the contour to the inside. When no beam offset is applied, the actual part will be bigger than intended.

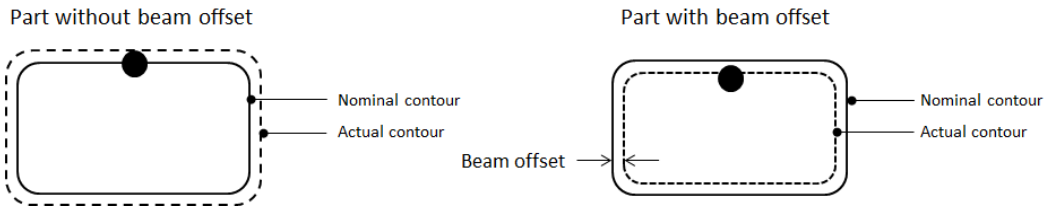

Figure 2: Illustration of part geometry without beam offset compensation compared to when beam offset compensation is applied (modified from EOS, 2007)

After the contour exposure, a solidified layer is produced in the inner area (*core*). The laser beam moves along parallel paths, line after line across the inner area. To ensure that the laser does not overshoot the contour, beam offset compensation is applied to the laser at the end paths. This is supposed to ensure that the edge of the laser's curing zone is on the edge of the contour (see Figure 3 for illustration). During hatching of the inner area, the laser energy is kept constant and it is advised that the scan speed is high while the distance between parallel scan lines can be set to about one quarter of the laser focus diameter, but this value can be varied. By making the distance between the laser scan lines smaller than the focus diameter, the laser beam will move several times across a point to be exposed and therefore the local temperature will be kept at higher levels for longer, and this is supposed to guarantee that complete sintering is attained (EOS, 2007b).

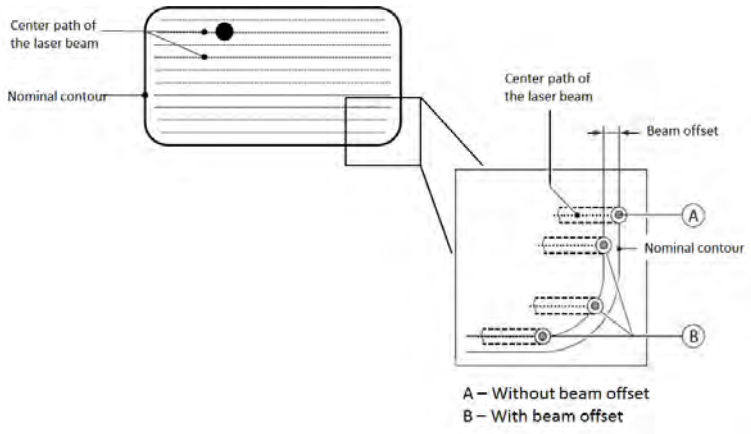

Figure 3: Illustration of beam offset applied to the laser path (modified from EOS, 2007b)

Mainly four exposure types exist for the hatching of the inner area. These exposure types are named *Skywriting*, *Stripes*, *Squares* and *Chess* and are explained in APPENDIX A. For all of the exposure types, one can define if

every layer should be exposed in that manner or what number of layers should be skipped before repetition of an exposure type (EOS, 2007b).

After sintering of the inner area, a second exposure of the part outline (*contour*) is carried out. The focal point of the laser is set exactly on the edge of the layer according to the CAD data. This should result in sharper part contours and more accurate parts (EOS, 2007b).

2.3 DMLS MATERIAL

The material powders used for laser sintering can vary from polymer and ceramic powders to steel-based and copper-based metal powders and titanium alloys. The attributes of the powder medium used for sintering can have a major influence on the sintering activity, densification during laser sintering and the porosity of the final sintered part. These attributes include the particle size distribution and shape, the powder surface morphology as well as other powder characteristics that are dependent on the powder production technique (Neikov *et al*., 2009 and Simchi *et al.,* 2003).

DLS powders usually consist of very fine grains for the reason that the surface energy driving force that initiate bond growth is much higher for finer powder particles than for coarser ones and therefore lower sintering temperatures are required for sintering of finer powders (Neikov *et al.,* 2009). EOS (2007c) stated that as a result of the higher surface area, finer powders are suitable for wide ranges of process parameters and manufacturing speeds which can result in varieties of mechanical properties. Although it has been suggested that mono-sized powders are preferred in producing dense, uniform, fine-grained structures, most powders possess certain size distributions, both to enhance sintering and to minimise overall shrinkage (Ma & Lim, 2002). In general it is thought that a broader particle size distribution (when mixing finer and coarser powders) will lead to higher densities in the sintered parts since the finer powders has the ability to penetrate into the gaps between the larger particles. However, Ma and Lim (2002) and Linger and Raj in Kang (2005) determined experimentally on alumina powder and glass spheres, respectively, that better sintering densification, more reliable microstructures

and less shrinkage were obtained with narrow particle size distributions (when smaller size differences exist between the particles) than with mono-sized or broad-sized distributions. In addition, Ma and Lim (2002) stated that agglomerates in the powder medium have a significant influence on the densification of powder compacts and it disguises the effect of particle size distributions. Kang (2005) states that a non-uniform compact density is obtained when powders consisting of agglomerates are sintered and consequently full densification is difficult to achieve because of differential densification during sintering (Kang, 2005).

Experiments by Simchi *et al.* (2003) proved that alloying elements or sintering aids such as carbon or phosphorous can enhance the sintering rate of metal powders and that high-alloy steels have higher densification rates than low-alloy powders when processed under the same conditions. It is said that carbon can be added to a mixture of iron and copper powders in order to decrease the surface tension during laser sintering. Furthermore, Simchi *et al.* (2003) revealed that alloying elements such as nickel and molybdenum can be used to improve the mechanical properties of a mixture of iron and copper powders depending on the application. The addition of the so-called sintering aids is presumably because the solid elements are soluble in the liquid phase causing solid-solution strengthening to take place. The high temperature liquid wets the solid and provides a capillary force that pulls the grains closer to each other and assists with densification. The high temperature softens the solid and causes high diffusion rates associated with faster sintering and lower sintering temperatures (German *et al.,* 2009).

In their studies on a Cu-CuSn-CuP mixed powder Gu *et al.* (2007) explained that the copper (Cu) acts as the structural metal (Gu *et al*., 2007; Tang *et al.,* 2003) while the copper-tin alloy (CuSn) melts completely and acts as the binder. Furthermore, the additive copper-phosphate (CuP) also melts completely and the phosphorus element acts as an *in situ* deoxidizer (Gu *et al.,* 2007) or flux (Tang *et al.,* 2003) by forming P_2O_5 and $CuPO_3$ during the sintering process.

Dai and Shaw (2004) and Tang *et al.* (2003) declared that the degree of dimensional deformation in metal and ceramic powders (Dai and Shaw, 2004) and in copper-based powders (Tang *et al.*, 2003) can be minimized by increasing the initial powder compact density as this would decrease the temperature gradient.

Zhu *et al.* (2005) concluded that an in-plane expansion that compensates for sintering shrinkage can be caused during the sintering process of their Cu-based metal powder. When the binder particle melts, the structural particles fall from on-top to in-between other particles and force the particles outwards (Figure 4).

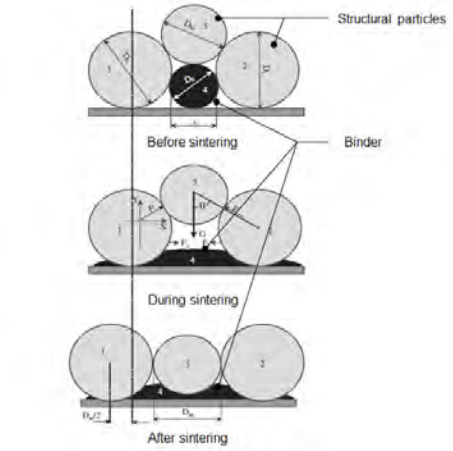

Figure 4: Illustration of in-plane expansion in DMLS (modified from Zhu *et al.* 2005)

2.4 SINTERING PROPERTIES AND PROCESS PARAMETERS

Numerous researchers performed experiments to investigate the effect of process parameters on the properties and qualities of the sintered parts. The effect of laser power, scan spacing, scan speed and layer thickness to the transient temperature and temperature gradient as well as the density, strength, accuracy and surface finish of the final parts were studied. The outcomes of the experiments were found to be generic for all the materials and are summarised and discussed in the paragraphs below.

In studies conducted on different materials which include copper-based alloys, ferrous alloys, composite polystyrene and polycarbonate, it was found that as the scan speed is increased, less energy is absorbed by the powder bed and consequently the transient surface temperature of the powder bed decreases. This in turn results in a decrease of the density and tensile strength of the final parts while the dimensional deformation is reduced (Wang *et* al., 2007; Gu *et al*., 2007; Simchi *et al*., 2003, Dong *et al.,* 2009; Tang *et al*., 2003).

For materials ranging from polystyrene to titanium and copper-based alloys it was found that when the laser power is increased the sintering depth, the transient temperature and the thermal gradient of the powder bed as well as the density of the final part is increased (Gu *et al.,* 2006; Gao *et al*., 2008; Patil & Yadava, 2007). Although the tensile strength is improved with an increase in laser power, the dimensional deformation of the final part is also increased (Wang *et al.,* 2007, Tang *et al.,* 2003) while the surface finish becomes courser (Wang *et al.,* 2007; Dong *et al.,* 2009; Tang *et al.,* 2003; Gao *et al.,* 2008). Gao *et al.* (2008) determined that the effect of laser power on the temperature is more significant than the effect of scanning speed.

The tensile strength and surface finish of the sintered parts are improved when the scan spacing is decreased but the dimensional deformation increases (Wang *et al.,* 2007; Tang *et al.,* 2003). The transient temperature is higher when the scan line spacing is decreased and this results in a rapid change in temperature gradient which can induce more thermal stress in the powder layer (Patil & Yadava, 2007).

When the layer thickness is increased excessively, the adhesion between the single layers becomes weak and the tensile strength, density (EOS, 2007b) and macro hardness (Gu *et al.,* 2006) decrease while the surface finish becomes worse (Tang *et al.,* 2003). According to Simchi (2006) and Wang *et al.* (2007) an increase in layer thickness results in less shrinkage of the polystyrene and ferrous sintered parts while Tang *et al.* (2003) stated that the strength of copper-based alloys decrease with an increase in layer thickness while the accuracy is almost not affected by the layer thickness.

A smaller laser focus diameter will penetrate deeper into the material and therefore the maximum laser intensity, surface temperature of the powder bed and temperature gradient in the material will increase (Dong *et al*., 2009; Patil & Yavada, 2007).

Simchi (2006) summarizes the effects of the process parameters on various ferrous powders in a single term “the energy input”. The laser power, scan rate and scan spacing affect the energy input. A higher laser power, a lower scan rate and decreased line spacing results in higher energy input and the consequence is that higher densities and more dimensional deformation are obtained in the final sintered parts.

Both Simchi (2006) and Dong *et al.* (2009) warned against too high laser energy inputs as this could result in the degradation or delamination of the sintered layer.

Gu *et al.* (2006) defined the factor η, ‘energy density by volume’, to evaluate the combined effect of processing parameters on the copper-based metal powders as follows:

$$\eta = \frac{P}{vhd} \qquad (1)$$

With P the laser power, v the scan speed, h the scan line spacing and d the layer thickness.

As mentioned earlier the exposure of the metal powder to the laser beam can happen through a combination of various sintering strategies. The findings by previous researchers on the effect of these strategies on the quality of the final parts will be presented in the following paragraphs.

The scanning vector length (*l*) can be described as the length of the straight-line sintering path which is followed by the active laser beam before a successive sintering path is created parallel to the first. More energy is absorbed from the neighbouring scan lines when short scanning vector lengths are employed and this should result in stronger and denser (Ning *et*

al., 2005) structures in copper-based materials powders. According to Ning *et al.* (2005) more dimensional deformation is experienced as a consequence of the denser part when short vector lengths are employed while Simchi (2006) states that higher scanning vector lengths can result in increased thermal stresses which result in dimensional deformation and cracks of iron-based powder systems. Contradictory to Ning *et al.* (2005) who suggests that short vector lengths should be avoided as it results in less homogeneous microstructures and more dimensional deformation, Matsumoto *et al.* (2002) and Simchi (2006) suggest that long vector lines should be avoided in nickel-based alloys and iron powders in order to prevent distortion of the solid layer on the powder bed.

Senthilkumaran *et al.* (2009) measured the shrinkage of nylon components manufactured through the hatching strategy only and of components in which contouring and hatching strategies were performed on the same layer. They found that the shrinkage of specimens which were manufactured through the hatching exposure strategy only was fractions less than that of specimens manufactured through the contouring and hatching exposure strategy. In addition, the shrinkage patterns of the parts manufactured through contouring and hatching were more irregular than that of the parts sintered through hatching only. They ascribed this to the contour exposure that constrains the expansion of a layer during the sintering process. Furthermore, the low laser power and high beam speed with which the contours were sintered caused non-uniform shrinkage between the various lengths of specimens.

Senthilkumaran *et al.* (2009) also investigated the effect of part orientation on shrinkage of nylon parts. They discovered that, for the specific machine used, 0.05% - 0.2% more shrinkage occurred in parts orientated along the machine's Y-direction (parallel to re-coater blade) than for the X-direction (perpendicular to re-coater blade). For both orientations the scanning direction was parallel with the parts' longitudinal dimension. According to them this phenomenon is attributed to the variation in thermal gradients in the machine as well as the effect of the re-coater's movements on the parts orientation. They claim that the larger shrinkage that occurred in parts

orientated along the machines Y-direction is mainly due to the friction forces that exist between the new powder layer and the sintered layer when recoating. They also attribute it to the possibility that there exists a variation in powder density in the Y-direction as the re-coater moves along the X-direction.

Ning *et al.* (2005) determined that the scanning vector direction has a significant effect on the bronze-based components' strength and consequently the material properties of the sintered parts. In test samples, where the scanning vector direction was parallel to the load direction (Figure 5), the average tensile strength was higher than the average strength of samples with a scanning vector direction perpendicular to the load direction (Figure 6). However, the minimum tensile strength was obtained in samples where the part orientation was parallel to the load direction such that the load would want to pull the layers apart (Figure 7). Furthermore it was discovered that the part orientation has a greater effect on the part strength than the scanning vector length.

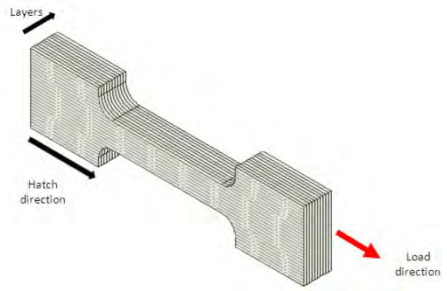

Figure 5: Illustration of a sample where the load is applied parallel to the hatch direction

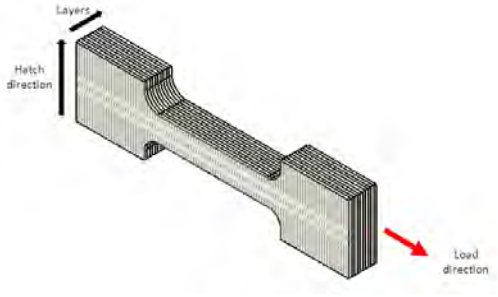

Figure 6: Illustration of a sample where the load is applied perpendicular to the hatch direction

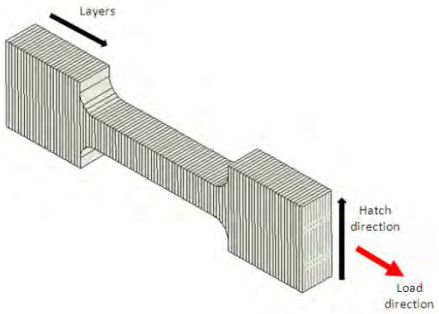

Figure 7: Illustration of a sample where the part is orientated parallel to load direction

In his experiments, Simchi (2006) discovered that when sintering iron powders in argon and nitrogen atmospheres respectively, better densification was obtained in the argon atmosphere. At low scan rates, the atmosphere had a larger influence on the densification while the atmosphere did not play a significant role at high scan rates. The low oxygen content being present in a nitrogen or argon environment reduced the surface oxides and slags that formed during the melting of the powder particles and consequently also reduced the surface tension.

Dai and Shaw (2004) determined that the degree of dimensional deformation in metal and ceramic powders is directly proportional to the temperature gradient. In order to minimize dimensional deformation the temperature gradient must be minimized (Wang *et al.,* 2007; Dai & Shaw, 2004; Dong *et al.,* 2009) and according to them this can be done by increasing the atmospheric temperature inside the building chamber (Dai & Shaw, 2004).

2.5 RELATED PROBLEMS AND EFFORTS TO REDUCE DIMENSIONAL DEFORMATION

In this section other researchers' attempts to increase the quality of the sintered parts and to reduce deformation in the sintered components will be discussed and their findings presented.

Zhu *et al*. (2003) made use of infiltration in an effort to improve the quality of their copper-based laser sintered parts. They chose epoxy as infiltrate in their experiments because of its high viscosity and good wetting capabilities in metal materials. In addition they added silver to the sintering powder in order to improve the ductility of sintered parts. Their results showed that infiltration can increase the densities of laser sintered parts, but does not affect the hardness. Additionally, the surface finish of the infiltrated parts improved when compared to the sintered parts. Even though the densities did improve through infiltration, the soft epoxy was unable to provide sufficient strength to prevent deformation. In similar experiments, Khaing *et al.* (2001) agreed that the surface roughness and density of copper-based laser sintered parts improved after epoxy infiltration. High deformation was, however, still experienced and the thermal conductivity was degraded after infiltration. They also revealed that the hardness of the sintered parts increased after epoxy infiltration and suggested that the hardness can be improved even further with low-melting point infiltration of silver or a lead-tin alloy.

In an attempt to minimize the effect of the dimensional offset caused by the laser's heat-affected zone on the boundary of the part, Simchi (2006) applied pre-contouring and post-contouring scanning techniques on ferrous metal powders. This was found to improve the dimensional accuracy of the final part.

Senhilkumaran *et al.* (2009) noted that the actual width of a single scan line was less than the spot diameter. A beam compensation adjustment value was defined that would calibrate the machine for specified parameters in order to obtain more accurate results on parts (Senhilkumaran *et al.,* 2009;

Zhu *et al.,* 2005). By calibrating the beam compensation value the dimensional accuracy of nylon samples improved up to 10 times (Senhilkumaran *et al.,* 2009).

Simchi *et al.* (2003) stated that the rapid cooling of iron-based DMLS components as well as phase transformations can lead to the accumulation of thermal stresses which result in dimensional deformation of the iron-based parts. They recommended that the DMLS part be post-sintered in order to close remaining pores, homogenize the microstructure and remove residual stresses. Completely dense parts and almost no shrinkage were obtained when parts were post-sintered while still being fixed to the base plate. In another study by Kibble *et al. (2007),* bronze (*DM20*) DMLS tensile test bars were heat treated in a muffle furnace at 650 ºC for 24 hours. When comparing the test bars after the heat treatment to those that were only stress relieved, it was found that the heat treated bars expanded with 3 - 4% over the length and cross section. This resulted in an increased porosity which resulted in a 50% reduction in strength.

2.6 MICROSTRUCTURES

When analysing the sintered samples of a copper-based metal powder, Gu *et al.* (2006) discovered that the samples consisted mainly of a dendritic structure in a network shape. They determined that the homogeneity, continuity and density of the dendritic structure depended on the process conditions or parameters. Their samples had a fully dense and continuous microstructure at 350 W and 0.04 m/s laser scan speed while at an increased laser speed of 0.06 m/s the microstructure became heterogeneous and discontinuous, showing narrow and thin dendrites. At 400 W laser power and 0.06 m/s laser speed, the densification improved, showing a continuous network with broad dendrites (Figure 8).

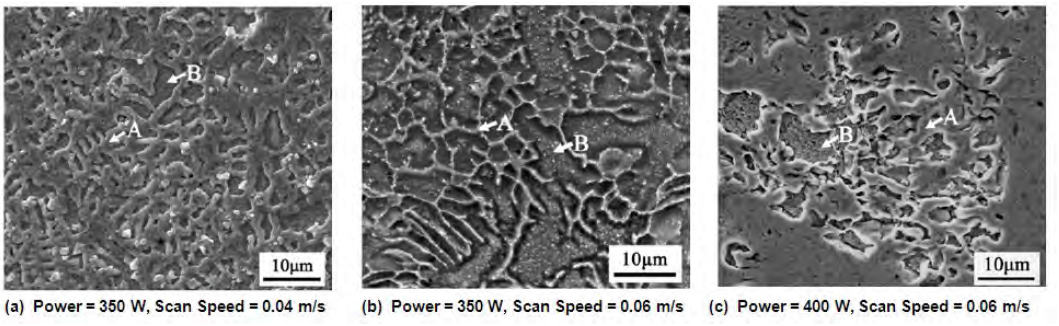

Figure 8: SEM images of the surface morphology of the microstructure of laser sintered Cu-based samples in which the laser power and laser scan speed were varied (Gu *et al*., 2006)

Additionally, their experiments demonstrated that the laser scan line spacing directly influences the number of pores in the microstructure and therefore the porosity of the sintered parts. Different to high laser scan line spacing, no individual tracks could be identified in the microstructure at lower laser scan line spacing (larger overlap), and an even and solid microstructure was obtained (Figure 9).

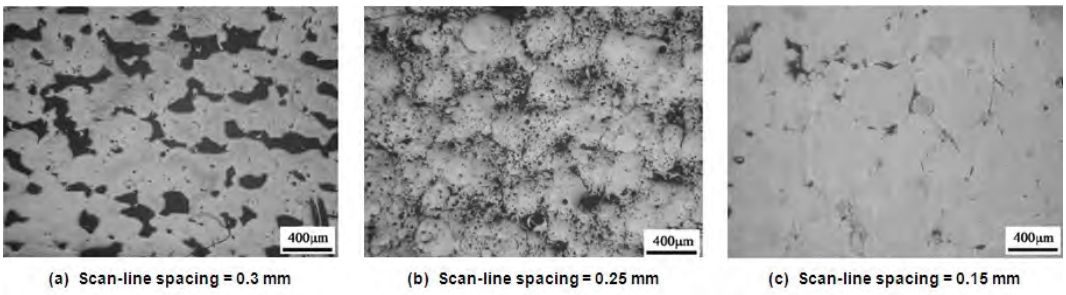

Figure 9: SEM images of the polished, non-etched microstructure on cross-sections of laser sintered Cu-based samples with variation in laser scan-line spacing. Process parameters are laser power 375 W, laser scan speed 0.05 m/s and powder layer thickness 0.3 mm (Gu *et al*., 2006)

The powder layer thickness also affected the microstructure. At a high powder layer thickness (0.4 mm) the sintered layers were not arranged horizontally, but at an angle instead. Here the layers in the microstructure were separated by thin, irregular, interconnected pores. As the powder layer thickness decreased the pores decreased and the layers became more structured and horizontally aligned until at 0.2 mm powder layer thickness the layers were horizontally aligned and the microstructure was consistent and homogeneous (Figure 10).

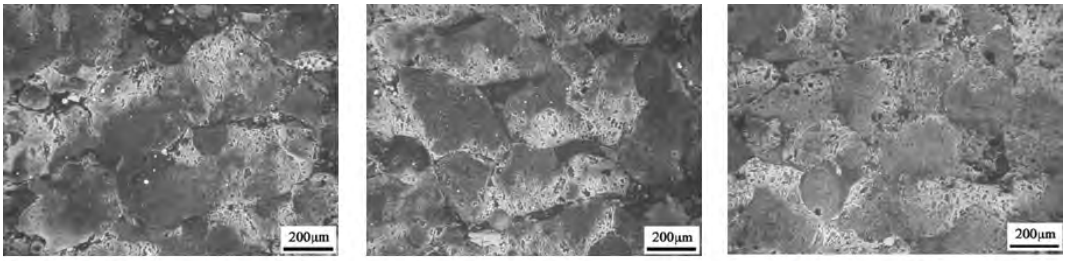

Figure 10: SEM images of the microstructure on cross-sections of laser sintered Cu-based samples at different powder layer thicknesses. Processing parameters are laser powder 375 W, laser scan speed 0.05 m/s and laser scan line spacing 0.15 mm (Gu *et al*., 2006)

In experiments on a copper-based powder mixture, Tang *et al.* (2003) studied the effect of the amount of the binder (SCuP) in the powder on the microstructure of the sintered parts. They observed that the porosity, pore size and shape, and the agglomeration size and shape are associated with the amount of binder particles (SCuP) in the powder system. As the amount of binder in the powder was increased from 25 vol% to 55 vol% the microstructure became denser as the spreading of the binder was improved, but high porosity was still obtained due to the short transient interaction duration of the laser beam and metal powder.

2.7 CONCLUSIONS AND PURPOSE OF STUDY

The DMLS process is an intricate process and the accuracy and quality of the final sintered parts are influenced by multiple variable process parameters. The degree of dimensional deformation, the strength and density are proportional to the temperature gradient in the sintered part which is a function of the energy input to the system. The energy is increased when the laser power is increased and the velocity, laser focus diameter, scanning vector length, hatch spacing and layer thickness is decreased. But as the quality of the part is defined by the density, strength and accuracy, this can become a tug-of-war situation where either the strength or the density will have to be compromised in order to obtain dimensional accuracy.

Although the open literature agrees on the effect of the sintering parameters on the quality of the sintered part, some difference exits between the findings of Simchi (2006), Ning *et al*. (2005) and Matsumoto *et al.* (2002) with respect to the effect of laser scanning vector length on the quality of the sintered

parts. Senthilkumaran *et al*. (2009) did work on the effect of contouring and hatching on the quality of the final sintered part. But other than that, no work has yet been done on the effect of different scanning strategies on the dimensional deformation and quality of the final sintered parts.

The purpose of this study is therefore aimed at the determination of the effect of different scanning strategies, with set parameters currently in standard use, on the dimensional deformation and quality of copper-based DMLS parts.

2.8 SCOPE

In this study the material powder used for sintering will be characterized and the effect that different geometric sintering strategies have on the quality of parts sintered with *Direct Metal 20* powder investigated. Three different scanning techniques currently in standard use on the EOSINT M250 Xtended machine at the CRPM is examined, namely *Solid Skin*, *Skin Stripes* and *Skin Chess*. The quality of the final parts is investigated and defined in terms of the dimensional deformation, the porosities and the microstructures obtained. No consideration is given to the sintering time, the tensile strength, surface finish or the hardness of final part samples.

CHAPTER 3: EXPERIMENTAL PROCEDURE

3.1 INTRODUCTION

Samples manufactured by DLS using a bronze-based metal powder, *DM20,* with a claimed composition of 70 – 90% copper, 10 – 30% nickel, 5 – 10% tin and 1 – 5% phosphorus were investigated. The experimental work consisted of a number of determinations to characterize the metal powder employed and to capture the extent of the degree of deformation of rectangular parts manufactured through DMLS. Two sets of three test samples were produced employing different sintering parameters. The deformation of each sample was determined before and after it was cut from the base-plate on which it was originally sintered. These specimens were then prepared for the various characterisation methods employed inclusive of porosity determinations and microscopic and electron microscopic studies and analyses.

3.2 MATERIAL POWDER CHARACTERIZATION

Semi-quantitative and qualitative X-ray fluorescence (XRF) analyses were carried out at Mintek's (National Minerals Technology-Research Organisation in Randburg, South Africa) analytical services division on duplicate bulk samples of *DM 20* powders to determine elemental compositions of the powder and to verify supplier claims and specifications.

For the purpose of determining the variation in the composition of the individual grains, a sample of *DM 20* powder was mounted in an Akasel-Aka-resin. The resin-mounted sample was then conventionally ground and polished with a 1 μm diamond paste to provide a flat surface for analysis through Energy Dispersive X-ray Spectrometry (EDS) using a silicon drifted detector on an Oxford Instruments Quanta FEG 250 Scanning Electron Microscope (SEM). EDS analyses were carried out on 24 grains in the mounted sample to identify and determine the composition of the different phases in the material powder. Multichannel analyser energy level counts were converted to percentage of elements present as a percentage oxide based on prior standard calibration. The EDS calibration software corrected for atomic number (Z), absorption (A) and fluorescence (F) effects, known as

ZAF corrections. The analyses of the metal grains were performed at 15 kV and using a suitable beam current to produce backscatter electron (BSE) imaging and practical EDS acquisition parameters.

To facilitate in the determination of the different morphologies present in the powder and to relate the morphologies to the compositions, loose grains of *DM 20* powder was deposited onto carbon paste to prevent charge build-up during beam exposure under the SEM and this sample was examined in a similar manner as above in order to relate observable 3D morphologies to qualitative compositions.

The SEM images of the metal powder were furthermore evaluated with Nikon Imaging Software (NIS-Elements D 3.2) in order to obtain the particle size distribution of a material powder sample. This was established by constructing a mesh on a microscope image of the material powder sample. The longest diameter, known as the Feret's diameter, of particles that lay on the intersecting points of the horizontal and vertical lines was measured. These data were additionally evaluated to classify the particles in terms of their morphology, e.g. spherical, lenticular or agglomerated.

Results

The composition of the powder determined through quantitative XRF analysis are compared to the compositional range provided by the material supplier and is listed in Table 1.

Element weight percentages (wt%)		
Element	XRF	Supplier *DM 20* (EOS, 2004)
Copper	77	70 - 90
Nickel	16.5	10 - 30
Tin	5	5 - 10
Phosphorus	0.5	1 - 5

Table 1: Powder composition of *DM 20* obtained from XRF analysis compared to supplier compositional claim

From the data obtained in Table 1 it is evident that the powder consists of 77% Cu, 17% Ni, 5% Sn and 0.5% P.

The compositions (normalized to 100%) of a number of grains of the embedded polished powder sample shown in Figure 11, obtained through SEM EDS analyses, are presented in Table 2. These analyses have been arranged, using the presence or absence of Sn, P and Ni, into groups (identified by colouring) thought to represent compositional variation in similar phases.

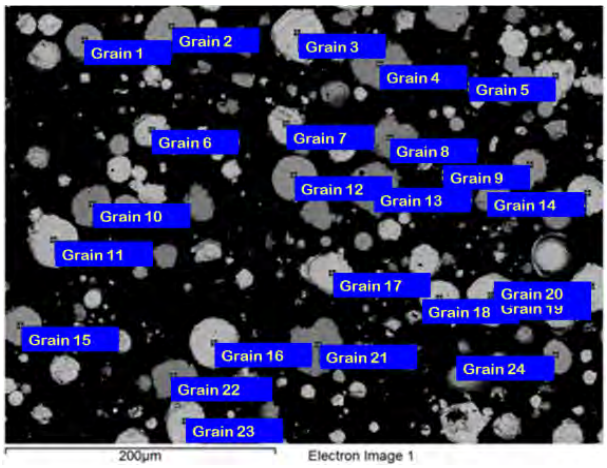

Figure 11: Secondary electron image of *DM 20* grains embedded in resin showing marked SEM EDS analysed grains

	Grain	P	Ni	Cu	Sn
		%	%	%	%
Phase 1	**Grain1**	2.2	0.0	97.8	0.0
	Grain2	1.8	0.5	97.7	0.0
	Grain 9	3.4	0.5	96.2	0.0
	Grain 12	8.3	0.3	91.3	0.0
	Grain 15	6.8	0.0	92.8	0.4
	Grain 24	3.1	0.0	96.9	0.0
Phase 2	**Grain3**	0.7	0.0	90.5	8.8
	Grain 5	0.0	0.0	94.9	5.1
	Grain 6	0.2	0.4	88.7	10.7
	Grain7	0.8	1.1	88.8	9.4
	Grain 11	0.5	0.4	87.4	11.6
	Grain 14	0.8	0.7	83.7	14.8
	Grain 16	0.2	0.5	88.4	10.8
	Grain17	0.3	0.0	91.1	8.7
	Grain 18	0.2	0.3	88.4	11.1
	Grain 19	0.6	0.0	88.8	10.6
	Grain 20	0.5	0.5	88.3	10.6
	Grain 23	0.5	0.5	87.8	11.2
Phase 3	**Grain 4**	0.0	100.0	0.0	0.0
	Grain 8	0.0	95.9	4.1	0.0
	Grain 10	0.0	95.3	4.7	0.0
	Grain 13	0.0	96.9	3.1	0.0
	Grain 21	0.0	96.9	3.1	0.0
	Grain 22	0.0	98.0	2.0	0.0

Table 2: The composition of a number of grains, embedded in resin and marked in Figure 11, obtained through SEM EDS analysis.

The analyses of compositional variations presented in Table 2 tend to show that essentially 3 phases are present in the powder as summarised in Table 3.

	Copper (Cu) wt %	**Phosphorus (P) wt %**	**Nickel (Ni) wt %**	**Tin (Sn) wt %**
Phase 1 **(Highlighted in yellow)**	91.3 - 97.8	1.8 - 8.3	0 – 0.5	
Phase 2 **(Highlighted in blue)**	83.7 - 94.9	0 - 0.8	0 - 1.1	5.1 - 14.8
Phase 3 **(Highlighted in green)**	0 - 4.7		95.2 - 100	

Table 3: Summary of phases identified in *DM 20* material particles

Evaluation of the particle compositions presented in Table 3 tend to indicate that the composition of *DM 20* particles varies between copper-phosphorus (Cu8.3P and Cu2P) with up to 0.5 wt% nickel present in the solid solution (Phase 1 in Table 3). The next phase is α-phase copper (Cu15Sn and Cu5Sn) in which up to 1 wt% nickel can exist in the solid solution (Phase 2 in Table 3). In addition, it is deduced that this phase can also contain up to 1 wt% phosphorus and that the composition can vary from grain to grain

within these limits. The third phase is nickel with traces of copper (up to 5 wt%) present in the solid solution (Phase 3 in Table 3).

The backscatter SEM images (at 1 000 times and 2 000 times magnifications respectively) of the powder deposited on the carbon paste tape is shown in Figure 12 and Figure 13.

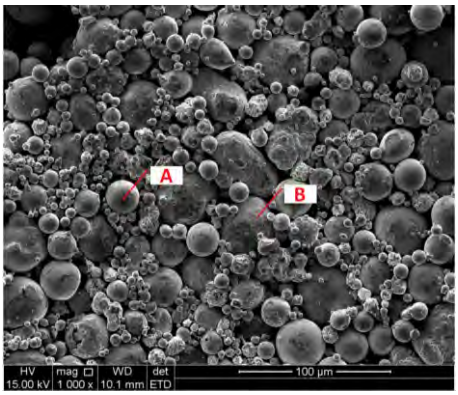

Figure 12: Backscatter SEM image at 1 000 times magnification of *DM 20* powder deposited onto carbon paste tape

Analyses of the morphologies shown (Figure 12) tend to indicate that the virgin powder consists mainly of spherical and near perfect spherical grains (marked A and B in Figure 12) of variable size. The particle dimensions were measured according to the Feret's diameter method (presented in APPENDIX B) and it was determined that the magnitudes of the spherical grains vary from 2 – 30 µm and that of the near spherical grains from 10 - 45 µm.

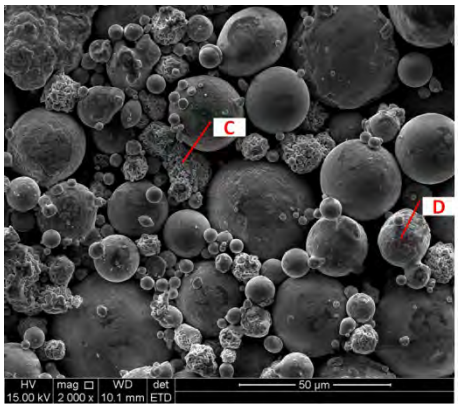

Figure 13: Backscatter SEM image at 2 000 times magnification of *DM 20* powder deposited onto carbon paste tape

Detailed observation at 2 000 times magnification showed that apart from the two main morphologies reported, a significant number of agglomerates of grains (marked C in Figure 13) with sizes that vary from 5 – 45 µm and some lenticular grains (marked D in Figure 13) with sizes that vary from 4 – 50 µm are also present.

Enlarged SEM images of typical morphologies marked in Figure 12 and Figure 13 are presented in Figure 14. A qualitative EDS SEM analysis was done on each of the grains presented in the figure and the shape, size and qualitative composition of the specific grains are listed next to the image.

	Morphology	Shape and texture	Size in µm	Composition in weight %
A	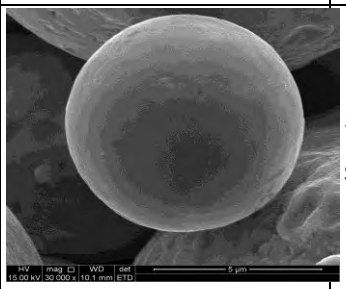	Spheres with a smooth surface	5	Cu7P
B	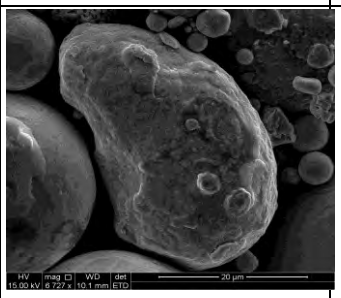	Near-spherical particles with orange-peel like surface	40	Cu11Sn
C	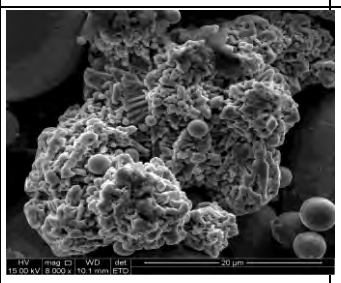	Agglomerate with an undulating surface appearance	45	Ni
D		Lenticular shaped figures with small crystals inside and undulating edges	40	Cu8P

Figure 14: SEM images of typical morphologies in a sample of *DM20* powder with the shape, size and quantitative SEM EDS results listed next to the image of the grain investigated

From the data presented in Figure 14 it is deduced that a typical spherical grain, 5 µm in size, has the composition of Cu7P, while the near spherical grain presented has a size of 40 µm and consist of Cu11Sn. A representative agglomerate, 45 µm in size, consist of pure Ni while a lenticular grain, 40 µm in size, has a composition of Cu8P.

The optical analysis of Figure 12 (APPENDIX B) revealed that the particle sizes vary from 2 µm to 45 µm with a mean particle size of 20 mm and a standard deviation of the powder dimensions of 11.5 mm. The percentage fractions of the particle sizes are presented in the form of a histogram in Figure 15.

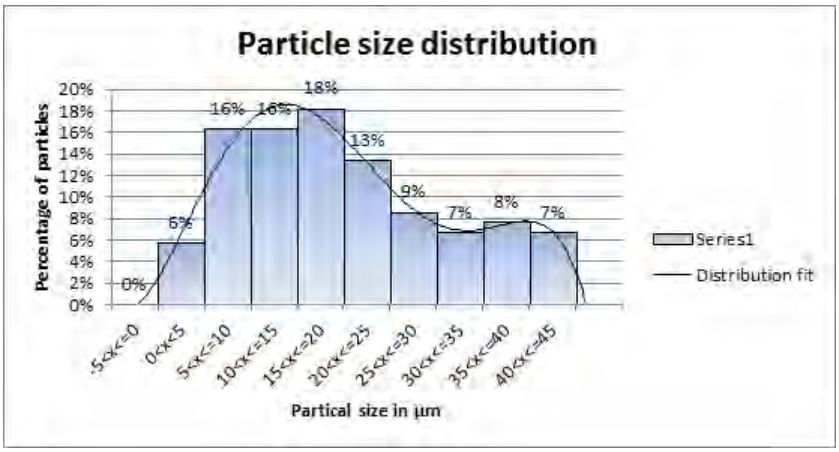

Figure 15: Particle size distribution of powder sample including measurement data of all morphologies present

From the data presented in Table 13 (APPENDIX B) it is determined that 20% of the powder particles are agglomerates (previously determined to be nickel). In Figure 16 below, the agglomerates are excluded from the particle size analysis and the data reworked to 100% in order to obtain the particle size distribution of the remainder of the particles (spherical, near-spherical and occasional lenticular grains).

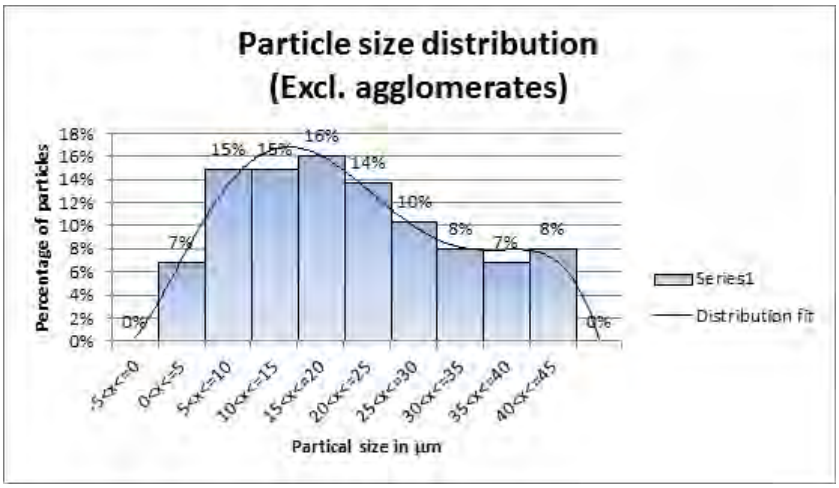

Figure 16: Particle size distribution of powder sample excluding measurement data of agglomerates

3.3 SAMPLE PRODUCTION

Three pairs of rectangular samples of dimensions 50 x 25 x 6 mm (Figure 17) were sintered from *DM 20* powder using an EOSINT M250 Xtended laser sintering machine.

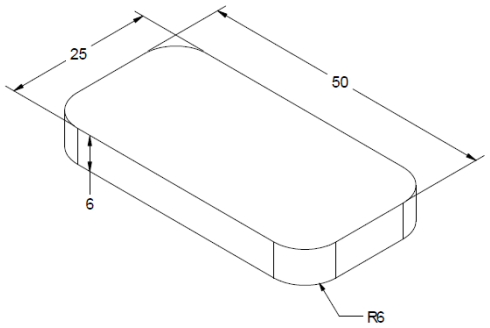

Figure 17: CAD drawing which indicates the outline and dimensions of the *DM 20* DMLS samples

All samples were orientated on the machine's xy-plane at 25º with respect to the x -axis about the z-axis to ensure that the re-coater blade could run over the sintered layers smoothly. By orientating the samples at this angle, no edge was orientated parallel to the re-coater blade and subsequently the chances of the re-coater blade getting stuck on a layer or row (or stop on an edge) was minimised (see Figure 21 below for sample orientation on platform). A 2 mm extrusion was first sintered onto the base plate which served as a solid support onto which each sample was sintered. On completion of sample growth the samples were cut from the base plate by way of a wire cutter and the base was removed without sacrificing any of the parts' geometry. The building-platform was pre-heated to 80 ºC prior to sintering. The sintering chamber was filled with nitrogen and the oxygen level in the chamber was kept at 0.2% during the course of the sintering process to limit oxidation.

All of the samples were manufactured with a CO_2 laser with a nominal laser power of 228 W and a wavelength of 10.6 µm - the diameter of the focused laser beam was 0.45 mm and the layer thickness on each deposit run was 0.06 mm.

Different geometric sintering strategies were employed for each of the three pairs known as 1) *Solid Skin*, 2) *Skin Stripes* and 3) *Skin Chess*, as reviewed in APPENDIX A. However all samples were sintered with the contouring and hatching strategy (discussed in Section 2.2) of which the pre- and post-contours of all samples had the same parameters. The pre-contours were sintered using a single laser track with a laser speed of 300 mm/s and a beam offset of 0.34 mm while the post-contours were sintered using a laser speed of 500 mm/s and a beam offset of 0.24 mm. The sintering parameters of each scanning technique are listed in APPENDIX C but are summarized next to the geometric sintering paths illustrated in Figure 18 to Figure 20 below for ease of comprehension. The outer skin of the samples manufactured through the *Skin Stripes* and *Skin Chess* sintering strategies had the same manufacturing parameters as the core of the sample manufactured through the *Solid Skin* sintering strategy.

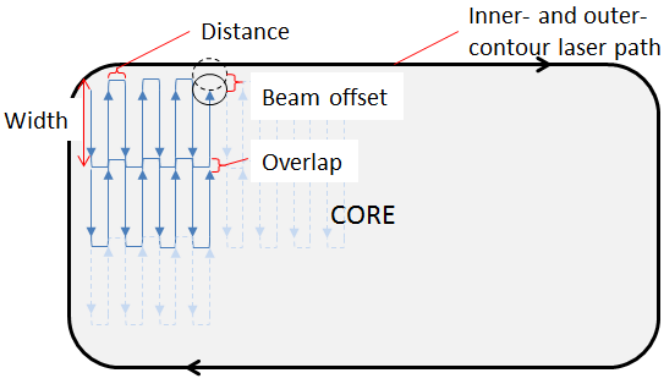

CORE PARAMETERS	
Width	5 mm
Distance	0.2 mm
Beam Offset	0.365 mm
Overlap	0.1 mm
Laser speed	500 mm/s

Figure 18: Sintering geometric surface paths for the samples manufactured with the *Solid Skin* sintering strategy with laser path indicated for the core (relative positions are indicated)

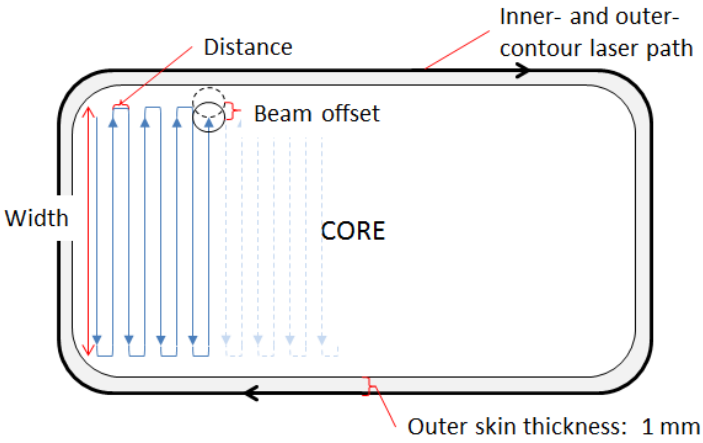

CORE PARAMETERS	
Width	60 mm
Distance	0.3 mm
Beam Offset	0.3 mm
Laser speed	250 mm/s

Figure 19: Sintering geometric surface paths for the samples manufactured with the *Skin Stripes* sintering strategy with laser path indicated for the core of the sample (relative positions are indicated)

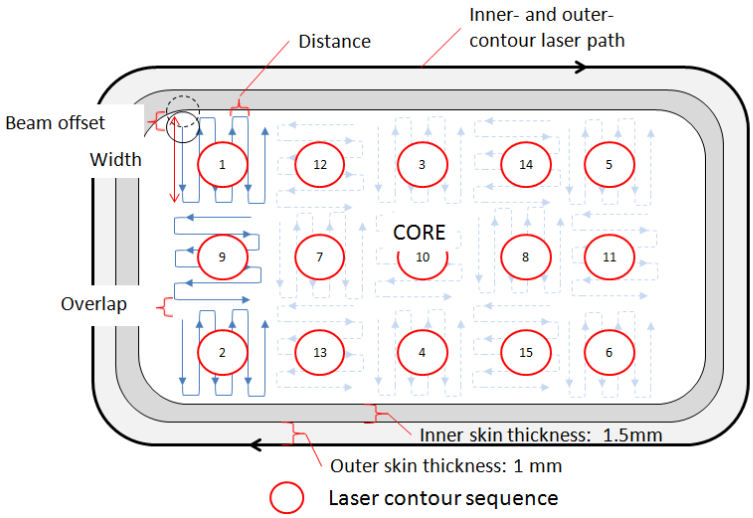

CORE PARAMETERS	
Width	7 mm
Distance	0.2 mm
Beam Offset	0.025 mm
Laser speed	875 mm/s
Overlap	0.04 gap

INNER SKIN PARAMETERS	
Width	5 mm
Distance	0.25 mm
Beam Offset	0.025 mm
Laser speed	350 mm/s
Overlap	0.04 gap

Figure 20: Sintering geometric surface paths for the sample manufactured with the *Skin Chess* sintering strategy with laser path indicated for the core of the sample (relative positions are indicated)

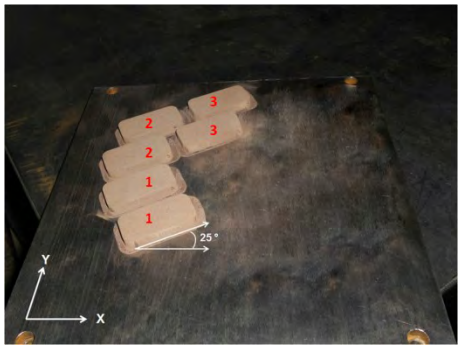

Figure 21: Produced samples as sintered onto the base plate orientated at 25º to the x-axis on the machine's xy-plane about the Z-axis

3.4 SAMPLE EVALUATION AND ANALYSES

This section describes the procedure followed to evaluate the sintered sample artefacts by means of optical light microscopic observations and elemental analyses employing SEM EDS of observed phases present.

3.4.1 Sample preparation

One of each pair of samples produced to the *Solid Skin*, *Skin Stripes* and *Skin Chess* geometric sintering patterns were sectioned, mounted, polished and etched in preparation of metallographic observations and analyses.

Each sample was sectioned with Struers' Secotom-10 using a silicon-carbide cut-off wheel. Sectioning was done along the samples' length and width such that four equal quarters were obtained for each sample (Figure 23). The wheel speed was 1 500 rpm while the feed rate was 0.75 mm/s. Cutting took place in a mixture of water and coolant to prevent over heating of the sample and wheel.

One quarter of the cut samples were hot mounted into 30 mm-diameter cylinders such that the longitudinal cross-sectional area was exposed (Figure 24). The samples were heated in a Struers Labo Press 3 for 6 minutes at 180 ºC while under a 30 kN force and then cooled for 8 minutes before released.

Figure 22: Struers' Secotom-10 used to section the samples

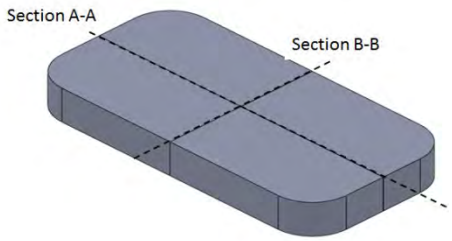

Figure 23: CAD model of sample with sectioning lines indicating where sectioning was done

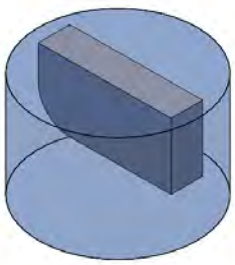

Figure 24: CAD model indicating the orientation of a section of a sample as mounted in resin

Grinding of the mounted samples were carried out with a Struers' Rotopol-11 machine using grinding discs with silicon carbide paper ranging from rough to fine grid sizes followed by polishing using cloth and diamond suspensions.

Details of the grinding and polishing procedures followed are summarized in APPENDIX D.

Figure 25: Struers Rotopol-11 machine used for grinding and polishing of samples

Etching of the samples was done by swabbing the samples delicately with cotton wool dunked in a mixture of water, iron-chloride and hydrochloric acid for 10 seconds to show the general structure[1].

3.4.2 Microstructural Inspection

To ascertain sintering effectiveness, the character of voids and their presence were determined, the variation in grain size and phase outlines observed and trends in the microstructure of the etched samples studied under reflected light at 50x, 200x and 500x magnifications using an Olympus UC 30 microscope. Observations were made at 9 positions i.e. at *top*, *middle* and *bottom* areas on the *outside*, *intermediate* and *centre* positions of each sample, where *bottom* denotes the first layers sintered onto the base plate and *top* denotes the last sintered layers while *outside* denotes the edge of the sample and *centre* denotes the middle of the sample (see Figure 26 for marked areas). The reflective light images at 50x and 200x magnifications only are presented in this section for the samples manufactured through the

[1] The mixture used for etching was prepared using the following quantities:

5 g Iron chloride ($FeCl_3$), 50 ml Hydrochloric acid (HCl), 100 ml Water

Solid Skin, *Skin Stripes* and *Skin Chess* sintering strategies. The complete range of images obtained is presented in APPENDIX E.

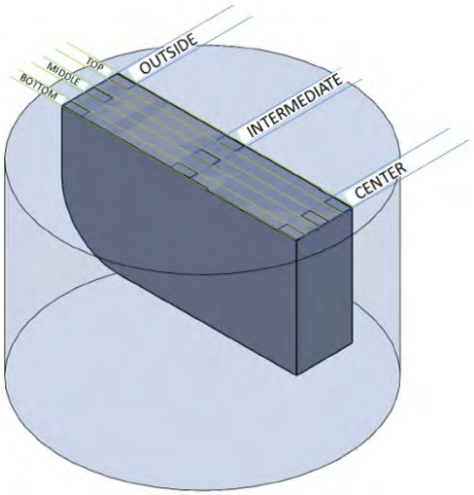

Figure 26: CAD model indicating positions on the mounted samples where reflective light microscope images were captured.

Photomicrographs of reflected light images of etched surfaces of the samples manufactured through the *Solid Skin*, *Skin Stripes* and *Skin Chess* geometric sintering strategies at 50x magnification at the nine positions indicated in Figure 26, are presented in Figure 27 to Figure 32.

	OUTSIDE	INTERMEDIATE	CENTER
TOP			
MIDDLE			
BOTTOM			

Figure 27: Optical microscope images of the samples manufactured through the *Solid Skin* geometric sintering strategy at 50x magnification at the nine positions indicated in Figure 26. More white glass phases and fewer voids are observed in the intermediate position.

Figure 28: Optical microscope images of the samples manufactured through the *Skin Stripes* geometric sintering strategy at 50x magnification at the nine positions indicated in Figure 26. The skin is separated from the core with a crack at the *outside* of the sample.

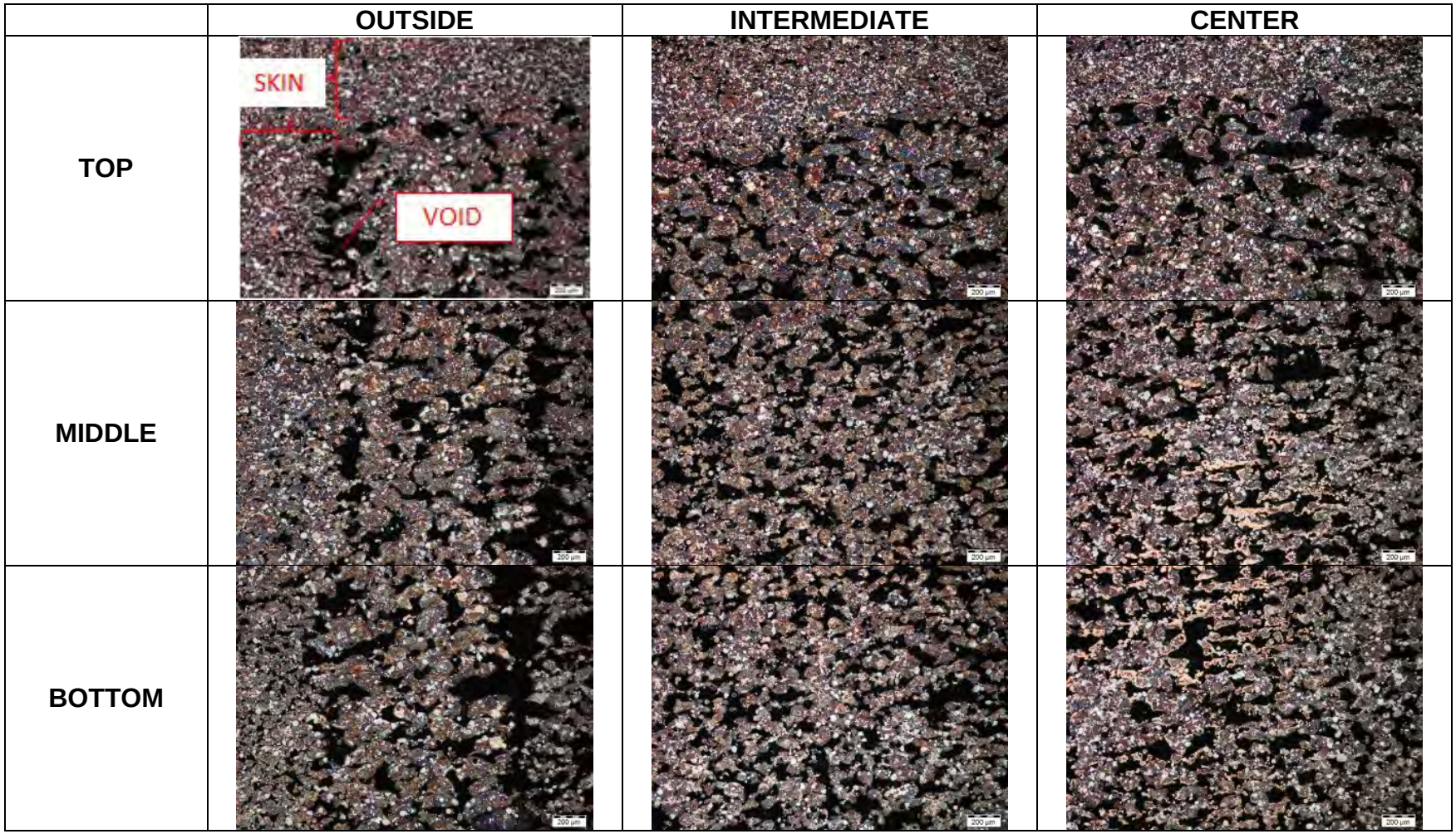

Figure 29: Optical microscope images of the samples manufactured through the *Skin Chess* geometric sintering strategy at 50x magnifications at the nine positions indicated in Figure 26**.** A denser skin area is detected at the *outside* and *top* positions of the sample while high porosity is observed in general across the sample.

From the photomicrographs presented in Figure 27 it is observed that more glass phases (white matrix) and fewer voids are present in the *intermediate* positions of the sample manufactured through the *Solid Skin* geometric sintering strategy than at the *outside* and *centre* positions.
On the *outside* of the samples manufactured through the *Skin Stripes* and *Skin Chess* geometric sintering strategies (Figure 28 and Figure 29) it is evident that a crack separates the *skin* from the *core*. The microstructure of the *skin* in the sample manufactured through the *Skin Chess* geometric sintering strategy is much denser than the *core* and in general it is unmistakable that the sample employing the *Skin Chess* geometric sintering strategy is much more porous than the other two samples.

Closer observations of the microstructures at 500x magnifications at the nine positions for each sample are presented in Figure 30 to Figure 32.

	OUTSIDE	INTERMEDIATE	CENTER
TOP	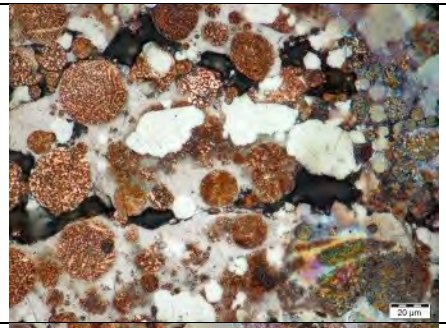	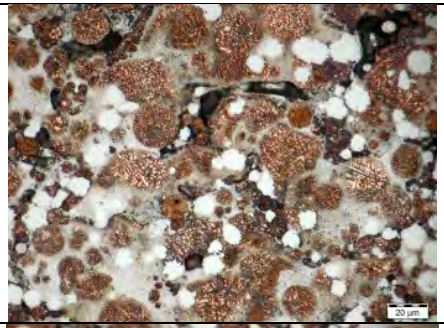	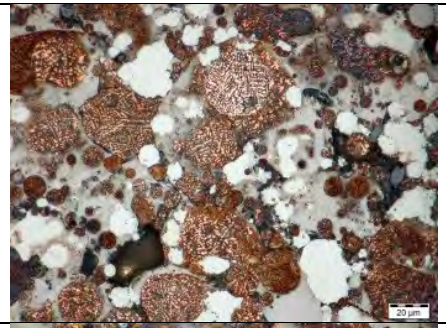
MIDDLE	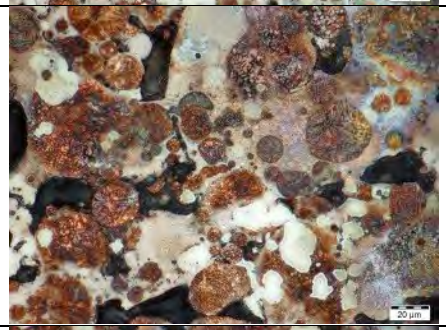	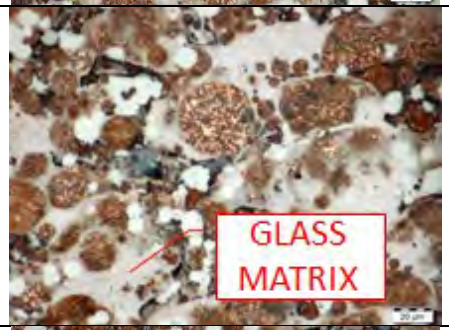	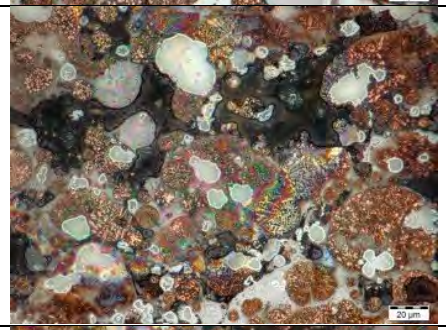
BOTTOM	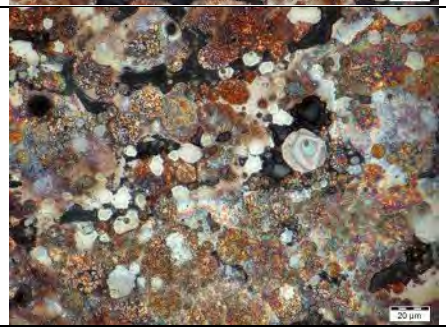	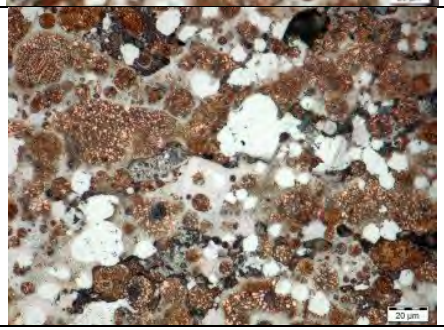	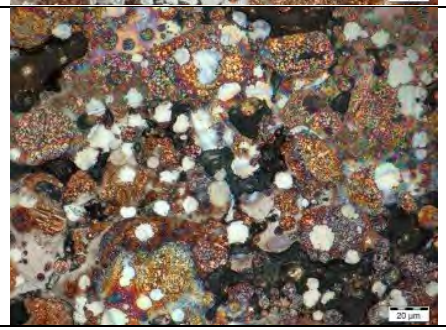

Figure 30: Optical microscope images of the sample manufactured through the *Solid Skin* geometric sintering strategy at 500x magnification at the nine positions indicated in Figure 26. More white glass matrix surrounding the other grains are observed in the *intermediate* and *top* areas than in the other positions.

	OUTSIDE	INTERMEDIATE	CENTER
TOP	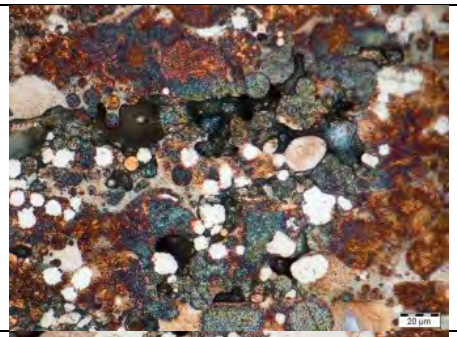		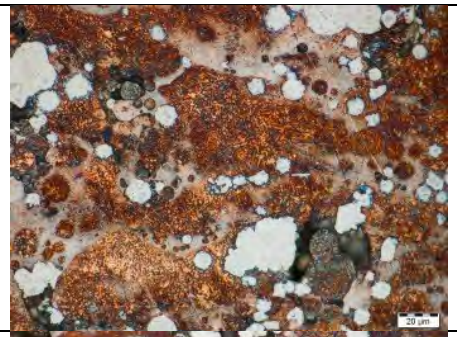
MIDDLE	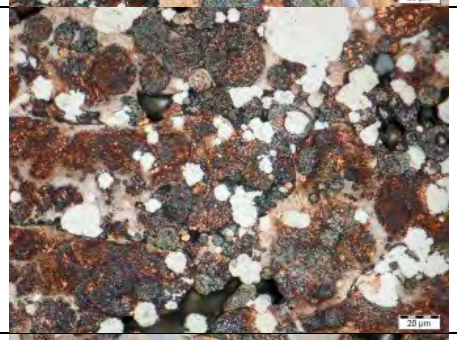	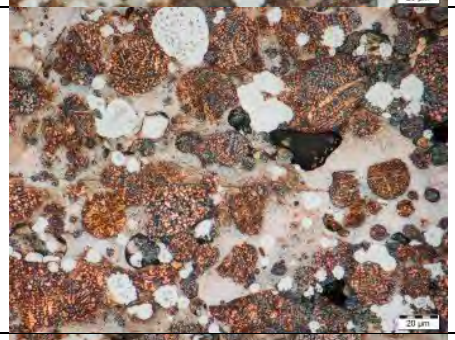	
BOTTOM		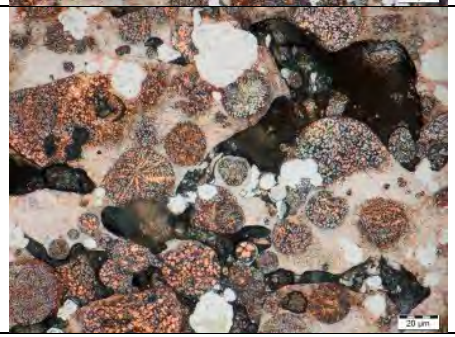	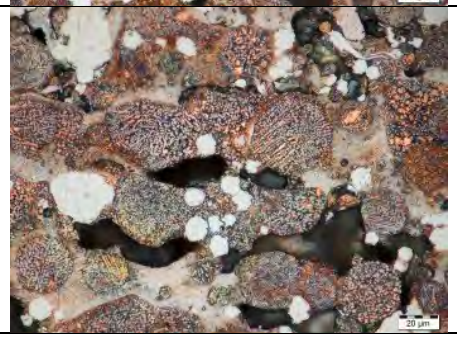

Figure 31: Optical microscope images of the sample manufactured through the *Skin Stripes* geometric sintering strategy at 500x magnification in the nine positions indicated in Figure 26 showing porosity (dark areas) in the sample.

	OUTSIDE	INTERMEDIATE	CENTER
TOP	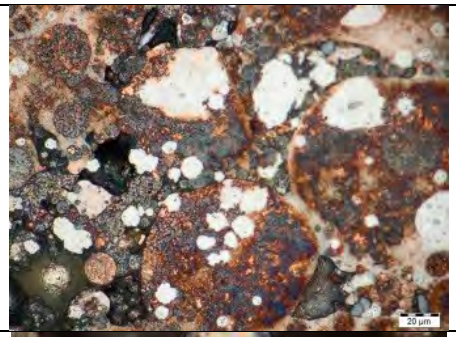	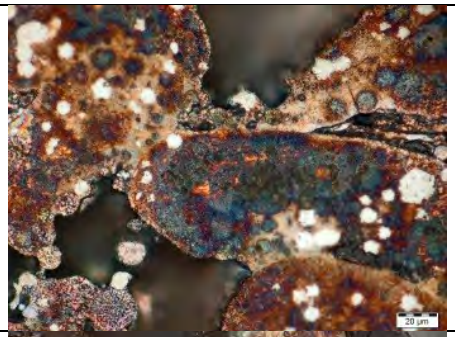	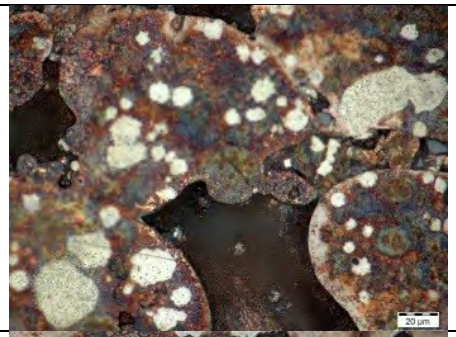
MIDDLE		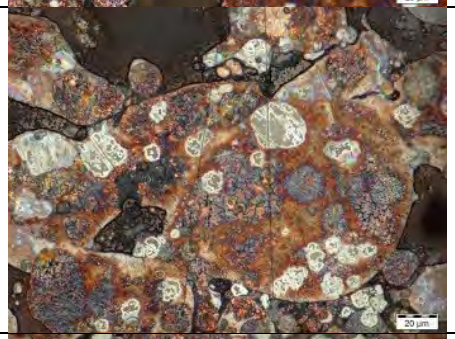	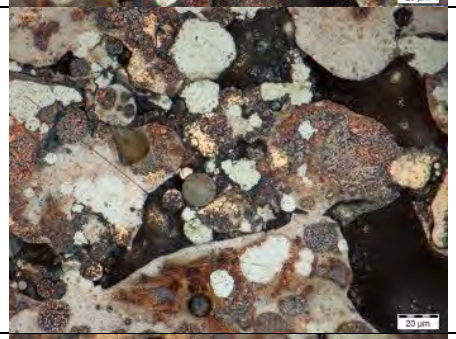
BOTTOM	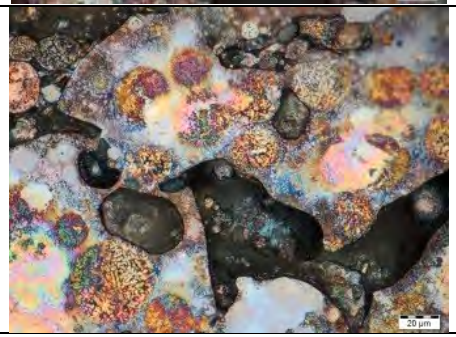	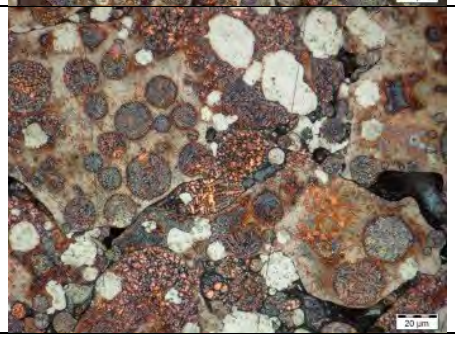	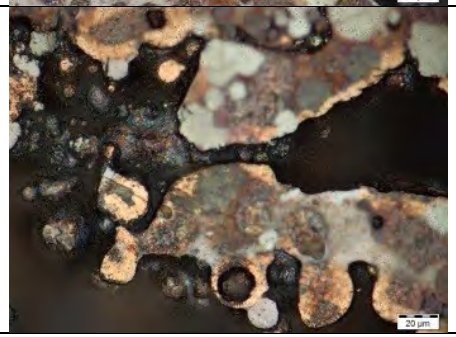

Figure 32: Optical microscope images of the sample manufactured through the *Skin Chess* geometric sintering strategy at 500x magnification in the nine positions indicated in Figure 26 showing high porosity across the sample.

From the photomicrographs presented in Figure 27 it is observed that more glass phases (white matrix) and fewer voids are present in the *intermediate* positions of the sample manufactured through the *Solid Skin* geometric sintering strategy than at the o*utside* and *centre* positions.

From the images presented in Figure 30 to Figure 32 it can be observed that many voids are present in the sintered microstructures of all three samples with considerably more and larger voids present in the sample manufactured through the *Skin Chess* geometric sintering strategy. The microstructures are irregular with spherical bronze-coloured phases and irregular white phases (later confirmed to be nickel) of different sizes cemented in a white-grey matrix. At closer observation of the sample manufactured through the *Solid Skin* geometric sintering strategy (Figure 30) it is observed that more glass phases (white matrix) and fewer voids are also present in the *top* positions of the sample.

3.4.3 Phase Identification

In addition to positions marked for the reflective light microscopic observations discussed in the previous section, three circular areas of 1 mm diameter each were marked in the core of the samples along the length, 7.5 mm from each other at the *outside* (position A), *intermediate* (position B) and *centre* (position C) positions of the mounted and etched samples (Figure 33).

Reflective light microscope images were captured in the marked areas (with a NikonDs-F1i camera attached to a Nikon Optiphot-100 microscope) to identify phases (that appeared different in colour after etching) that can indicate different compositions. The microstructures of the microscopic images were then compared with secondary electron images of the same areas for analytical purposes to ensure analysis of comparative phases. A Thermo Scientific EDS detector was then employed to determine the composition of the phases identified in the sintered microstructure and to attain the composition of the phases that participated in the sintering.

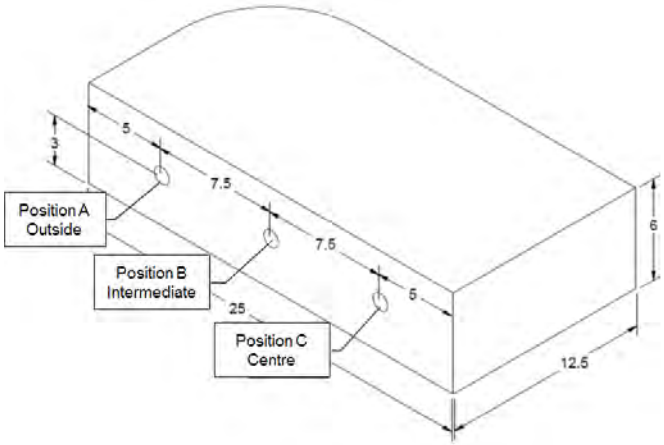

Figure 33: CAD representation of sample section with position of marked areas for metallographic observations indicated

Results

In the paragraphs that follow reflective light microscope images are presented next to the comparative SEM images with the typical results from the EDS SEM analyses of the phases marked in the samples manufactured through the *Solid Skin*, *Skin Stripes* and *Skin Chess* geometric sintering strategies. Not all phases were marked and analysed in each of the three positions, but it was attempted that all phases in each sample be identified and analysed. Detailed analyses results are presented in APPENDIX F.

Samples manufactured through the *Solid Skin* geometric sintering strategy

Position A *(Outside)*

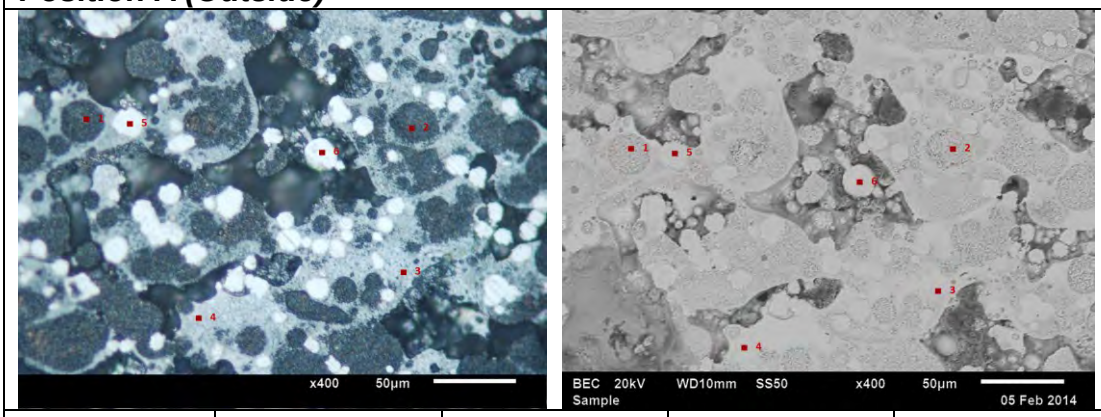

	wt% **Cu**	wt% **P**	wt% **Ni**	wt% **Sn**
1	88.9	0.8	0.8	9.5
2	86.3	1.0	0.8	11.9
3	93.7	4.7	0.7	1.0
4	94.0	3.4	2.2	0.4
5	4.1	0.1	95.8	0.0
6	3.5	0.0	96.4	0.2

Figure 34: Reflected light microscope and comparable SEM images of identical areas with composition of phases identified in position A (Figure 33) of the sample manufactured through the *Solid Skin* geometric sintering strategy as marked with corresponding numbers in the figures.

Position B *(Intermediate)*

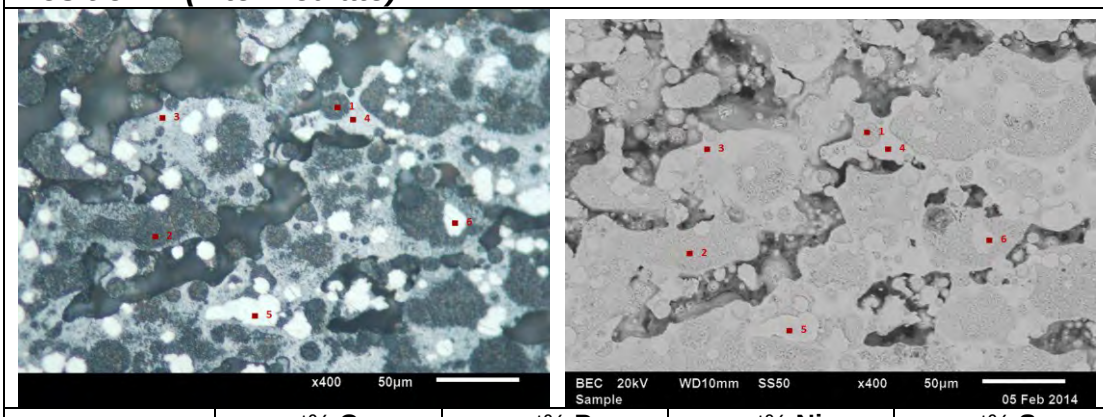

	wt% **Cu**	wt% **P**	wt% **Ni**	wt% **Sn**
1	88.3	1.0	0.5	10.2
2	88.0	1.0	0.5	10.5
3	93.2	5.2	1.2	0.4
4	94.5	4.6	0.8	0.1
5	2.9	0.1	97.1	0.0
6	4.2	0.0	95.6	0.2

Figure 35: Reflected light microscope and comparable SEM images of identical areas with composition of phases identified in position B (Figure 33) of the sample manufactured through the *Solid Skin* geometric sintering strategy as marked with corresponding numbers in the figures.

Position C *(Centre)*

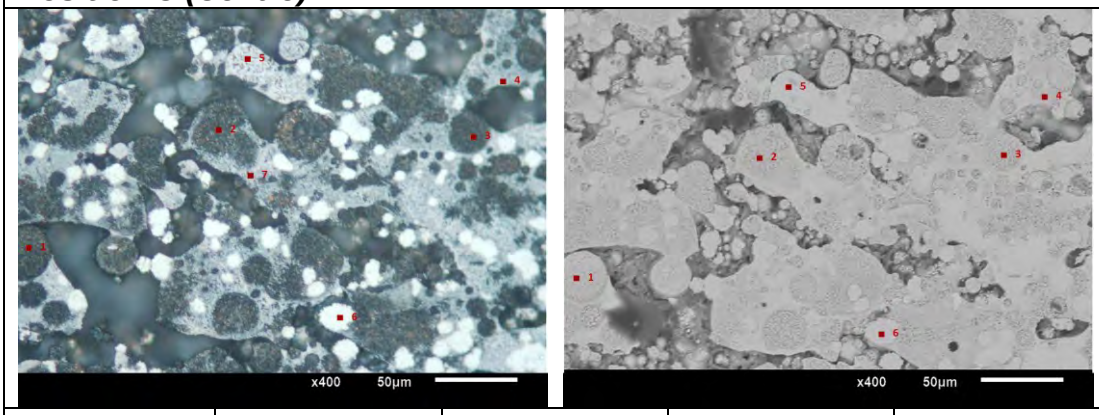

	wt% **Cu**	wt% **P**	wt% **Ni**	wt% **Sn**
1	90.6	0.6	0.2	8.6
2	90.3	1.3	0.5	7.9
3	89.5	0.9	0.5	9.1
4	92.6	5.1	0.6	1.7
5	93.7	5.4	0.5	0.4
6	2.4	0.0	97.5	0.2

Figure 36: Reflected light microscope and comparable SEM images of identical areas with composition of phases identified in position C (Figure 33) of the sample manufactured through the *Solid Skin* geometric sintering strategy as marked with corresponding numbers in the figures

The results for the phases present in the sample manufactured through the *Solid Skin* geometric sintering strategy is summarized in Table 4 below.

	Copper (Cu)	**Phosphorus (P)**	**Nickel (Ni)**	**Tin (Sn)**	**Description**
Phase 1	86.3 – 90.6%	0.6 – 1.3%	0.2 – 1.6%	7.9 – 11.9%	Dark, round with dendrites
Phase 2	2.4 – 5%	0 – 0.1%	94.8 – 97.5%	0 – 0.2%	White blotch
Phase 3	90 - 96.2%	2.1 - 6%	0.1 – 2.2%	0.1 – 4.4%	White-blue Matrix

Table 4: Summary of phases identified in the sample manufactured through the *Solid Skin* geometric sintering strategy

From the analysis it is evident that mainly three phases are present in the sintered microstructure of the sample manufactured through the *Solid Skin* geometric sintering strategy; the first phase (marked 1 and 2 in Figure 34 and Figure 35 and 1, 2 and 3 in Figure 36) is grains consisting of copper-tin (Cu8Sn – Cu12Sn) with traces of phosphorus and nickel (up to 1.5%), the next phase (marked 5 and 6 in Figure 34 and Figure 35 and 6 in Figure 36) is nickel with up to 5% copper, the third phase (marked 3 and 4 in Figure 34 and Figure 35 and 4 and 5 in Figure 36) cements the other two phases and

consists of copper-phosphorus (Cu2P-Cu6P) with up to 4% tin and traces of nickel (up to 2%).

Samples manufactured through the *Skin Stripes* geometric sintering strategy

Position A *(Outside)*

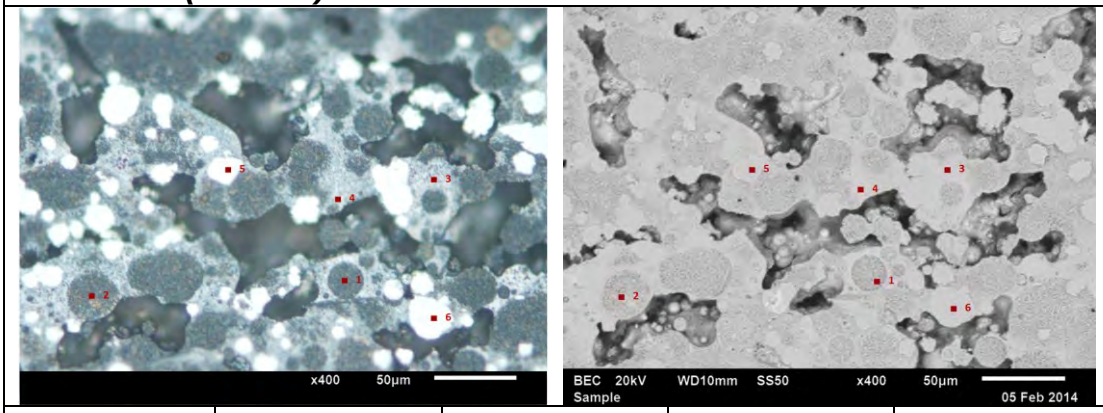

	wt% **Cu**	wt% **P**	wt% **Ni**	wt% **Sn**
1	88.5	0.6	0.7	10.2
2	91.6	0.8	0.6	7.1
3	96.3	2.4	0.5	0.7
4	94.7	3.7	0.7	0.9
5	3.2	0.1	96.6	0.1
6	2.0	0.1	97.9	0.1

Figure 37: Reflected light microscope and comparable SEM images of identical areas with composition of phases identified in position A (Figure 33) of the sample manufactured through the *Skin Stripes* sintering strategy as marked with corresponding numbers in the figures.

Position B (*Intermediate*)

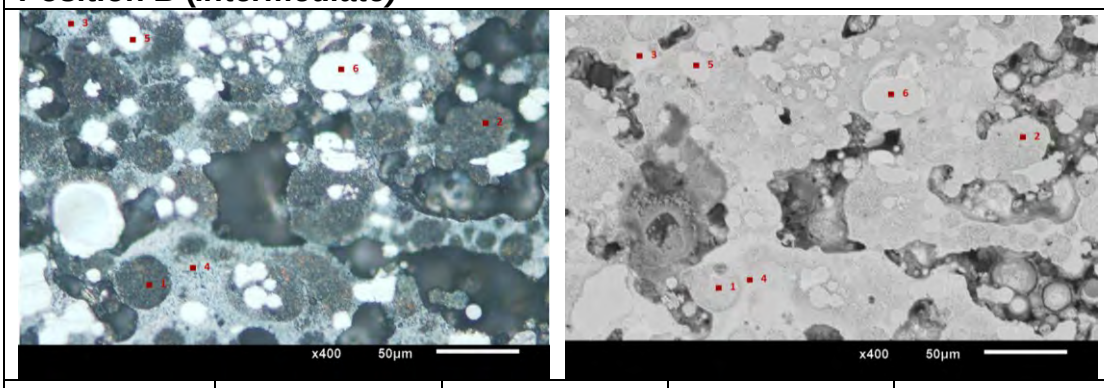

	wt% **Cu**	wt% **P**	wt% **Ni**	wt% **Sn**
1	87.2	0.8	1.7	10.4
2	89.5	0.4	0.8	9.3
3	93.7	5.5	0.5	0.3
4	92.3	5.1	0.7	1.8
5	2.6	0.1	97.3	0.1
6	0.9	0.0	99.1	0.0

Figure 38: Reflected light microscope and comparable SEM images of identical areas with composition of phases identified in position B (Figure 33) of the sample manufactured through the *Skin Stripes* geometric sintering strategy as marked with corresponding numbers in the figures.

Position C *(Centre)*

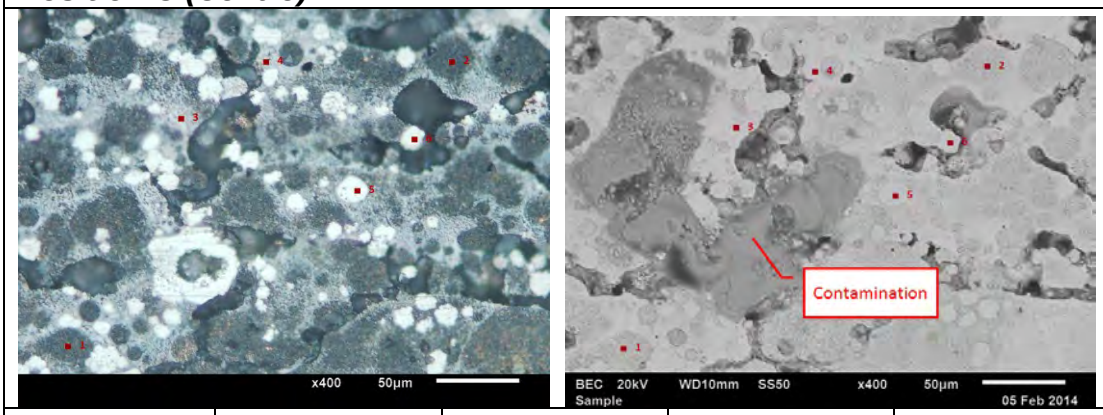

	wt% **Cu**	wt% **P**	wt% **Ni**	wt% **Sn**
1	87.9	1.1	1.0	10.0
2	86.9	1.3	0.8	11.0
3	96.4	2.7	0.5	0.4
4	91.1	5.9	1.5	1.6
5	3.1	0.0	96.9	0.0
6	4.9	0.1	94.8	0.2

Figure 39: Reflected light microscope and comparable SEM images of identical areas with composition of phases identified in position C (Figure 33) of the sample manufactured through the *Skin Stripes* geometric sintering strategy as marked with corresponding numbers in the figures.

The results for the phases present in the sample manufactured through the *Skin Stripes* geometric sintering strategy can be summarized in Table 5 below.

	Copper (Cu)	**Phosphorus (P)**	**Nickel (Ni)**	**Tin (Sn)**	**Description**
Phase 1	90.4 – 96.4%	2.4 – 6.7%	0.4 – 2.1%	0.3 – 5%	White-blue Matrix
Phase 2	86.9 – 94.6%	0.4 – 1.3%	0.4 – 1.7%	3.7 – 11%	Brown round with dendrites
Phase 3	0.9 – 4.9%	0 – 0.1%	94.8 – 99.1%	0 – 0.3%	White blotch

Table 5: Summary of phases present in the sample manufactured through the *Skin Stripes* geometric sintering strategy

Three phases are identified in the sintered microstructure of the sample manufactured through the *Skin Stripes* geometric sintering strategy; the first phase (marked 1 and 2 in Figure 37 to Figure 39) is grains consisting of copper-tin (Cu4Sn-Cu11Sn) with traces of phosphorus and nickel (up to 1.5%), the next phase (marked 5 and 6 in Figure 37 to Figure 39) is nickel with up to 5% copper, the third phase (marked 3 and 4 in Figure 37 to Figure 39) cements the other two phases and consists of copper-phosphorus (Cu2P – Cu7P) with tin (up to 5%) and traces of nickel (up to 2%).

Sample manufactured through the *Skin Chess* geometric sintering strategy

Position A *(Outside)*

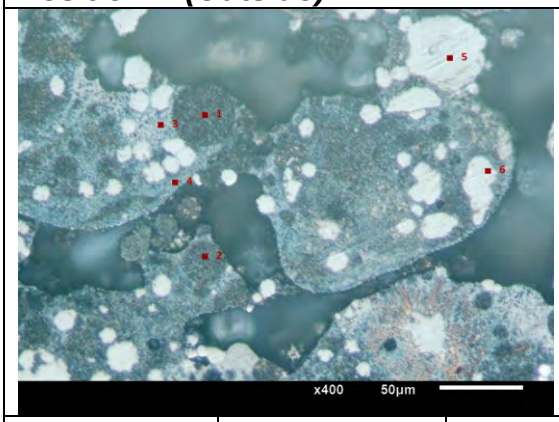

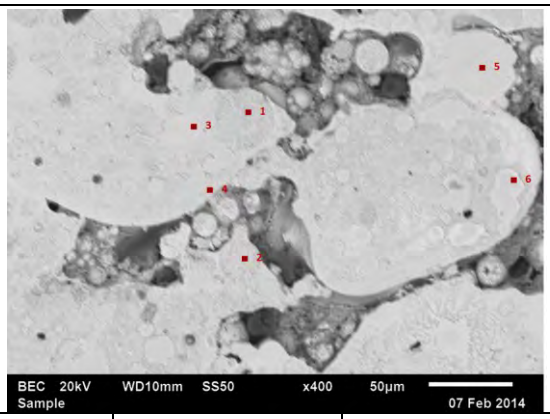

	wt% **Cu**	wt% **P**	wt% **Ni**	wt% **Sn**
1	88.6	0.7	0.6	10.2
2	86.7	1.1	0.4	11.8
3	92.8	4.7	0.7	1.8
4	93.0	1.8	1.3	3.9
5	0.3	0.0	99.7	0.0
6	1.7	0.1	97.9	0.3

Figure 40**:** Reflected light microscope and comparable SEM images of identical areas with composition of phases identified in position A (Figure 33) of the sample manufactured through the *Skin Chess* geometric sintering strategy as marked with corresponding numbers in the figures.

Position B *(Intermediate)*

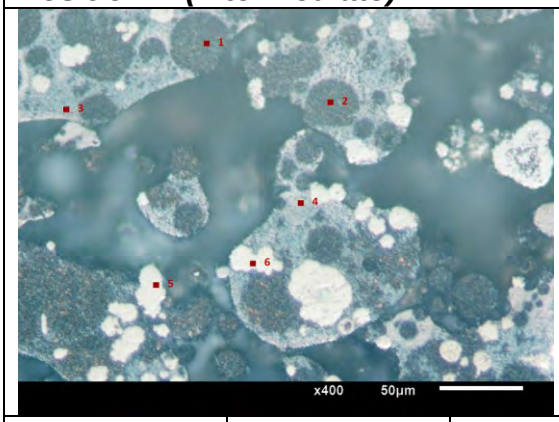

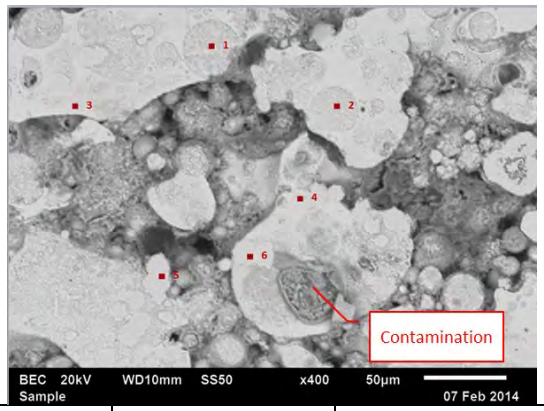

	wt% **Cu**	wt% **P**	wt% **Ni**	wt% **Sn**
1	87.5	0.8	1.6	10.1
2	89.5	5.0	1.5	4.0
3	90.9	4.3	1.4	3.4
4	90.1	4.5	2.7	2.7
5	2.0	0.0	97.8	0.1
6	1.4	0.0	98.4	0.2

Figure 41**:** Reflected light microscope and comparable SEM images of identical areas with composition of phases identified in position B (Figure 33) of the sample manufactured through the *Skin Chess* geometric sintering strategy as marked with corresponding numbers in the figures.

Position C *(Centre)*

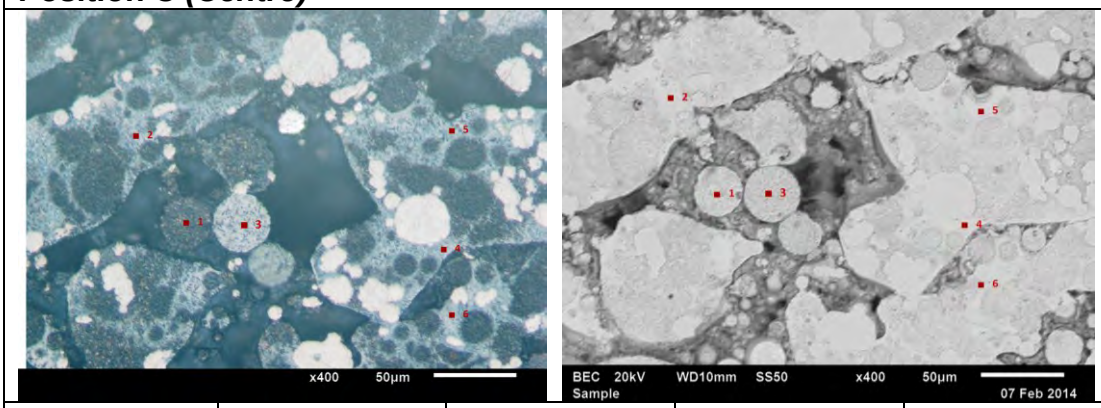

	wt% **Cu**	wt% **P**	wt% **Ni**	wt% **Sn**
1	86.8	0.7	0.8	11.8
2	94.8	3.4	0.3	1.5
3	90.5	8.8	0.2	0.5
4	91.1	6.3	1.2	1.4
5	93.6	4.6	0.3	1.5
6	88.4	6.7	1.5	3.5

Figure 42: Reflected light microscope and comparable SEM images of identical areas with composition of phases identified in position C (Figure 33) of the sample manufactured through the *Skin Chess* geometric sintering strategy as marked with corresponding numbers in the figures.

The results for the phases present in the sample manufactured through the *Skin Stripes* geometric sintering strategy can be summarized in Table 6 below.

	Copper (Cu)	**Phosphorus (P)**	**Nickel (Ni)**	**Tin (Sn)**	**Description**
Phase 1	88.4 – 97.4%	1.6% - 8.8%	0.1 – 2.7%	0.3 – 3.5%	White-blue Matrix
Phase 2	86.7 – 88.6%	0.7 – 1.5%	0.4 – 1.6%	9.6 – 11.8%	Brown round with dendrites
Phase 3	0.3 – 2%	0 – 0.1%	97.8 – 99.7%	0 – 0.3%	White blotch

Table 6: Summary of phases present in the sample manufactured through the *Skin Chess* geometric sintering strategy

From the data presented in Table 6, mainly three phases are identified in the sintered microstructure of the sample manufactured through the *Skin Chess* geometric sintering strategy; the first phase (marked 1 in Figure 40 and marked 1 and 2 in Figure 41 and Figure 42) is grains consisting of copper-tin (Cu10Sn-Cu12Sn) with traces of phosphorus and nickel (up to 1.5%), the next phase (marked 5 and 6 in Figure 40 and Figure 41) is nickel with up to 2% copper, the third phase (marked 3 and 4 in Figure 40, 2,3 and 4 in Figure 41 and 2 – 6 in Figure 42) cements the other two phases and consists of copper-

phosphorus (Cu3P – Cu12P) with tin (up to 4%) and traces of nickel (up to 3%).

3.5 DIMENSIONAL DEFORMATION

A Renishaw Cyclone Coordinate Measuring machine (CMM) with a repeatability of 5 µm was employed to establish the geometry of the samples prior to and after the samples were cut from the base plate. A touch probe with a ball diameter of 5 mm was used to obtain the 3D geometry of the sintered samples while still attached to the base plate. After the samples were cut from the base plate, a laser beam was used to trace the dimensions. Geometric Qualify 2012 software incorporated in the CMM, was used to compare the traced geometry with that of the intended CAD sample artefact. The results were plotted on a 3D model of the CAD geometry and deviations from the actual (CAD) geometry presented in terms of coloured scales.

Figure 43: Samples being traced with the Renishaw Cyclone CMM

Results

Dimensional deformation for the sample manufactured through the *Solid Skin* geometric sintering strategy **before** it was released from the base plate is shown in Figure 44.

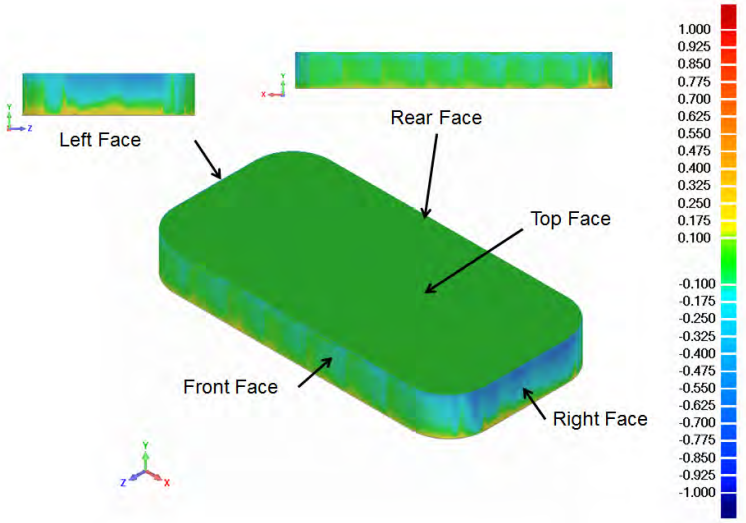

Figure 44: Variation in dimension on the different faces of the sample manufactured through the *Solid Skin* geometric sintering strategy while still attached to the base plate

In the thickness direction (Y-direction), the actual thickness obtained varied between +1.7% and -1.7% from the input thickness of 6 mm. Across the transverse direction (Z-direction) the actual geometry varied between +1% and –1% from the input width of 25 mm, while in the longitudinal direction (X-direction) the actual geometry varied between +1.5% and -1.5% from the input length of 50 mm.

Similar dimensional variations were determined for the samples in which the *Skin Stripes* and *Skin Chess* geometric sintering strategies were employed and the results are shown in APPENDIX G.

Dotted lines were constructed on the coloured deformation diagrams representing dimensional deformation for the samples manufactured through the *Solid Skin*, *Skin Stripes* and *Skin Chess* geometric sintering strategies **after** they were released from the base plate in order to ease interpretation for the reader.

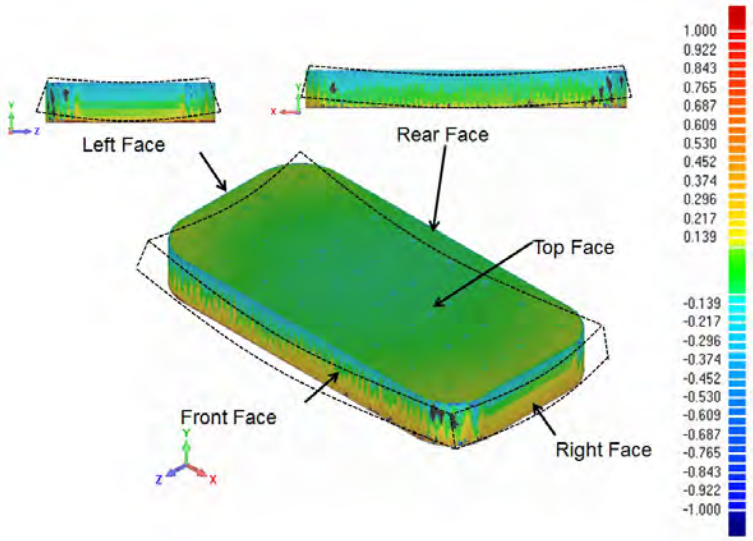

Figure 45: Variation in dimension on the different faces of the sample manufactured through the *Solid Skin* geometric sintering strategy after it was cut from the base plate

In the sample manufactured through the *Solid Skin* geometric sintering strategy **after** it was removed from the base plate (Figure 45) deviations of +2.5% to -2.5% from the input thickness (Y-direction) appeared while up to +1.5% to -1.5% and 3% to -3% deviations were measured in the longitudinal (X) and transverse (Z) directions of the geometry respectively. When considering the top face, it is evident that the face expanded with 0.15 mm (2.5%) near the periphery while shrinkage of 0.15 mm was present in the centre of the top plane.

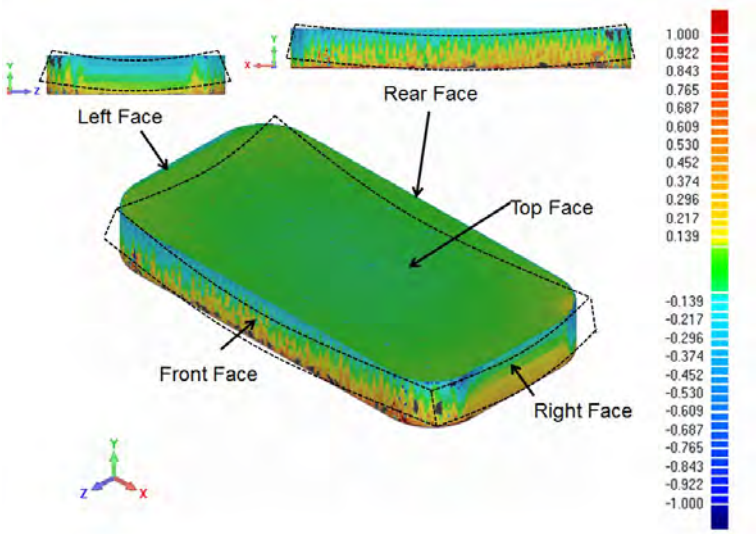

Figure 46: Variation in dimension on the different faces of the sample manufactured through the *Skin Stripes* geometric sintering strategy after it was cut from the base plate

In the sample manufactured through the *Skin Stripes* geometric sintering strategy **after** it was cut from the base plate (Figure 46) dimensional deviations of + 1.8% to - 1.8% and + 3.5% to - 3.5% were measured across the longitudinal and transverse directions of the sample (X- and Z-directions) respectively while deviations across the thickness (Y-direction) varied between +2.5% on the edges and -3% at the centre. On the left end (-X) shrinkage was predominantly present on the top half of the plane while expansion was present for the most part of the right plane (+X).

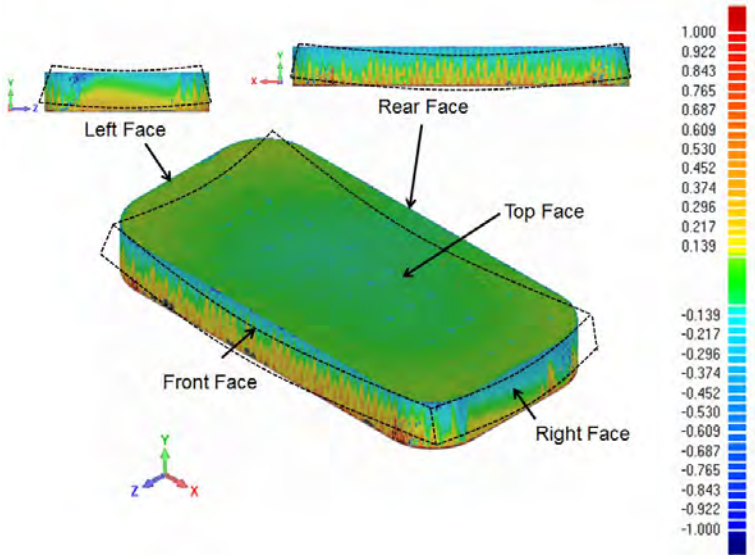

Figure 47: Variation in dimension on the different faces of the sample manufactured through the *Skin Chess* geometric sintering strategy after it was cut from the base plate

In the sample manufactured through the *Skin Chess* geometric sintering strategy **after** it was released from the base plate (Figure 47) deviations of +2.5% to -2.5% from the input thickness (Y-direction) appeared while up to +3.2 to -3.5% and +1.6% to -1.7% deviations were measured across the longitudinal (X) and transverse (Z) directions of the intended geometry respectively.

When comparing the dimensional deformation of the sample while it was still attached to the base plate (i.e. as sintered onto the base plate) to **after** it was cut from the base plate it is evident that more dimensional deformation took place in all directions after the sample was cut from the base plate than before it was released from the base plate. On the top face the sample expanded a bit all around the periphery **after** it was cut from the base plate, while it collapsed somewhat in the middle. The sample therefore curled upwards and sunk in at the top **after** cut from the base plate. The blue dots that appear on the top plane **after** it was cut from the base plate are small inclusions that were modelled and sintered as a provision to ease orientation when sectioning and/or comparing samples. The diameter of the spherical ball used to trace the geometry prior to it was cut from the base plate was too big to penetrate into the dots and could therefore not trace it, but the laser scanner used after the samples were cut from the base plate could penetrate into the dots and trace it.

	Solid Skin	*Skin Stripes*	*Skin Chess*
Front		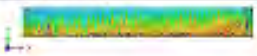	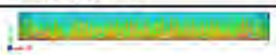
Max Shrinkage	0.5 mm	0.65 mm	0.7 mm
Max expansion	0.7 mm	0.8 mm	0.8 mm
Average difference	0.5 mm	0.55 mm	0.65 mm
Max difference	1.2 mm	1.45 mm	1.5 mm
Back		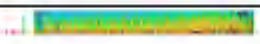	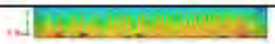
Max Shrinkage	0.65 mm	0.7 mm	0.7 mm
Max expansion	0.1 mm	0.85 mm	0.8 mm
Average difference	0.35 mm	0.6 mm	0.6 mm
Max difference	0.75 mm	1.55 mm	1.5 mm
Left	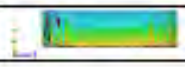	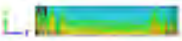	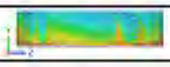
Max Shrinkage	0.4 mm	0.9 mm	0.85 mm
Max expansion	0.2 mm	0.3 mm	0.8 mm
Average difference	0.4 mm	0.35 mm	0.3 mm
Max difference	0.6 mm	0.7 mm	1.65 mm
Right	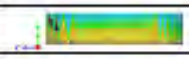	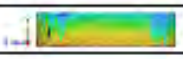	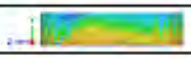
Max Shrinkage	0.7 mm	0.9 mm	0.8 mm
Max expansion	0.2 mm	0.9 mm	0.3 mm
Average difference	0.4 mm	0.4 mm	0.4 mm
Max difference	0.9 mm	1.8 mm	1.1 mm
Top			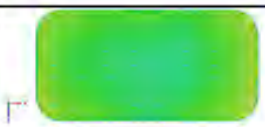
Max Shrinkage	0.15 mm	0.2 mm	0.25 mm
Max expansion	0.15 mm	0.15 mm	0.15 mm
Average difference	0.3 mm	0.25 mm	0.35 mm
Max difference	0.3 mm	0.35 mm	0.35 mm

Table 7: Comparison of deformation in the samples manufactured through the *Solid Skin*, *Skin Stripes* and *Skin Chess* sintering strategies **after** it was cut from the base plate

When comparing the three samples manufactured according to the different geometric sintering strategies, namely *Solid Skin*, *Skin Stripes* and *Skin Chess*, (Table 7) the following was observed:

On the front and back faces, the dimensional deviation was the least in the sample manufactured through the *Solid Skin* geometric sintering strategy, followed by the sample manufactured through the *Skin Stripes* geometric sintering strategy and then the sample manufactured through the *Skin Chess* geometric sintering strategy. On the top face, the sample in which the *Skin Stripes* sintering strategy was employed deformed the least, followed by the sample in which the *Solid Skin* geometric sintering strategy was employed and then the sample in which the *Skin Chess* geometric sintering strategy was employed. In all three the samples, the right side (X) expanded more than the left side (-X), while the sample manufactured through the *Skin Chess* geometric sintering strategy had a much more irregular deformation on the left and right edges than the other two samples. The standard deviation of the traced points from the intended CAD geometry of the sample in which the *Solid Skin* geometric sintering strategy was employed was 0.369 mm while the sample manufactured through the *Skin Stripes* geometric sintering strategy had a standard deviation of the traced points from the intended CAD geometry of 0.344 mm and the sample manufactured through the *Skin Chess* geometric sintering strategy had a standard deviation of 0.449 mm.

From the information obtained for the deformation of the three samples, it can be deduced that the sample manufactured through the *Skin Stripes* geometric sintering strategy is the preferred sintering method as it resulted in less deformation compared to the other two sintering strategies.

3.6 DETERMINATION OF VOIDS PERCENTAGES

The optical microscope images (displayed in Figure 27 to Figure 29) of the nine positions (Figure 26) at the *top*, *middle* and *bottom* of the *outside, intermediate* and *centre* positions (where *bottom* denotes the part of the sample sintered onto the base plate and *outside* is the edge of the sample furthest away from the centre of the sample) of each sample were processed with Olympus Stream Image Analysis software and black spots identified and verified as voids were expressed in terms of an area percentage of the total area exposed to the objective of the microscope. The results are discussed in the paragraphs that follow.

Results

An example of the results obtained for the *outside top* position of the sample manufactured through the *Solid Skin* geometric sintering strategy is shown in Figure 48 where the yellow areas represent solid matter where as the green areas resemble voids. The results are tabulated for the nine positions of each sample in Table 8 to Table 10. Graphs of average area void percentage versus sample position were constructed containing and comparing the results for the three positions along the longitudinal dimension and thickness of each sample (Figure 49 and Figure 50).

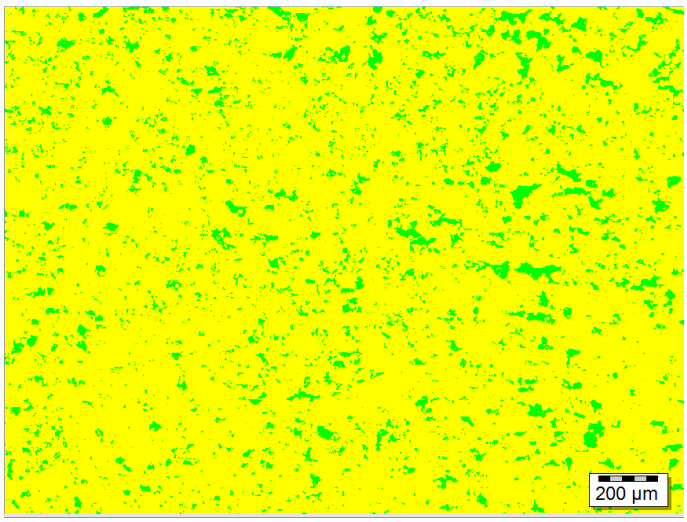

Object Class	Sum (Area) [µm²]	Area Fraction ROI [%]	Object Count [#]	Relative Object Count [%]
2	267628.42	6.95	7346	92.39
1	3584739.11	93.05	605	7.61

Figure 48: Area percentage of voids (average 6.95%) at the *outside top* position of the sample manufactured through the *Solid Skin* geometric sintering strategy as expressed by Olympus Stream Images Analysis software

Solid Skin				
	Outside	**Intermediate**	**Centre**	**Average**
Top	8%	13.1%	8.6%	9.9%
Middle	6.9%	13.3%	10.4%	10.2%
Bottom	8.5%	14.3%	9%	10.6%
Average	7.8%	13.6%	9.3%	**10.2%**

Table 8: Results of the area percentage of voids at the *outside, intermediate* and *centre* positions of the sample manufactured through the *Solid Skin* geometric sintering strategy for three depths, namely *top, middle* and *bottom*

Skin Stripes				
	Outside	**Intermediate**	**Centre**	**Average**
Top	6%	7.3%	7.3%	6.9%
Middle	8%	5.2%	7.3%	6.8%
Bottom	11.2%	8.2%	7.2%	8.9%
Average	8.8%	6.9%	7.3%	**7.5%**

Table 9: Results of the area percentage of voids at the *outside, intermediate* and *centre* positions of the sample manufactured through the *Skin Stripes* geometric sintering strategy for three depths namely *top, middle* and *bottom*

Skin Chess				
	Outside	**Intermediate**	**Centre**	**Average**
Top	19.3%	17.3%	17.7%	18.1%
Middle	25.2%	30.3%	26.4%	27.3%
Bottom	31.4%	32.6%	28.9%	31%
Average	25.3%	26.7%	24.4%	**25.5%**

Table 10: Results of the area percentage of voids at the *outside, intermediate* and *centre* positions of the sample manufactured through the *Skin Chess* geometric sintering strategy for three depths namely *top, middle* and *bottom*

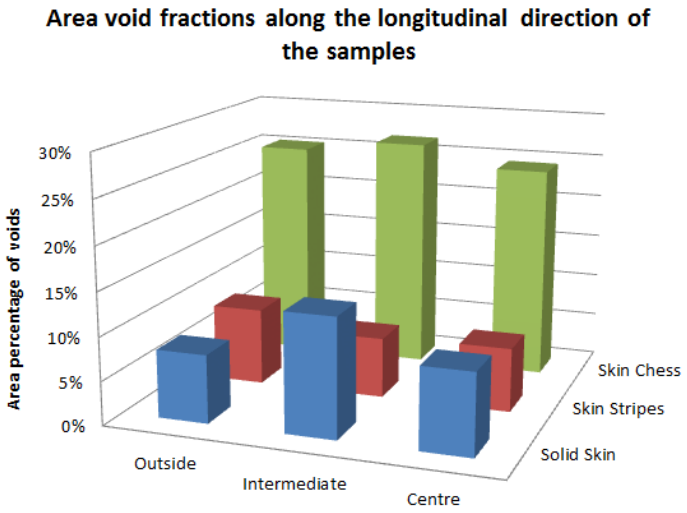

Figure 49: Graph of average area percentage of voids across the longitudinal dimensions of the three samples

From the graph in Figure 49 it can be deduced that the porosity in the sample manufactured through the *Solid Skin* geometric sintering strategy increases from the *outside* to the *intermediate* position and decreases again at the *centre* position. The porosity in the sample manufactured through the *Skin Stripes* geometric sintering strategy is consistent and decreases slightly from the *outside* to the *centre* positions while the porosity in the sample manufactured through the *Skin Chess* geometric sintering strategy is consistent across the longitudinal direction of the sample.

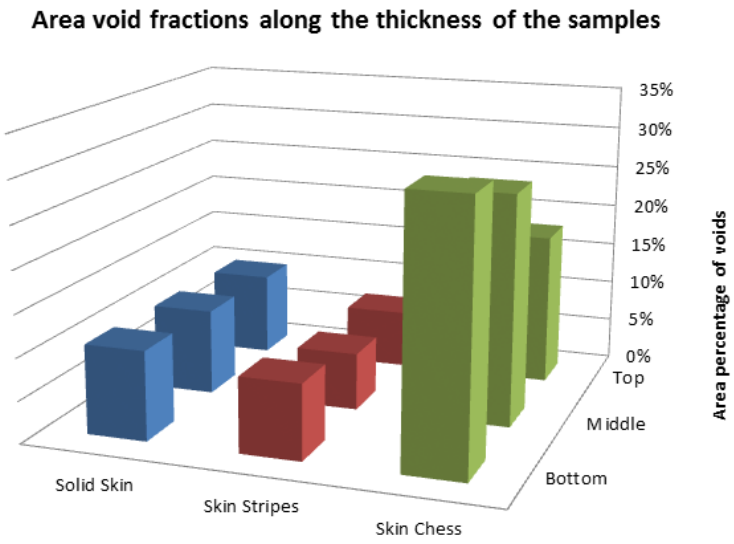

Figure 50: Graph of average area percentage of voids across the thickness of the three samples

The data represented in the graph (Figure 50) indicates that the porosity of the sample manufactured through the *Solid Skin* geometric sintering strategy remains almost unchanged across the thickness of the sample while it decreases slightly from the *bottom* to the *top* of the sample manufactured through the *Skin Stripes* geometric sintering strategy. The porosity in the sample manufactured through the *Skin Chess* geometric sintering strategy reduces significantly from the *bottom* to the *top* of the sample.

From the results it is evident that much higher porosities exist in all positions of the sample manufactured through the *Skin Chess* geometric sintering strategy (as qualitatively observed in Figure 40 to Figure 42) compared to the other two samples.

The average percentage of voids in the sample manufactured through the *Skin Stripes* geometric sintering strategy was 7.5%, followed by the sample manufactured through the *Solid Skin* geometric sintering strategy with a percentage of voids of 10.2% and lastly the sample in which the *Skin Chess* geometric sintering strategy was employed with a percentage of voids of 25.5%.

CHAPTER 4: DISCUSSION AND CONCLUSION

The semi-quantitative XRF analyses of the bulk powder (Table 1) confirms that the powder comprised of copper, phosphorus, nickel and tin according to the supplier's (EOS) claim and specification (Table 1) with the percentage copper and nickel in this powder being in the middle of the specified range while tin is at the lower specified limit. The weight percentage phosphorus in this powder (0.5 wt%) is however below the lower limit of the supplier claim (1 wt% - 5 wt%).

SEM observations of a sample of the powder indicate that the powder consists of smaller and larger spherical grains, occasional lenticular grains and agglomerates of variable sizes (Figure 12 and Figure 13).

From the particle size distribution analysis presented in Figure 15 it is evident that the majority (34%) of the grains measured have a grain size of 10 - 20 µm while the rest of the grains have sizes that vary between 0 – 10 µm (22%), 20 – 30 µm (21%), 30 – 40 µm (24%) and 40 – 45 µm (7%) (Figure 15). When the agglomerates (that make up 20% of the powder) are removed from the evaluation and the data reworked, similar results are obtained. Besides, from the data presented in Figure 15 and Figure 16 it appears that a bi-modal particle size distribution exists in the powder regardless of whether the agglomerates are included or excluded from the analyses.

From the analysis of the SEM images of the powder, based on the data in Table 3 and Figure 14, the conclusion is made that the *DM 20* powder consist of three phases; the smaller (~5 µm) spherical grains (Figure 14) represent Phase 1 in Table 3 and consist of copper-phosphorus (Cu8.3P to Cu2P with up to 0.5% Ni), the near spherical grains (~40 µm in Figure 14) represent another phase (Phase 2 in Table 3) with the composition of copper-tin (Cu15Sn to Cu5Sn with up to 1% Ni) and the agglomerates (45 µm in Figure 14) represent Phase 3 in Table 3 with a composition of mainly nickel (Ni – Ni5Cu). The occasional lenticular grains (50 µm in Figure 14) consist of

grains of possible different compositions that were cemented due to previous melting.

In the Cu-Ni phase diagram (Figure 51) it is evident that nickel is completely soluble in copper above about 355 ºC which may be the reason for the variation in concentrations of Ni in the phases according to the analyses.

From the phase diagram in Figure 52 it is observed that the lowest melting point for the two phase Cu-P system will be 714 ºC (at the eutectic at 8.3 wt% P) provided that the phase Cu_3P is present in the powder, but the analysis of the phases in the powder proved that this phase was not present in any of the evaluated phases. However the weight percentage phosphorus varies essentially between 2 and 8 wt% (Table 3) and this means that for these compounds a melt of the Cu-P phases will be obtained at 714 ºC if the powder is exposed to heat for long enough. It is thought that the Cu-P phases are therefore the lower melting point components in the powder which are expected to bring down the melting temperature of the system in order for liquid phase sintering to take place.

If near 13.5 wt% Sn is present in the sample, and the sintering temperature would reach 798 ºC or above, it would give rise to the formation of β-phases and intermetallic compounds that one would want to avoid (Figure 53). However, the majority of the Cu-Sn phases analysed according to a map of image analysis are below 13.5%.

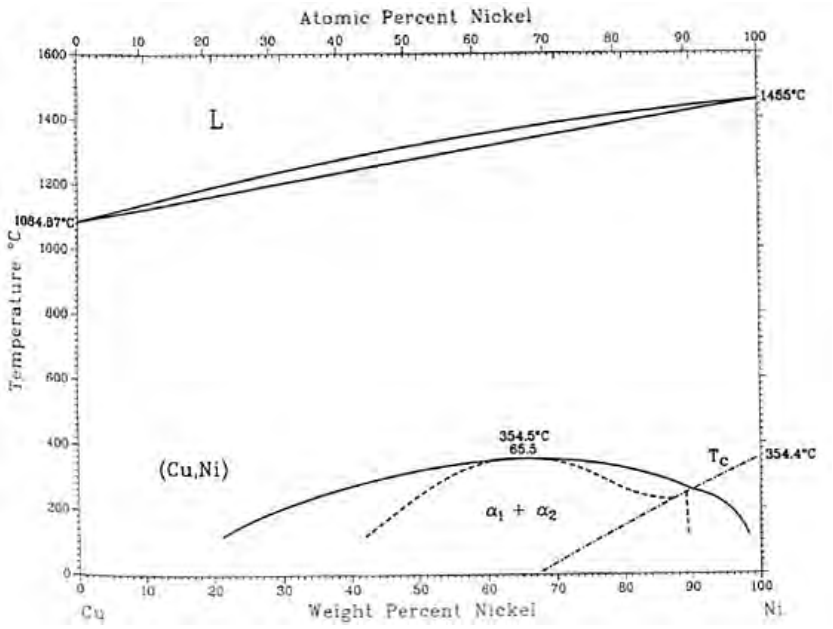

Figure 51: Binary copper-nickel phase diagram (ASM International, 1997)

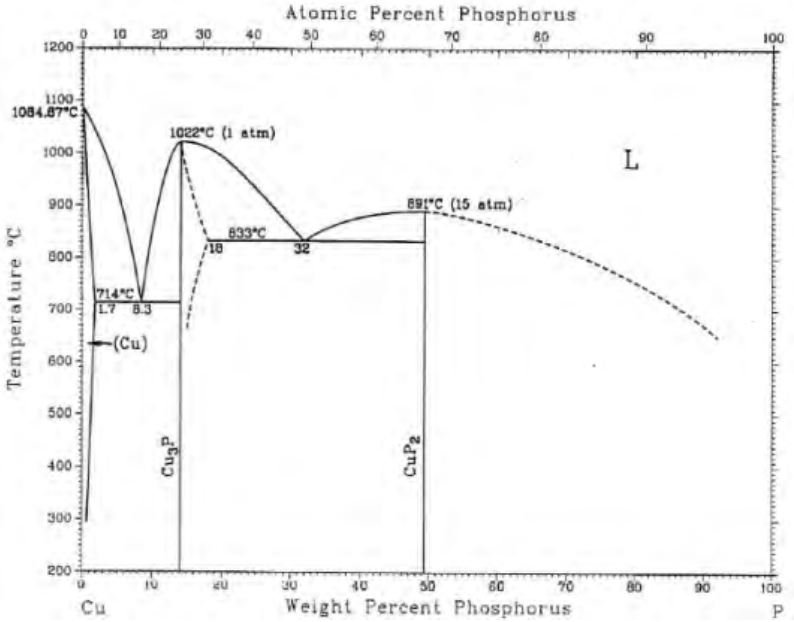

Figure 52: Binary copper-phosphorus phase diagram (ASM International, 1997)

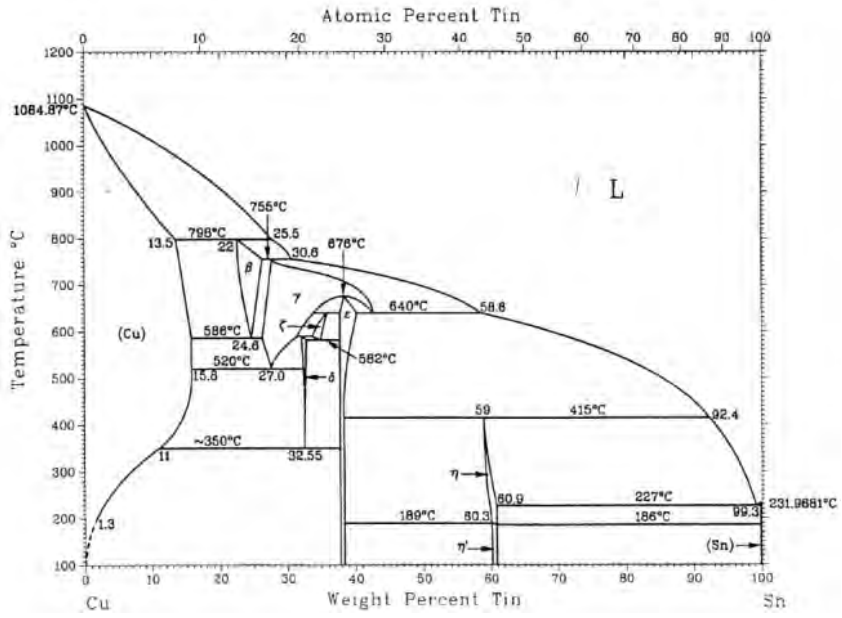

Figure 53: Binary copper-tin phase diagram (ASM International, 1997)

From the phase relations and SEM EDS analyses (Figure 34 to Figure 42) of the sintered samples it is thought that the white-grey (e.g. phase 3 and 4 in Figure 34) copper-phosphorus glass (Cu2P-Cu12P with up to 5% Sn and up to 3% Ni) cementing the other phases served as the binder which agrees with the data previously discussed in the phase chemistry of the powder. The copper-tin (Cu4Sn-Cu12Sn with traces of P and up to 1.5% Ni) phases (e.g. phases 1 and 2 in Figure 34) cemented in the binder are the structural elements. The deduction can therefore be made that the liquid phase sintering did indeed take place at ~714 ºC (eutectic temperature in Cu-P phase diagram in Figure 52). Furthermore it is found that the white nickel (e.g. phases 5 and 6 in Figure 34) phases found in the powder were not affected (95 – 100 wt% Ni) by the sintering process (nor did it contribute to sintering or any other property) and are also cemented in the binder.

The composition of the copper-tin phases in all three the samples varied between ~5 - 15 wt% Sn, while the copper-phosphorus phases varied between 2 – 9 wt% P which is typically the ranges found in the powder. These compositions were plotted on a triangular graph in Figure 54 and the spread of the two phases (encircled with like colours representing each sample) as well as the outliers are clearly visible for each sample. It is evident

that traces of Sn are present in the Cu-P phases and small traces of P in the Cu-Sn phases. The encircled areas (Figure 54b) indicate the range in which the phases are present for each sample.

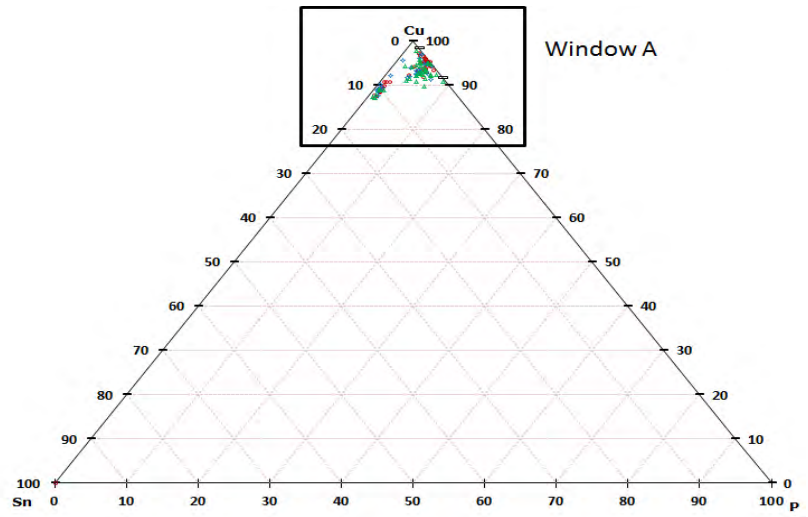

Figure 54a: Ternary Cu-Sn-P diagram with phases identified in the sintered samples plotted

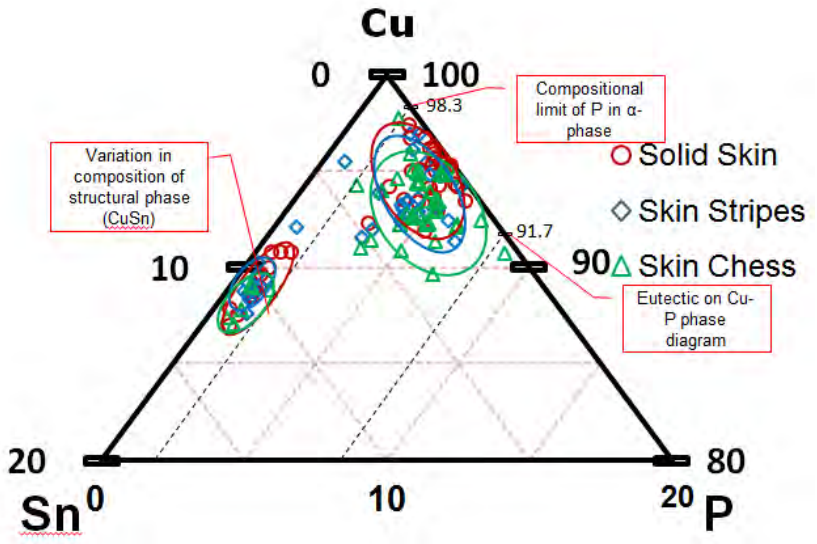

Figure 54b: Window A of the ternary Cu-Sn-P diagram with phases identified in the sintered samples for each sample plotted and ranges in which the phases are present encircled

The maximum limit of P in the alpha phase of the Cu-P phase diagram (1.7% P) and the eutectic (8.3% P) are indicated on the Cu-P axis of the triangular compositional diagram (Figure 54b). When considering the compositions of the analysed Cu-P glass phases (binder) (represented in the triangular compositional diagram, Figure 54b) for the samples manufactured with the

different geometric sintering strategies it is apparent that the wt% P in the samples ranges between 1.7 and 8.3 (between the α-phase limit and eutectic of Cu-P phase diagram) for all the samples. The data available indicate that the liquid phase (Figure 54b) acting as a binder in the sample manufactured through the *Solid Skin* and *Skin Stripes* geometric sintering strategies tend to vary in composition less than in the sample produced with the *Skin Chess* geometric sintering strategy.

	Average wt% P in the CuP glass phase	**Deviation of average wt% P in the CuP glass phase from the eutectic**
Solid Skin	4.9	3.4
Skin Stripes	4.5	3.8
Skin Chess	5	3.3

Table 11: Average wt% P and deviation of average wt% P in the Cu-P glass phase from the eutectic composition of the samples manufactured through the *Solid Skin, Skin Stripes* and *Skin Chess* geometric sintering strategies

Table 11 contains the results of analyses carried out on the data points plotted in Figure 54. The data points were analysed in terms of the deviation of the average wt% phosphorus in the binder from the Cu-P eutectic (8.3% P) in the Cu-P glass binder of each sample. From Table 11 it is evident that the average composition in the sample manufactured through the *Solid Skin* geometric sintering strategy is 4.9 wt%, which is 3.4% less than the eutectic composition (8.3 wt%), the average composition in the sample manufactured through the *Skin Stripes* geometric sintering strategy is 4.5 wt% (3.8% less than the eutectic composition) and the average composition in the sample manufactured through the *Skin Chess* geometric sintering strategy is 5 wt% (3.3% less than the eutectic composition). It is thought that when the Cu-P phases are exposed to heat for long enough, such that more effective sintering would take place (and consequently better equilibration), the composition of the Cu-P glass phase will approach the composition of the eutectic at 8.3 wt% P. The deviation of the percentage phosphorus in the glass binder from the eutectic (8.3%) is on average 3.5% lower than the typical composition of a Cu-P glass at the eutectic in all the samples and may

be ascribed to the fact that sufficient equilibration did not take place during sintering.

The data produced in Figure 54 and Table 11 is thought to be inconclusive to confirm or negate the findings by Ning *et al.* (2005) who stated that a less consistent microstructure will be found in samples where shorter scanning vector lines (samples manufactured through the *Solid Skin* and *Skin Chess* sintering strategies*)* were employed, as the uncertainties of the analyses were not determined and therefore the uncertainties in the wt% phosphorus variation in the composition of the binder (glass phase) are also not significant.

Additionally, if for instance phase 5 in Figure 36 is inspected in more detail in the different sintering configurations, the compositions of the smaller grains embedded in the binder phase are unknown and has not been analysed and may have a composition of CuP with maximum 1.7% P or Cu_3P.

Although, according to Zhu *et al.* (2005), the nickel is said to grow during furnace sintering and compensate for shrinkage and results in an increase in the yield strength of the material (Zhu *et al*., 2005), it is clear that at the temperatures of laser sintering and the limited dwell time of the laser beam, no time is available for the diffusion of nickel and its consequent growth for the purpose of shrinkage compensation nor did the nickel (agglomerates of nickel) take part in any reaction or formed any compound that could contribute to cementing of sintered artefacts. The sintering temperature of ~714 ºC was too low for the nickel to melt and consequently the nickel could not grow or shrink through the forming of a Ni-glass or glass with other elements such as copper. It is however thought that the nickel, as previously absorbed by the copper and shown in the analysis of phases in the powder (Table 3), could strengthen the Cu-Sn and Cu-P through solid-solution strengthening during the manufacturing process of the powder, but not through the sintering process. It is evident that excessive nickel exists in the powder and it is thought that it would be financially beneficial if the nickel composition in the

powder can be reduced or even extracted from the powder available to test the hypothesis.

From the inspection of the microstructures of the sintered samples, it was observed that qualitatively high porosities were obtained in all three samples, in particular the sample manufactured through the *Skin Chess* geometric sintering strategy.

In the microstructures of the samples manufactured through the *Skin Stripes and Skin Chess* geometric sintering strategies, a less dense microstructure (*skin*) was separated from a denser microstructure (*core*) with a crack (Figure 28 and Figure 29). It was determined (Figure 69 and Figure 73) that the separation occurred on the skin boundaries as defined by the sintering geometric surface paths shown in Figure 19 and Figure 20 which occurred as a result of the difference in sintering parameters (and thus different energy inputs) between the *skins* and the *core*.

From the deformation diagrams presented in Section 3.5 it was determined that more deformation took place **after** the samples were released from the base plate than **before** it was released from the base plate and that this is an indication that high residual stresses were present in the samples while they were attached to the base plate. The stresses were released to some extent **after** they were cut from the base plate and the samples deformed, curling upwards and inwards at the top.

From the data in Figure 47 it is revealed that the sample manufactured through the *Skin Chess* geometric sintering strategy exhibits more dimensional deformation on all the faces than the other two samples. The above deduction is further confirmed by the standard deviations of the traced points from the intended CAD geometry. The sample manufactured through the *Skin Stripes* geometric sintering strategy, had the least dimensional deformation, followed by the sample manufactured through the *Solid Skin* geometric sintering strategy and then the sample manufactured through the *Skin Chess* geometric sintering strategy.

Although the material data sheet specifies a typical part accuracy of ±50 µm, dimensional deviations of up to 70, 90 and 85 µm were experienced in the relatively small (50 x 25 x 6 mm) samples manufactured through the *Solid Skin*, *Skin Stripes* and *Skin Chess* geometric sintering strategies respectively. Furthermore, it is noted that the percentage dimensional deviation was more (~ ±3%) across the transverse directions (25 mm width) than across the longitudinal directions (~±1.5% over 50 mm length) of the samples (Figure 45 to Figure 47). It is projected that the dimensional deviation of larger parts of up to 250 x 250 x 200 mm (maximum building capacity of the machine according to EOS (2007a)) will be ±7 mm, which is far more than the ± 50 µm specified.

According to the material data sheet (EOS, 2007c) a minimum porosity of 8% is to be expected for direct metal laser sintered parts sintered with *DM 20* powder. The average porosity obtained of the sample manufactured through the *Skin Stripes* geometric sintering strategy was close to this value at 7.5% while the porosities of the samples manufactured through the *Solid Skin* and *Skin Chess* geometric sintering strategies were much higher at 10% and 25% respectively. Furthermore it is evident from the bar graphs in Figure 49 and Figure 50 that the sample manufactured through the *Skin Stripes* geometric sintering strategy had the lowest and a more consistent porosity across the height and longitudinal direction compared to the other two samples.

In all three the samples, the average porosity decreased from the first layers deposited to the last layers deposited (Figure 50 where “bottom” denotes the first layers deposited and “top” denotes last layers deposited). It is thought that this can be attributed to expansion (Figure 45 to Figure 47) at the bottom near the base plate and contraction at the top (last sintered layers) allowing for higher densities at the top than at the bottom of the sample. This is attributed to a slower cooling rate associated with the last sintered layers compared to the first sintered layers onto the base plate. Cooling at the base plate will be rapid via conduction through the metal base (which was heated to 80 ºC only) onto which the first sintered layer was sintered resulting in less glass binder and more porosity developing in the matrix. Many more layers

were sintered after the first, resulting in more heat accumulating as more layers were sintered one onto the other. Higher sintering temperatures were reached on the last sintered layers associated with more glass-binder development (e.g *top* in Figure 27) and less deformation in the last sintered layers due to the binder that was exposed to higher sintering temperatures for longer.

In the *intermediate* positions of the sample manufactured through the *Solid Skin* geometric sintering strategy, more white-grey Cu-P phases and fewer voids were observed (Figure 27 and Figure 30). This is not in agreement with the results obtained from the area percentage of voids as higher porosity values were obtained in the *intermediate* position of the sample manufactured through the *Solid Skin* geometric sintering strategy.

When employing Gu *et al.*'s (2006) formula to determine the *'energy density by volume'* it is evident from the calculations in Table 12 that the sample manufactured through the *Skin Stripes* geometric sintering strategy, had the highest energy input (42 Ws/m^3), followed by the sample manufactured through the *Solid Skin* geometric sintering strategy (32 Ws/m^3) and then the sample manufactured through the *Skin Chess* geometric sintering strategy (18 Ws/m^3). It is therefore thought that (when no consideration is given to the geometric sintering paths) the higher densities obtained in the sample manufactured through the *Skin Stripes* geometric sintering strategy may be attributed to more effective sintering that took place due to a higher value obtained for the '*energy density by volume'.*

Solid Skin	*Skin Stripes*	*Skin Chess*
$\eta_{Solid} = \frac{P}{vhd}$ $= \frac{190}{500 \times 0.2 \times 0.06}$ $= 31\ Ws/m^3$	$\eta_{Solid} = \frac{P}{vhd}$ $= \frac{190}{250 \times 0.3 \times 0.06}$ $= 42\ Ws/m^3$	$\eta_{Solid} = \frac{P}{vhd}$ $= \frac{190}{875 \times 0.2 \times 0.06}$ $= 18\ Ws/m^3$

Table 12: Determination of 'Energy density by volume' for the different scanning strategies

When the sintering strategy is considered independently of any other parameter variables, it is thought that that the sample manufactured through the *Skin Chess* sintering strategy would experience the fastest cooling as the heat generated in the individual sintered blocks would be conducted to the sides and each individual block would be allowed to cool before the powder in the in-between blocks is sintered. The faster cooling rate would then result in a more porous microstructure due to less liquid phases (Figure 49 and Figure 50). It is also thought that the sample in which the *Solid Skin* sintering strategy was employed would experience a faster cooling rate than the sample manufactured through the *Skin Stripes* sintering strategy. Each sintered strip compiled from shorter scan tracks (*Solid Skin* sintering strategy) will be allowed to cool via conduction to the outsides and convection to the atmosphere, before the laser will start with a neighbouring strip (consisting of smaller scan tracks), parallel to the first. In the sample manufactured through the *Skin Stripes* sintering strategy, where longer scan tracks were utilised, the start of the long scan track would not be allowed to cool sufficiently before the second track is sintered parallel to the first. Less time therefore passes before the laser re-heats the initial track and moves on to the successive tracks, resulting in heat build-up from one parallel track to the next. This would consequently result in slower cooling, and therefore better sintering and consequently more liquid phases and higher densities, to occur (dependant on the accompanying volume change).

The porosity and dimensional deformation of the sample manufactured through the *Skin Stripes* sintering strategy is the lowest and it is therefore deduced that it is the better sintering strategy of the three strategies in order to generally obtain parts with the highest possible density and accuracy. It is thought that an even more consistent porosity and less dimensional deformation would be obtained if the powder system could be optimised in terms of the phases present in the powder and the initial compact density of the powder.

The particle sizes in this powder vary from 2 μm – 45 μm and are characterized by a bi-modal particle size distribution. This distribution is not ideal for obtaining high sintering densities as it will not as effectively fill pore spaces as a normal distribution would. Also, in this work, it was observed that the nickel is present in the powder in the form of agglomerates. In this respect, Khang (2005) reported that agglomerates present in sintered powder samples will give rise to higher porosities which may contribute to the porosities obtained in this sample.

According to Wang *et* al. (2007), Gu *et al*. (2007), Simchi *et al*. (2003), Dong *et al.* (2009) and Tang *et al*. (2003) who did work on polystyrene, titanium, iron-based and copper-based alloys higher energy inputs (smaller laser focus diameter, slower laser speed, higher laser power, thinner layers, smaller scan line spacing etc.) result in higher densities and more dimensional deformation (Wang *et* al., 2007; Gu *et al*., 2007; Simchi *et al*., 2003, Dong *et al.,* 2009; Tang *et al*., 2003), which is contradictory to the findings in this work - when comparing the deformation with the void fractions, more deformation took place in the sample manufactured through the *Skin Chess* geometric sintering strategy where higher void fractions, in other words, lower densities, were present compared to the samples manufactured through the *Solid Skin* and *Skin Stripes* geometric sintering strategies.

It is thought that in the samples manufactured through the *Solid Skin* and *Skin Chess* geometric sintering strategies, more energy was absorbed from the short neighbouring tracks which resulted in more dimensional deformation than in the *Skin Stripes* sample. This data correlates with the findings of Ning *et al*. (2005) who, on Cu-based powders, determined experimentally that shorter laser scan lines resulted in more dimensional deformation.

In summary, this research has contributed towards the characterisation of the *DM 20* powder that would contribute to further simulation, modelling and improvement of porosities and deformations of sintered samples as this EOS M250 system is still fully operational at the CRPM. The *Skin Stripes* geometric sintering strategy proved to be the better sintering strategy of the

three standard strategies investigated for the sintering of *DM 20* powder as it resulted in less porosity and dimensional deformation in the sintered samples than the other sintering strategies.

CHAPTER 5: RECOMMENDATIONS

With the aim to optimise the *DM 20* material powder, it is recommended that the amount of Cu-P phases (binder) in the powder be increased such that the amount of phosphorus in the powder is at least near the higher levels specified (5%). This should result in more glass binder and higher densities in the sintered samples.

It is also recommended that the nickel agglomerates (or even the Ni content of the original material) be reduced or be removed from the *DM 20* powder system as it does not participate in the sintering process. This will not only bring down the cost of the powder but should result in a more compact powder density.

Furthermore, it is recommended that the base plate be heated to a higher temperature in order to minimise the temperature losses during deposition and sintering of base layers.

It is advised that the *Skin Stripes* geometric sintering strategy be utilised in the future when components are sintered with the *DM20* powder system on the EOSINT M250 Xtended machine at the CRPM. It is, however, suggested that no distinction be made between the *skin* and the *core* parameters and that the whole component be sintered with the *core* parameters only, to prevent cracks from forming on the skin boundaries.

It is worthwhile that post processing techniques be investigated in order to relieve residual stresses while the samples are still attached to the base plate.

REFERENCES

ASM International. 1995. Volume 2. *Properties and Selection: Nonferrous Alloys and Special-Purpose Materials*.

DAI, K. & SHAW, l. 2004. *Thermal and mechanical finite element modelling of laser forming from metal and ceramic powders.* Acta Materialia, 52: 69-80.

DONG, L., MAKRADI, A., AHZI, S. & REMOND, Y. 2009. *Three-dimensional transient finite element analysis of the selective laser sintering process*. Journal of Materials Processing Technology, 209: 700-706.

EOS (Electro Optical Systems). 2004. Material data sheet. MS/01.04

EOS (Electro Optical Systems). 2007a. *EOSINT M250 Xtended operators manual.*

EOS (Electro Optical Systems). 2007b. *Basic training manual*. EOSINT M270 Xtended.

EOS (Electro Optical Systems). 2007c. *Material data sheet.* MS/10.07

EOS (Electro Optical Systems). 2012. EOS, *EC Safety data sheet*, Direct Metal 20, version 1.1.0/GB.

GAO, Y., XING, J., ZHANG, J., LUO, N. & ZHENG, H. 2008. *Research on measurement method of selective laser sintering (SLS) transient temperature*. Optik, 119: 618-623.

GERMAN, R.M., SURI, P. & PARK, S.J. 2009. *Review: liquid phase sintering*. Journal of Material Science, 44(1): 1-39.

GU, D., SHEN, Y. & LU, Z. 2009. *Microstructural characteristics and formation mechanism of direct laser-sintered Cu-based alloys reinforced with Ni particles.* Materials and Design, 30: 2099-2107.

GU, D., SHEN, Y., FANG, S. & XIAO, J. 2007. *Metallurgical mechanisms in direct laser sintering of Cu-CuSn-CuP mixed powder.* Journal of Alloys and Compounds, 438: 184-189.

GU, D.D., SHEN, Y.F., YANG, J.L. & WANG, Y. 2006. *Effects of processing parameters on direct laser sintering of multicomponent Cu based metal powder.* Material Science and Technology, 22(12): 1229-1455.

KALPAKJIAN, S. & SCHMID, S. 2006. *Manufacturing engineering and technology.* 5th Edition. Pretence Hall.

KHAING, M.W., FUH, J.Y.H. & Lu, L. 2001. *Direct metal laser sintering for rapid tooling: Processing and characterization of EOS parts.* Journal of Materials Processing Technology, 113: 269-272.

KANG, S.J.L. 2005. *Sintering Densification, Grain Growth and Microstructure.* Butterworth Hennemann, Elsevier.

KIBBLE, K., STANFORD, M. & LINDOP, M. 2007. *Structural Integrity of Rapid Manufactured Laser Sintered Plastic and Metal Parts*.

MA, J. & LIM, L.C. 2002. *Effect of particle size distribution on sintering of agglomerate-free submicron alumina powder compacts*. Journal of European Ceramic Society, 22: 2197–2208.

MATSUMOTO, M., SHIOMI, M., OSAKADA, K. & ABE, F. 2002. *Finite element analysis of single layer forming on metallic powder bed in rapid prototyping by selective laser processing.* International Journal of Machine Tools and Manufacture, 42 : 61-67.

Neikov, I.D., Naboychenko, S., Mourachova, I.B., Gopienko, V.G., Frishberg, I.V. and Lotsko, D.V. 2009. *Handbook of Non-Ferrous Metal Powders: Technologies and Applications*. Elsevier.

NING, Y., WONG, Y.S. & FUH, J.Y.H. 2005. *Effect and control of hatch length on material properties in the direct metal laser sintering process.* Journal of Engineering Manufacture, 219(B): 15-25.

PATIL, R.B. & YADAVA, V. 2007. *Finite element analysis of temperature distribution in single metallic powder layer during metal laser sintering.* International Journal of Machine Tools and Manufacture, 47: 1069 – 1080.

SENTHILKUMARAN, K., PANDEY, P.M & RAO, PVM. 2009. *Influence of building strategies on the accuracy of parts in selective laser sintering*. Materials and Design, 30: 2946-2954.

SIMCHI, A. 2006. *Direct laser sintering of metal powders: Mechanism, kinetics and microstructural features*. Material Science and Engineering, 428(A): 148-158.

SIMCHI, A., PETZOLDT, F. & PHOL, H. 2003. *On the development of direct metal laser sintering for rapid tooling.* Journal of material processing technology, 220: 183-190.

SMITH, W.F. 1996. Principles of Material Science & Engineering. 3rd ed. India: McGraw-Hill.

TANG, Y., LOH, H.T., WONG, Y.S., FUH, J.Y.H. & WANG, x. 2003. *Direct laser sintering of a copper-based alloy for creating three-dimensional metal parts*. Journal of Materials Processing Technology, 140: 368-372.

WANG, R.J., WANG, L., ZHAO, L. & LIU, Z. 2007. *Influence of process parameters on part shrinkage in SLS.* Journal of Advanced Manufacturing Technology, 33: 498-504.

ZHU, H.H., LU, L. & FUH, J.Y.H. 2005. *Study on shrinkage behaviour of direct laser sintering metallic powder*. Journal of Engineering Manufacture, 220(B): 183-190.

ZHU, H.H., LU, L., FUH, J.Y.H. 2003. *Development and characterization of direct laser sintering Cu-based metal powder.* Journal of Materials Processing Technology, 140: 314-317.

APPENDIX A: EXPOSURE TYPES

- Skywriting: During skywriting of the inner area the laser beam accelerates and decelerates outside the exposure area, during which the laser is switched off. Two types of skywriting are possible, namely sequential skywriting and continuous skywriting. When sintering a hollow rectangular section for example, the laser will follow parallel scan lines in which the laser is switched on when material needs to be sintered and switched off when passing the hollow section. During sequential skywriting, the laser will first sinter uninterrupted areas where after it will sinter the material behind a gap. During continuous skywriting, the laser will start sintering on one side and continue across the part until the other end is sintered. The difference in laser sintering path is shown in Figure 56 and Figure 57 (EOS, 2007b).

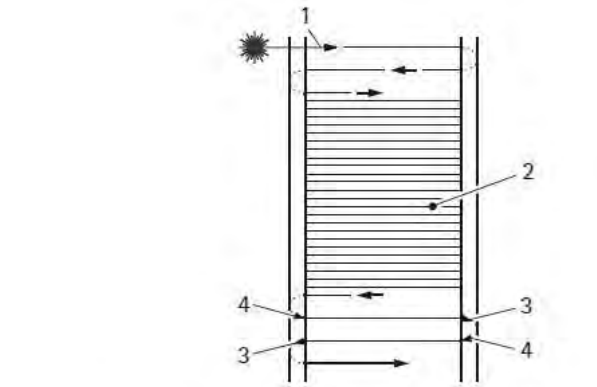

1 Direction of of the exposure by the laser
2 Building area, hatch lines
3 Retardation phase
4 Acceleration phase

Figure 55: Skywriting (EOS, 2007b)

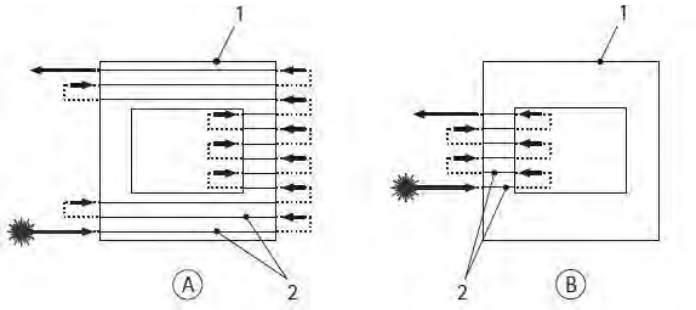

1 Contour
2 Hatch lines
A First exposure phase
B Second exposure phase

Figure 56: Sequential skywriting (EOS, 2007b)

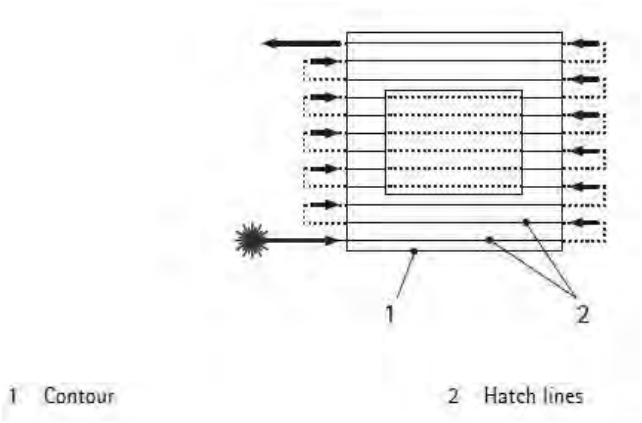

Figure 57: Continuous skywriting (EOS, 2007b)

- Stripes: This is the exposure of parallel lines, without skywriting taking place. (EOS, 2007b)

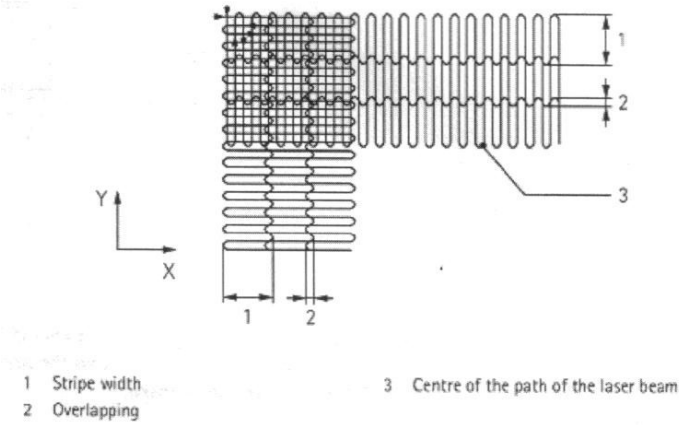

Figure 58: Exposure type, Stripes (EOS, 2007b)

- Squares: With this type of exposure, no Skywriting takes place. Exposure is done in squares to prevent the distortion of parts. The size of the squares can be set by the machine operator. Unexposed gaps are left between the squares and after the exposure of all the squares, the gaps are exposed at a second speed (EOS, 2007b).

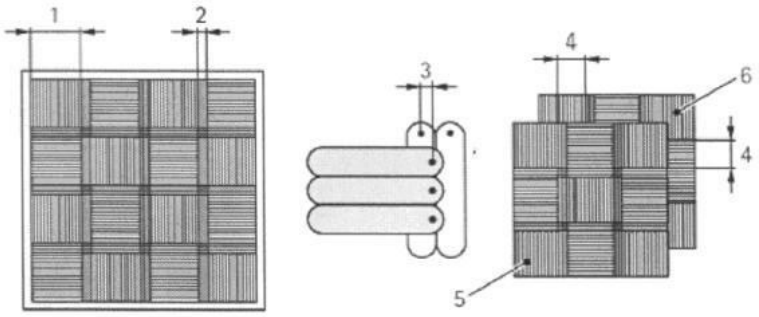

1 Square width
2 Gap width
3 Overlapping
4 Offset
5 1st, 3rd, 5th layer, etc.
6 2nd, 4th, 6th layer, etc.

Figure 59: Exposure type, Squares. (EOS, 2007b)

- Chess: The Chess exposure is different than the Squares exposure, only in the sense that the direction and sequence of the squares' exposure differ. During the Chess exposure, all the squares in one direction are exposed in sequence first, and then the squares in the other direction. Regardless of a displacement of the part, the squares' arrangement is the same at all times (EOS, 2007b).

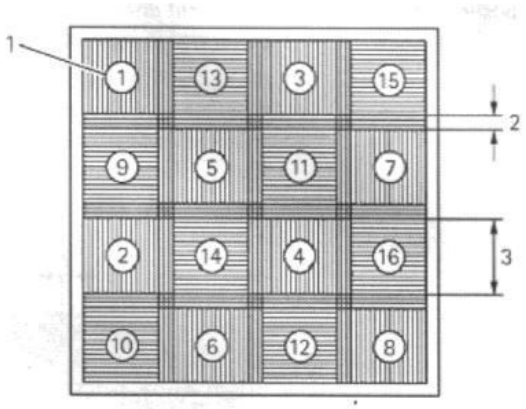

1 Exposure sequence
2 Gap
3 Square

Figure 60: Exposure type, Chess (EOS, 2007b)

APPENDIX B: PARTICLE SIZE DISTRIBUTION

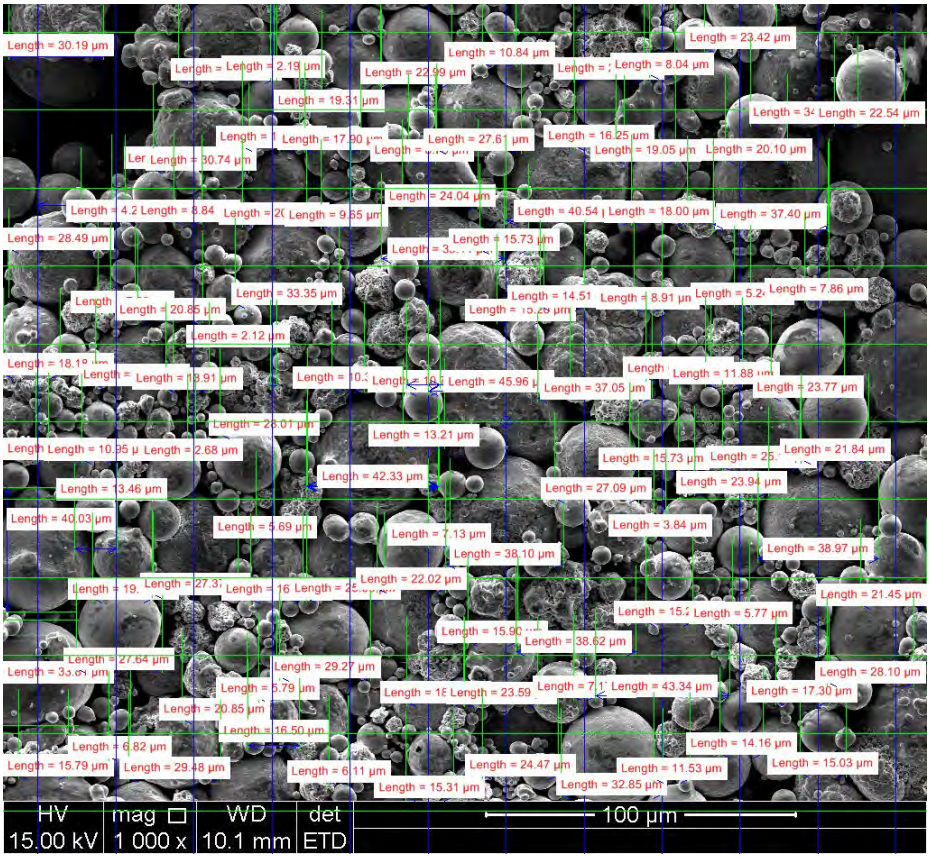

Figure 61: Powder sample with grains as measured to determine the particle size distribution.

Item	Length	Shape
1	30.19	Agglomerate
2	13.89	Spherical
3	28.49	NS[2]
4	18.18	NS
5	3.79	Lenticular
6	40.03	NS
7	33.81	NS
8	15.79	Lenticular
9	4.29	Spherical
10	7.83	Spherical
11	24.76	NS
12	10.95	Spherical
13	19.28	NS
14	27.64	NS
15	6.82	Lenticular
16	30.74	NS
17	30.74	NS
18	8.84	Spherical
19	20.85	NS
20	13.91	Agglomerate
21	2.68	Spherical
22	27.37	NS
23	20.85	Agglomerate
24	29.48	NS
25	2.19	Spherical
26	18.41	Spherical
27	20.36	Spherical
28	33.35	NS
29	2.12	Spherical
30	28.01	Agglomerate
31	5.69	Agglomerate
32	16.85	Lenticular
33	5.79	Spherical
34	16.5	NS
35	19.31	Spherical
36	17.9	Spherical
37	9.65	Spherical
38	10.32	Spherical
39	41.9	NS
40	42.12	NS
41	42.33	NS
42	25.06	NS
43	29.27	NS
44	6.11	Spherical
45	22.99	Spherical
46	8.78	Spherical
47	24.04	Lenticular
48	39.14	NS
49	10.71	Spherical
50	7.46	Agglomerate
51	12.73	Spherical
52	21.94	Spherical
53	17.99	Agglomerate
54	14.63	Spherical
55	10.24	NS
56	27.5	NS
57	19.02	Agglomerate
58	15.07	Agglomerate
59	44.76	NS
60	44.47	NS
61	37.89	NS
62	16.53	Agglomerate
63	23.84	NS
64	21.94	Agglomerate
65	15.62	Spherical
66	39.66	NS
67	13.86	Spherical
68	36.86	Agglomerate
69	26.5	Spherical
70	11.76	Spherical
71	36.15	Agglomerate
72	7.02	Spherical
73	32.47	Spherical
74	8.25	Spherical
75	19.31	Lenticular
76	18.25	Spherical
77	8.95	Spherical
78	5.27	Spherical
79	15.44	NS
80	4.04	Spherical
81	15.62	Spherical
82	42.65	NS
83	11.23	Agglomerate
84	22.99	NS
85	19.83	Spherical
86	37.21	NS
87	5.09	Spherical
88	12.29	Agglomerate
89	24.92	Spherical
90	23.87	Agglomerate
91	5.44	Spherical
92	9.3	Agglomerate
93	13.69	Spherical
94	32.64	NS
95	15.8	Agglomerate
96	37.38	NS
97	7.37	Agglomerate
98	23.34	NS
99	21.06	Spherical
100	38.08	NS
101	10.35	Agglomerate
102	10.35	Agglomerate
103	14.39	Lenticular

Table 13: Grain sizes and shape as measured in Figure 61.

[2] NS denotes Near Spherical

APPENDIX C: SINTERING PARAMETERS OF SINTERED SAMPLES

	Sample 1	Sample 2	Sample 3
NAME	***Solid Skin***	***Skin Stripes***	***Skin Chess***
Speed	300 mm/s	300 mm/s	300 mm/s
Power	228 W	228 W	228 W
Beam offset	0.34 mm	0.34 mm	0.34 mm
Layer Thickness	0.06 mm	0.06 mm	0.06 mm

Table 14: Sintering parameters for the pre-contours of the *Solid Skin, Skin Stripes* and *Skin Chess* geometric sintering strategies

	Sample 1	Sample 2	Sample 3
NAME	***Solid Skin***	***Skin Stripes***	***Skin Chess***
Exposure type	Stripes	Stripes	Stripes
Skin Thickness (x/y)	50 mm	1 mm	1 mm
Skin Thickness (z)	6 mm	0.5 mm	0.5 mm
Skipped layers	0	0	0
Distance between parallel lines	0.2 mm	0.2 mm	0.2 mm
Width	5 mm	5 mm	5 mm
Speed	500 mm/s	500 mm/s	500 mm/s
Overlap	-0.1 mm	-0.1 mm	-0.1 mm
Power	228 W	228 W	228 W
Beam offset[3]	0.365 mm	0.365 mm	0.365 mm
Layer thickness	0.06 mm	0.06 mm	0.06 mm

Table 15: Sintering parameters for the outer skin of the *Solid Skin*, *Skin Stripes* and *Skin Chess* geometric sintering strategies

[3]Offset with reference to boundary. See Figure 18

	Sample 1	Sample 2	Sample 3
NAME	***Solid Skin***	***Skin Stripes***	***Skin Chess***
Exposure type	N.A.	N.A.	Chess
Skin thickness (x/y)			1.5 mm
Skin Thickness (z)			1 mm
Distance between parallel lines			0.25 mm
Gap Distance			0.25 mm
Speed			350 mm/s
Power			228 W
Square width			5 mm
Overlap			0.04 mm
Beam offset			0.025 mm

Table 16: Sintering parameters for the inner skin of the *Solid Skin*, *Skin Stripes* and *Skin Chess* geometric sintering strategies

	Sample 1	Sample 2	Sample 3
NAME	***Solid Skin***	***Skin Stripes***	***Skin Chess***
Exposure type	N.A.	Stripes	Chess
Distance between parallel lines		0.3 mm	0.2 mm
Speed		250 mm/s	875 mm/s
Power		228 W	228 W
Square/Stripe width		60 mm	7 mm
Overlap		-0.1 mm	0.04 mm
Beam offset		0.3 mm	0.025 mm

Table 17: Sintering parameters for the core of the *Solid Skin*, *Skin Stripes* and *Skin Chess* geometric sintering strategies

	Sample 1	Sample 2	Sample 3
NAME	***Solid Skin***	***Skin Stripes***	***Skin Chess***
Speed	500 mm/s	500 mm/s	500 mm/s
Power	228 W	228 W	228 W
Beam offset	0.24 mm	0.24 mm	0.24 mm
Thickness	0.06 mm	0.06 mm	0.06 mm

Table 18: Sintering parameters for the post contour of the *Solid Skin*, *Skin Stripes* and *Skin Chess* geometric sintering strategies

APPENDIX D: GRINDING AND POLISHING SPECIFICATIONS

Step	Grid	Fluid	Rotational speed	Normal Force	Time
1	60	Distilled water	300 rpm	15 N	1 min
2	120	Distilled water	300 rpm	15 N	1 min 20 sec
3	400	Distilled water	300 rpm	15 N	3 min 20 sec
4	800	Distilled water	300 rpm	15 N	3 min
5	1 200	Distilled water	300 rpm	15 N	3 min 30 sec

Table 19: Steps followed during the grinding process of the samples

Step	Cloth	Diamond suspension	Rotational speed	Normal force	Time
1	6 µm	6 µm StruersDiaDuo	150 rpm	25 N	2 min
2	3 µm	3 µm StruersDiaDuo	150 rpm	35 N	4 min
3	1 µm	1 µm StruersDiaDuo	150 rpm	40 N	4 min

Table 20: Steps followed during the polishing process of the samples

APPENDIX E: MICROSCOPE IMAGES AT NINE POSITIONS OF THE SAMPLES

Solid Skin

	OUTSIDE	INTERMEDIATE	CENTER
TOP	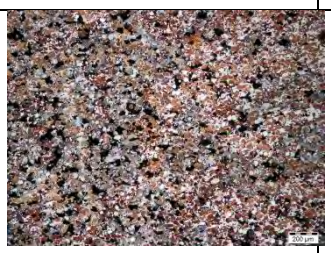		
MIDDLE	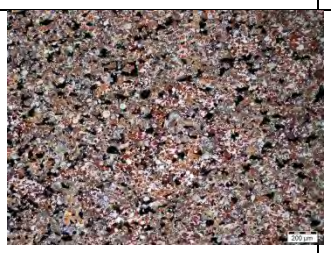		
BOTTOM	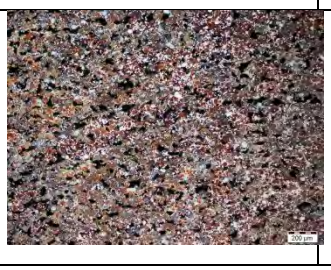		

Figure 62: Optical microscope images of the sample manufactured through the *Solid Skin* geometric sintering strategy at 50x magnification

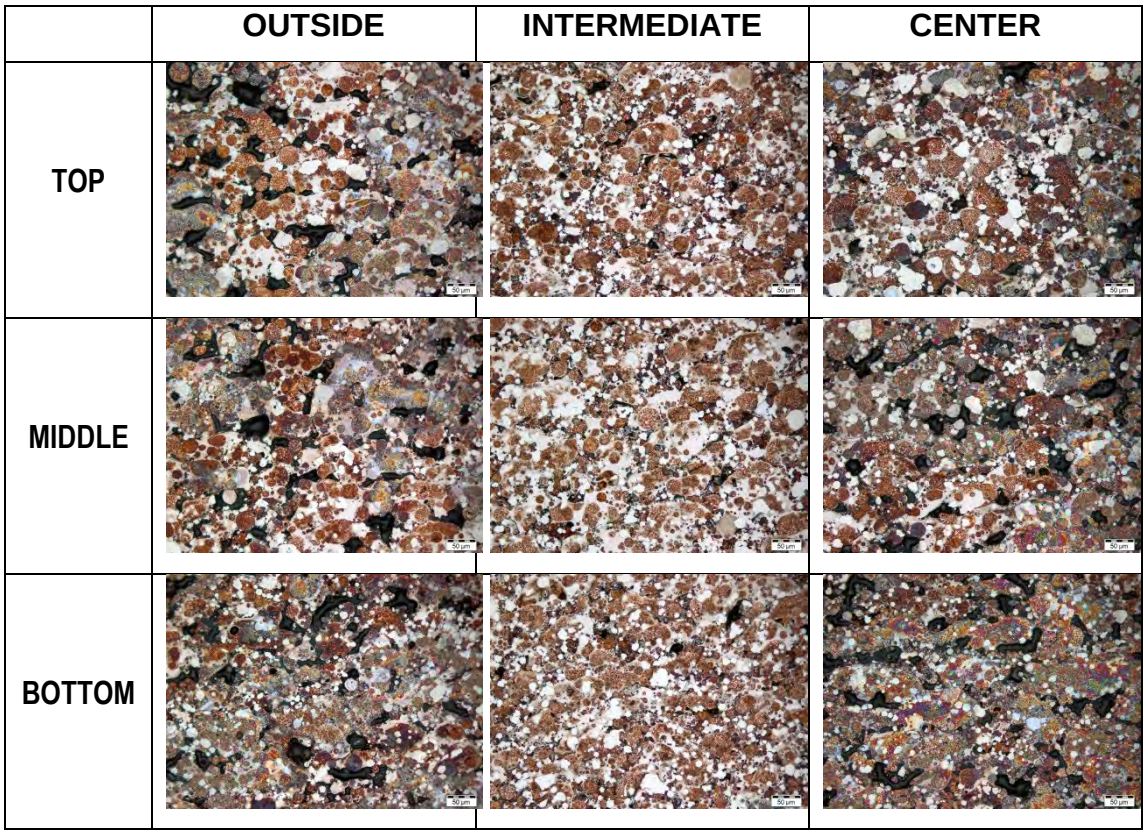

Figure 63: Optical microscope images of the sample manufactured through the *Solid Skin* geometric sintering strategy at 200x magnification

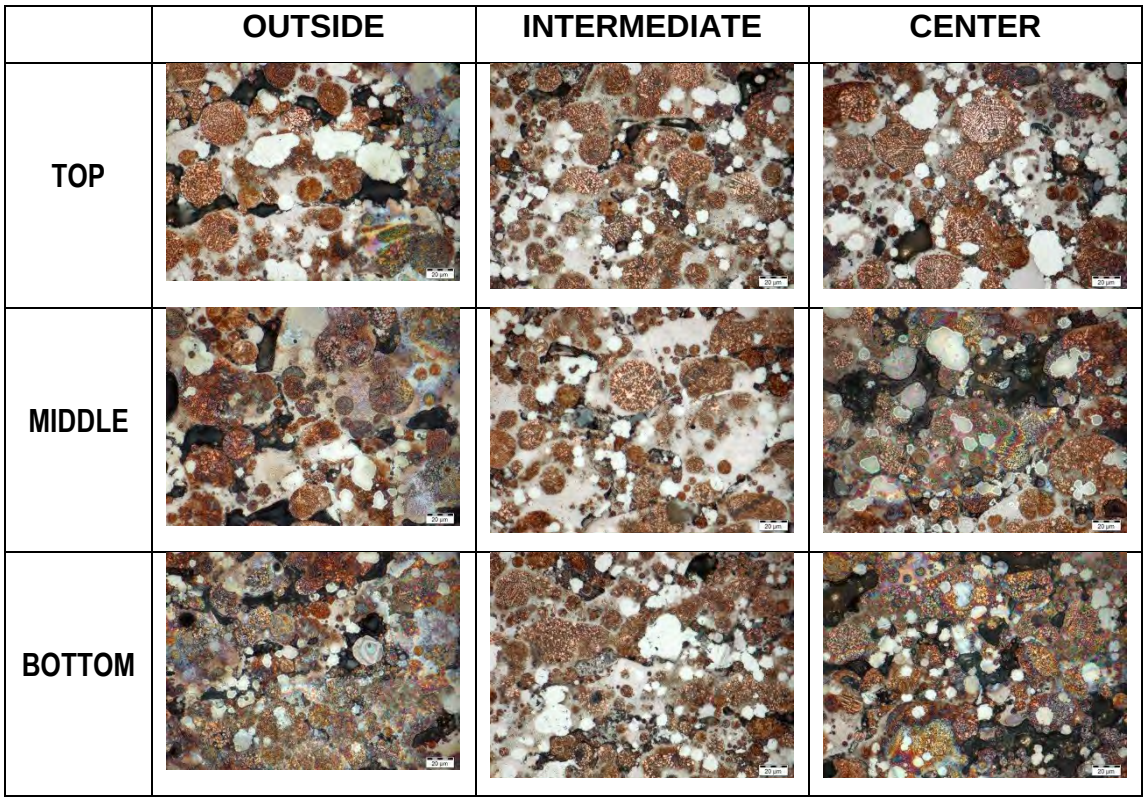

Figure 64: Optical microscope images of the sample manufactured through the *Solid Skin* geometric sintering strategy at 500x magnification

Skin Stripes

	OUTSIDE	INTERMEDIATE	CENTER
TOP			
MIDDLE			
BOTTOM			

Figure 65: Optical microscope images of the sample manufactured through the *Skin Stripes* geometric sintering strategy at 50x magnification

	OUTSIDE	INTERMEDIATE	CENTER
TOP	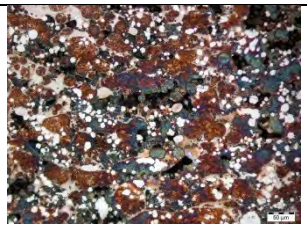	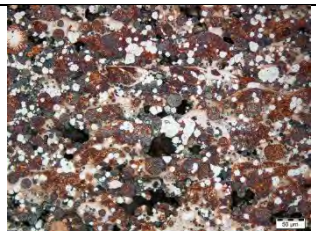	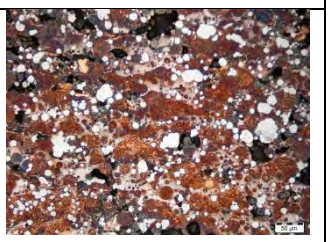
MIDDLE	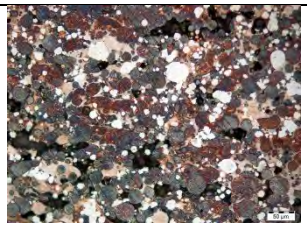	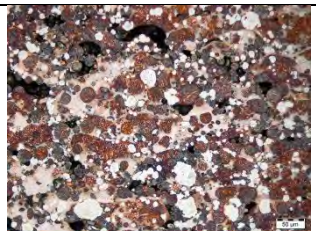	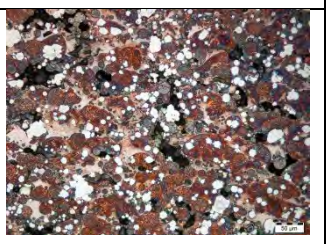
BOTTOM	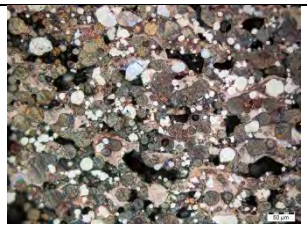	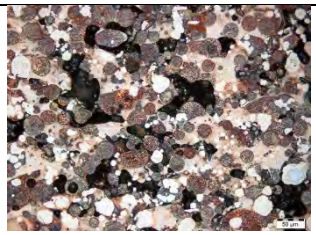	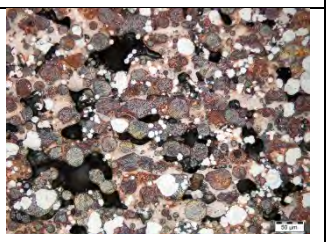

Figure 66: Optical microscope images of the sample manufactured through the *Skin Stripes* geometric sintering strategy at 200x magnification

	OUTSIDE	INTERMEDIATE	CENTER
TOP	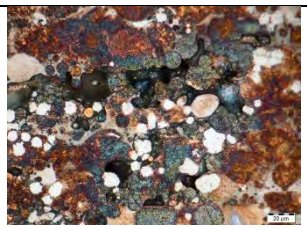	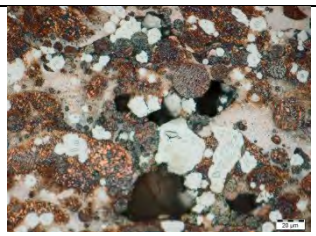	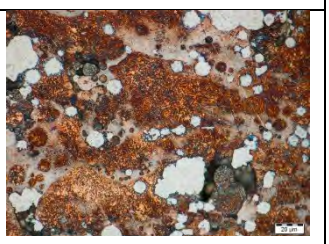
MIDDLE	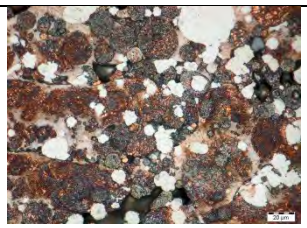	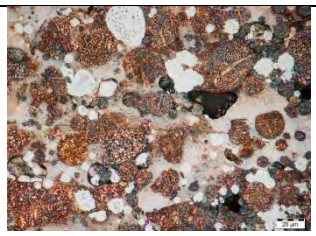	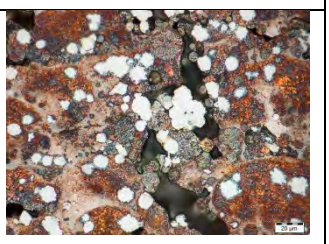
BOTTOM		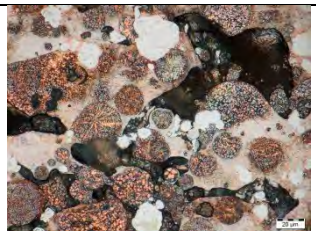	

Figure 67: Optical microscope images of the sample manufactured through the *Skin Stripes* geometric sintering strategy at 500x magnification

A clear void in the form of a crack is present on the outside of the sample, dividing the sample manufactured through the *Skin Stripes* geometric sintering strategy into a denser microstructure of 600 µm – 700 µm and less dense microstructure at the centre. When being very observant, it is evident that a number of voids separate a 600 µm strip at the top from the rest of the sample. In Figure 68 and Figure 69 below, the cracks were measured using NIS Elements D 3.2.

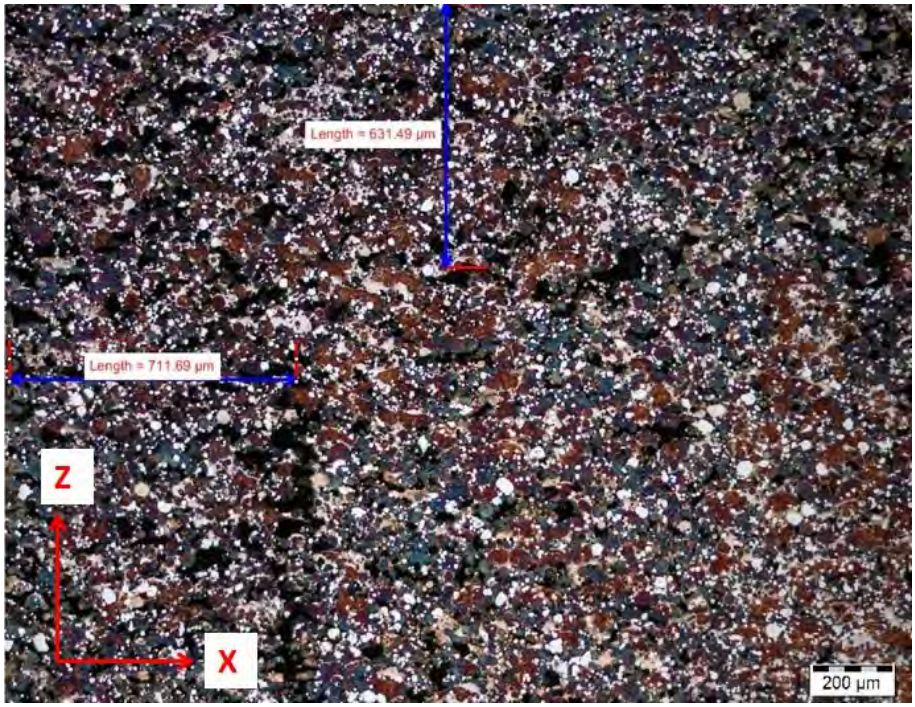

Figure 68: Optical microscope image of the top outside corner of the sample manufactured through the *Skin Stripes* geometric sintering strategy at 50x magnifications

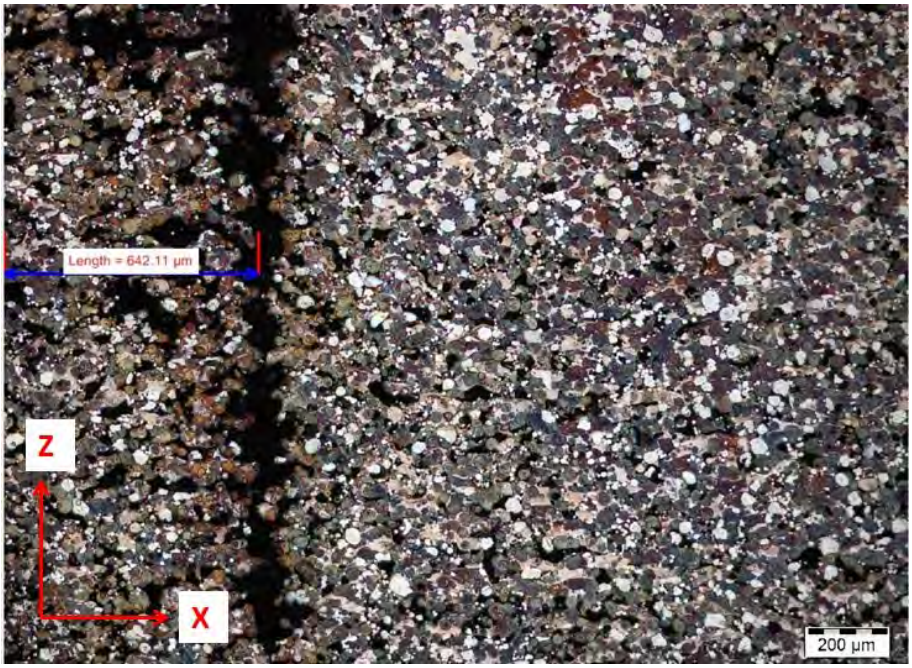

Figure 69: Optical microscope image of the bottom outside corner of the sample manufactured through the *Skin Stripes* geometric sintering strategy at 50x magnification

Skin Chess

	OUTSIDE	INTERMEDIATE	CENTER
TOP			
MIDDLE	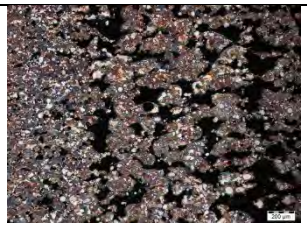		
BOTTOM	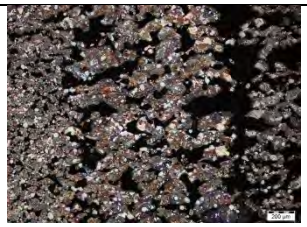		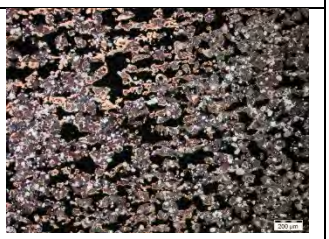

Figure 70: Optical microscope images of the sample manufactured through the *Skin Chess* geometric sintering strategy at 50x magnification

	OUTSIDE	INTERMEDIATE	CENTER
TOP	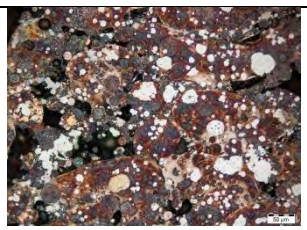	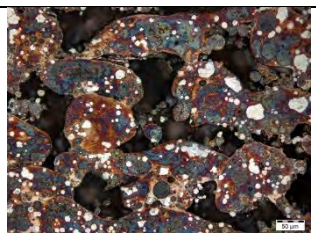	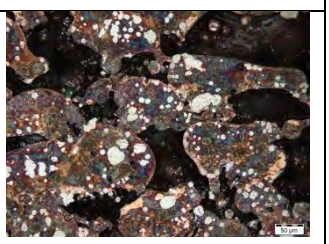
MIDDLE	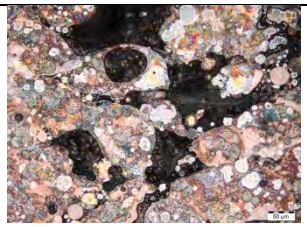	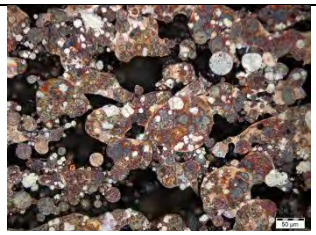	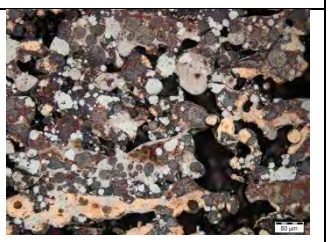
BOTTOM	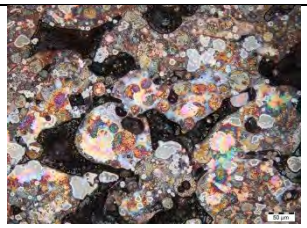	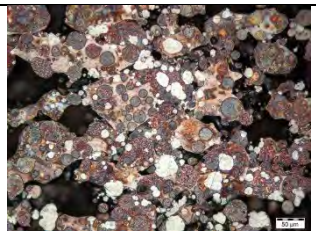	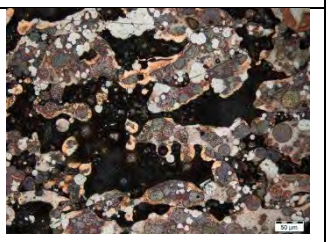

Figure 71**:** Optical microscope images of the sample manufactured through the *Skin Chess* geometric sintering strategy at 200x magnification

	OUTSIDE	INTERMEDIATE	CENTER
TOP	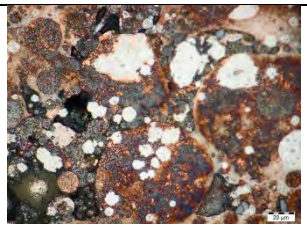	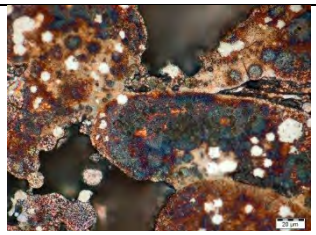	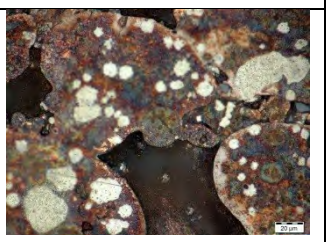
MIDDLE	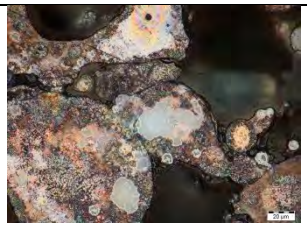	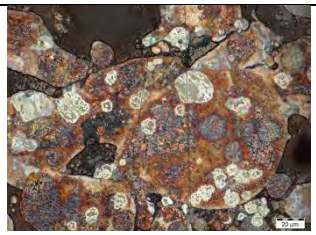	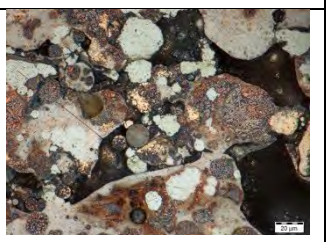
BOTTOM	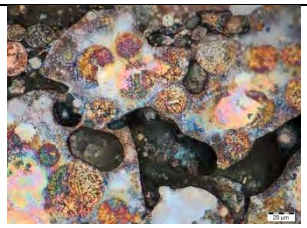	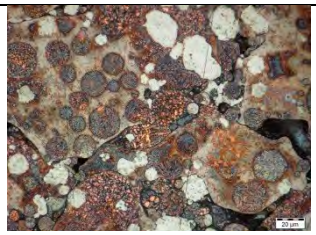	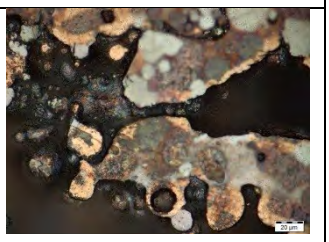

Figure 72: Optical microscope images of the sample manufactured through the *Skin Chess* geometric sintering strategy at 500x magnification

At 50x magnification a denser microstructure is visible in the sample manufactured through the *Skin Chess* geometric sintering strategy for ‘n strip of ~500 µm at the top of the sample and to the outside of the sample. A clear cavity in the form of a crack separates the dense section from the less compact microstructure. When investigating the outside portion of the sample even further, a second crack is identified on the inside of the less-dense section; this forms a boundary to the less-dense section which has a width of ~1 500 µm. In Figure 73 below it is indicated how and where the cavities are measured.

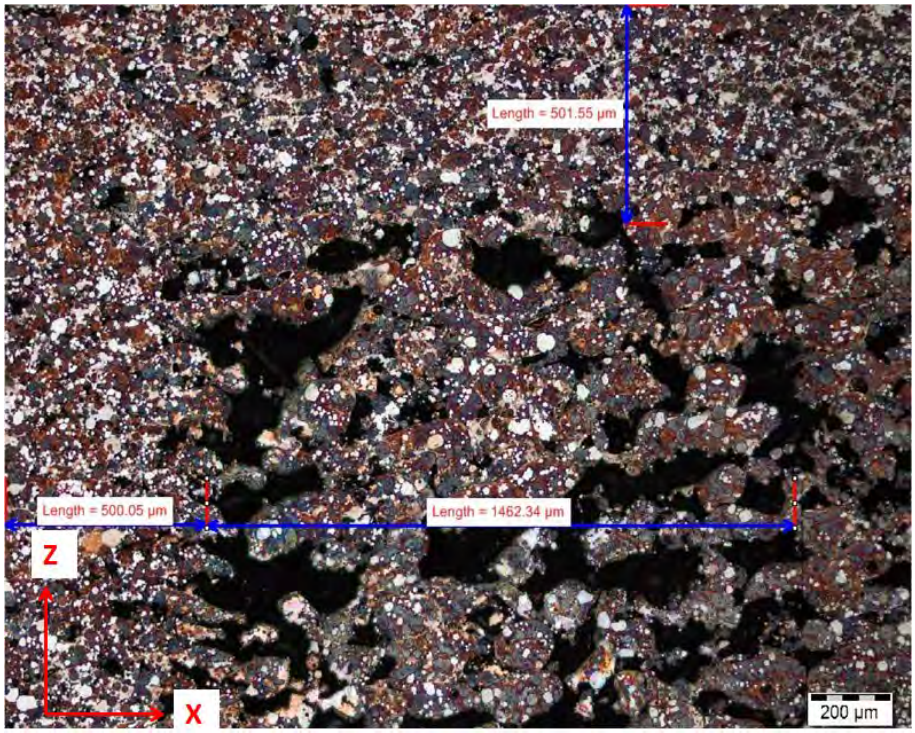

Figure 73: Optical microscope image of the top outside corner of the sample manufactured through the *Skin Chess* geometric sintering strategy at 50x magnification

APPENDIX F: IDENTIFICATION OF PHASES IN THE SINTERED SAMPLES

Solid Skin

	Outside
Light microscope 100x magnification	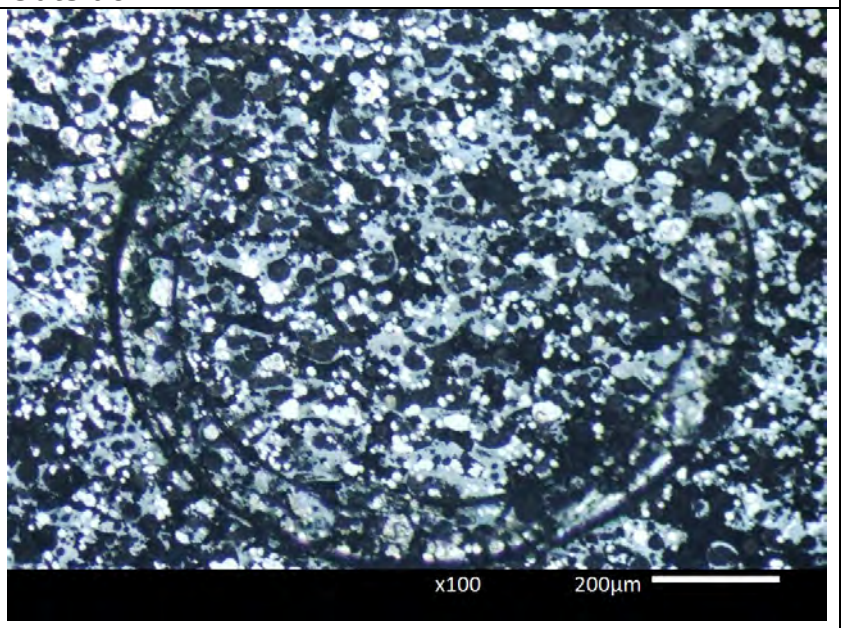
Light microscope 400x magnification	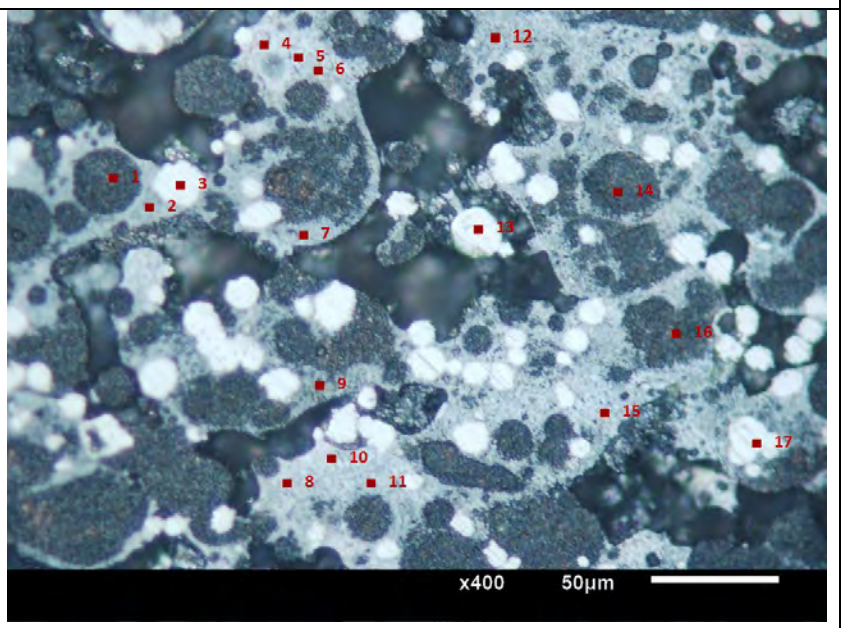

Electron Microscope 400x magnification

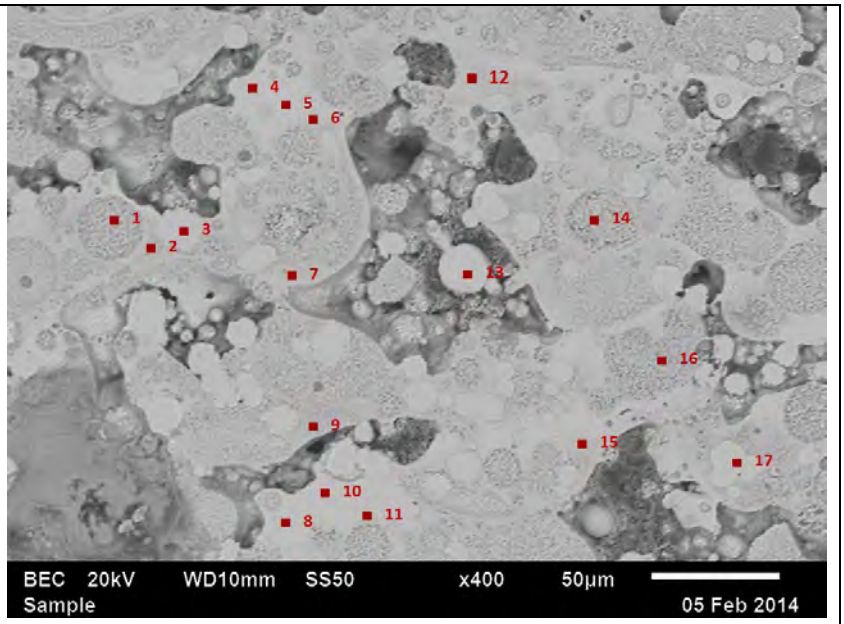

SEM EDS Analyses Results: Normalized weight %

	wt% Cu	wt% P	wt% Ni	wt% Sn
1	88.9	0.8	0.8	9.5
2	90.0	5.3	2.1	2.7
3	4.1	0.1	95.8	0.0
4	92.4	6.0	1.2	0.5
5	94.6	4.6	0.3	0.5
6	95.6	3.8	0.1	0.5
7	67.4	2.8	27.8	1.9
8	94.0	3.4	2.2	0.4
9	90.5	3.2	1.8	4.4
10	94.4	4.6	0.8	0.2
11	92.4	5.3	0.6	1.7
12	93.7	3.0	0.5	2.8
13	3.5	0.0	96.4	0.2
14	86.3	1.0	0.8	11.9
15	93.7	4.7	0.7	1.0
16	89.4	0.9	1.6	8.2
17	2.8	0.1	97.0	0.2

Figure 74: Images and composition of phases identified in the outside position of the sample manufactured through the *Solid Skin* geometric sintering strategy

	Intermediate
Light microscope 100x magnification	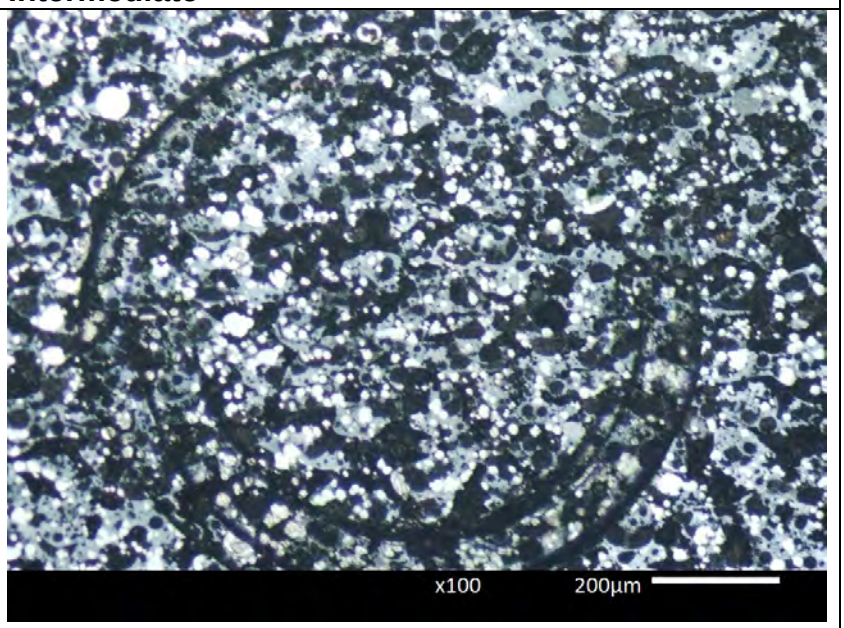
Light microscope 400x magnification	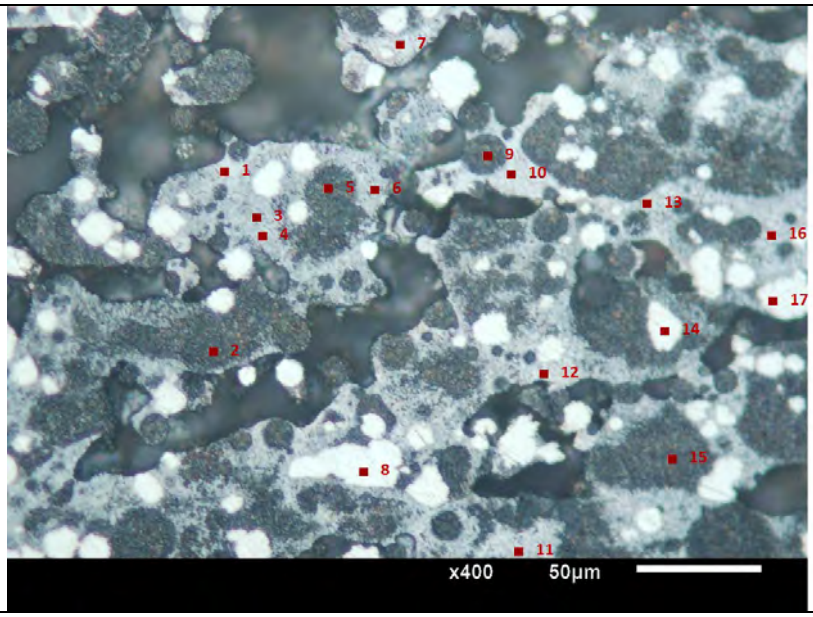

Electron Microscope 400x magnification

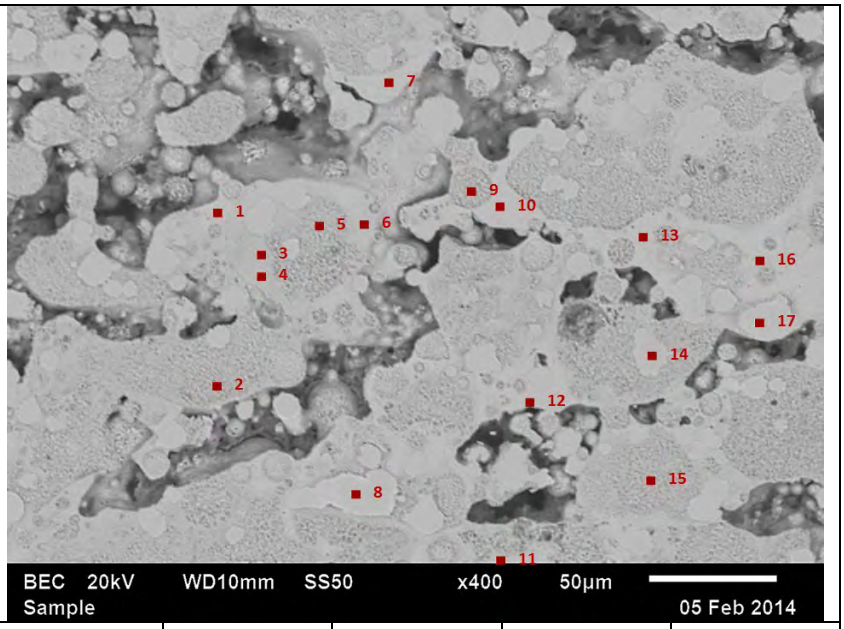

SEM EDS Analyses Results: Normalized weight %

	wt% **Cu**	wt% **P**	wt% **Ni**	wt% **Sn**
1	93.2	5.2	1.2	0.4
2	88.0	1.0	0.5	10.5
3	92.8	4.8	0.9	1.5
4	92.6	4.4	0.9	2.2
5	88.2	0.9	0.5	10.3
6	94.7	3.6	0.5	1.3
7	95.6	3.6	0.5	0.3
8	2.9	0.1	97.1	0.0
9	88.3	1.0	0.5	10.2
10	94.5	4.6	0.8	0.1
11	94.9	4.2	0.6	0.4
12	95.0	3.7	1.0	0.4
13	96.2	3.0	0.5	0.3
14	4.2	0.0	95.6	0.2
15	87.3	0.6	0.7	11.5
16	94.4	3.4	0.7	1.6
17	2.8	0.1	97.1	0.0

Figure 75: Images and composition of phases identified in the intermediate position of the sample manufactured through the *Solid Skin* geometric sintering strategy

	Centre
Light microscope 100x magnification	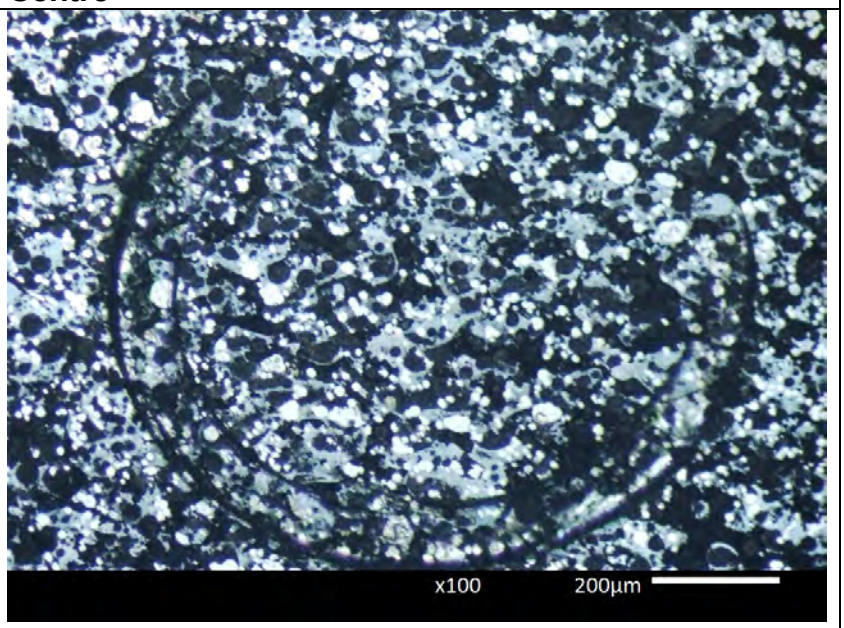
Light microscope 400x magnification	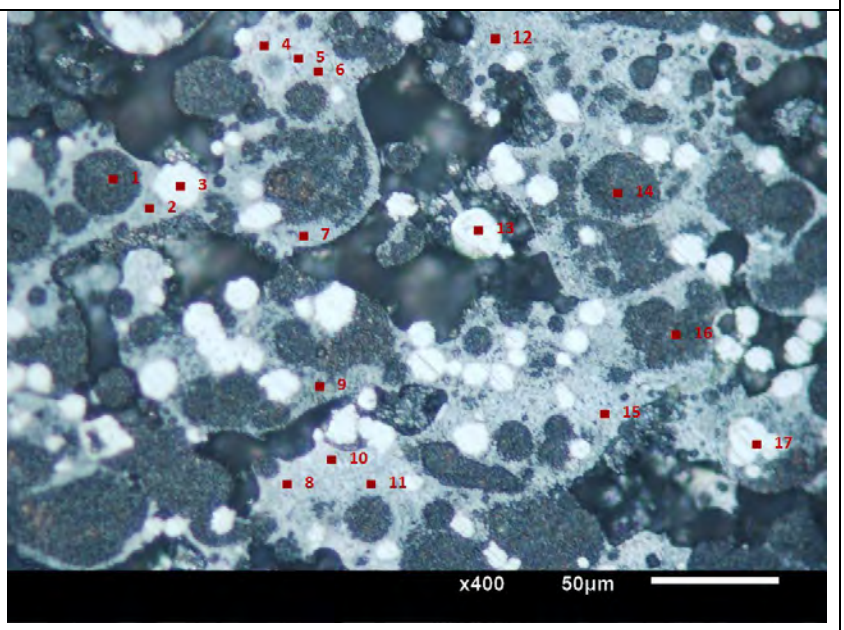

Electron Microscope 400x magnification

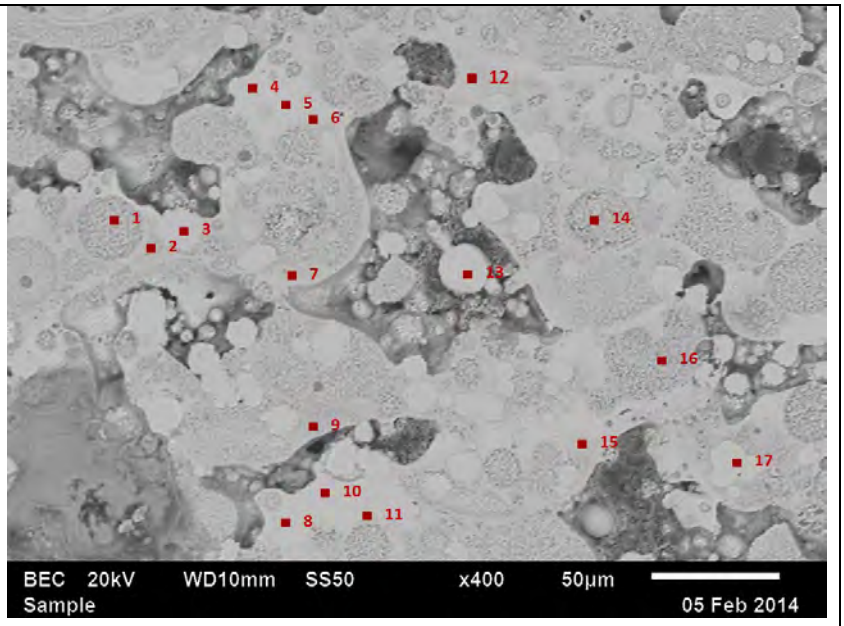

SEM EDS Analyses Results: Normalized weight %

	wt% **Cu**	wt% **P**	wt% **Ni**	wt% **Sn**
1	90.6	0.6	0.2	8.6
2	95.6	2.1	1.8	0.5
3	86.9	1.0	0.8	11.4
4	91.7	4.7	2.1	1.5
5	90.3	1.3	0.5	7.9
6	93.7	5.4	0.5	0.4
7	88.5	1.1	0.5	9.9
8	95.1	3.9	0.4	0.7
9	94.5	4.2	0.5	0.8
10	88.1	1.0	0.6	10.4
11	95.0	4.3	0.4	0.3
12	2.4	0.0	97.5	0.2
13	95.7	2.5	1.0	0.8
14	92.3	4.4	1.9	1.4
15	89.5	0.9	0.5	9.1
16	5.0	0.0	94.8	0.2
17	92.6	5.1	0.6	1.7

Figure 76: Images and composition of phases identified in the centre position of the sample manufactured through the *Solid Skin* geometric sintering strategy

Skin Stripes

	Outside
Light microscope 100x magnification	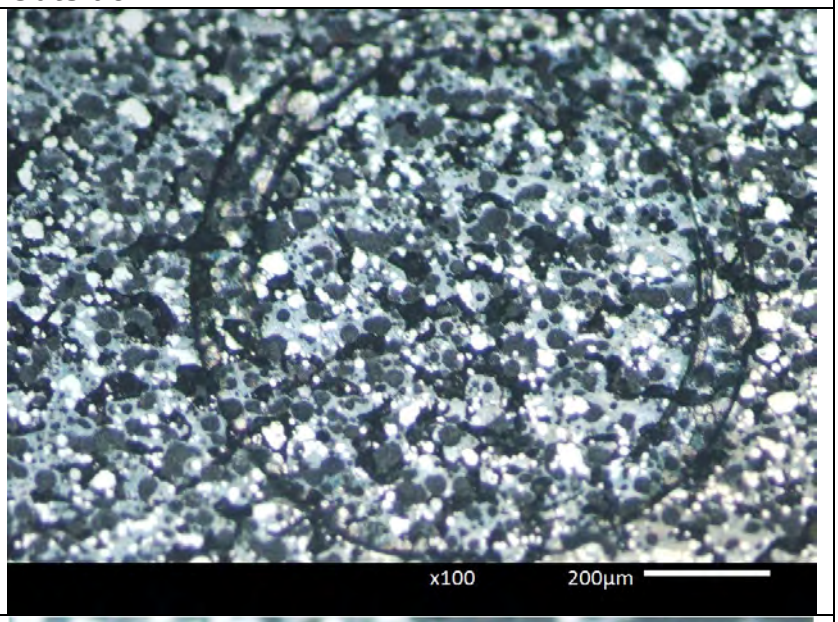
Light microscope 400x magnification	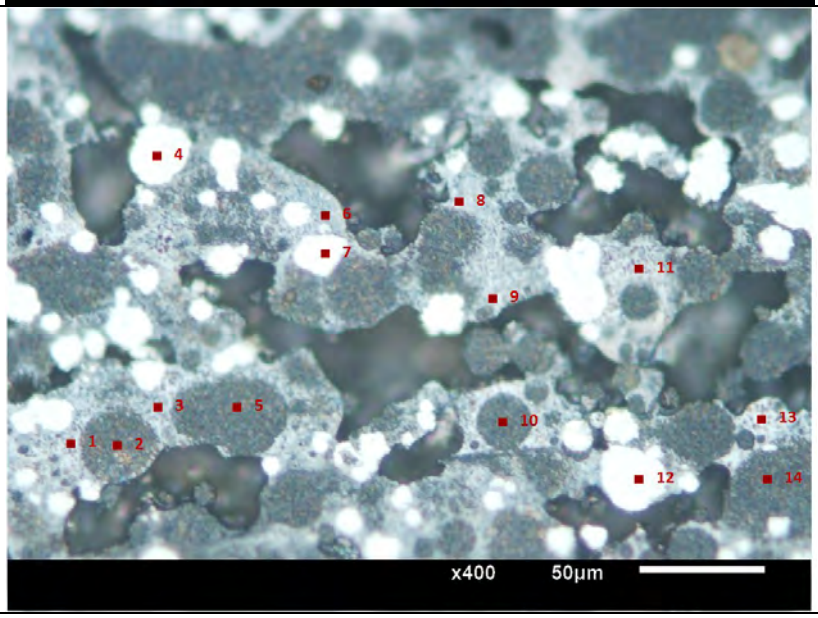

Electron Microscope 400x magnification

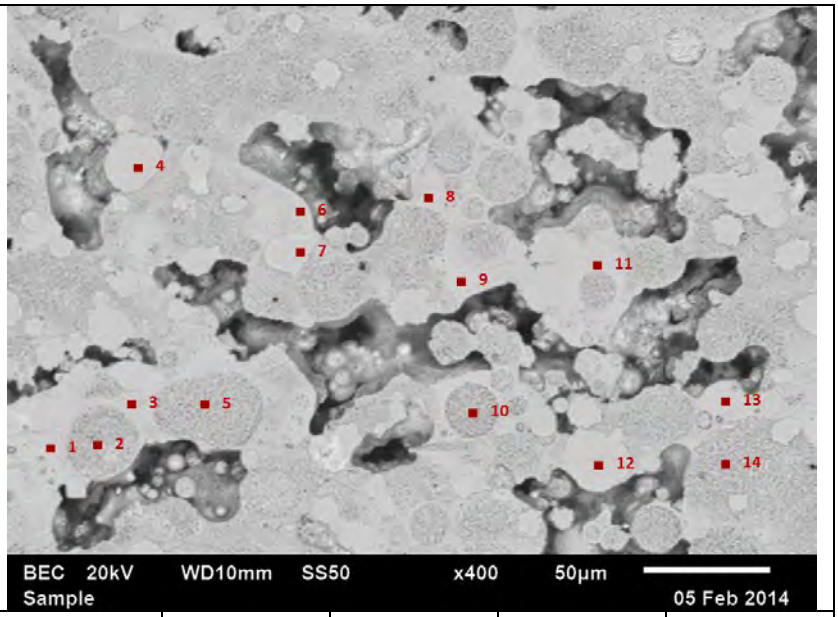

SEM EDS Analyses Results: Normalized weight %

	wt% **Cu**	wt% **P**	wt% **Ni**	wt% **Sn**
1	91.3	4.8	1.4	2.5
2	91.6	0.8	0.6	7.1
3	91.3	3.5	0.7	4.5
4	2.0	0.0	97.8	0.2
5	88.9	1.1	0.5	9.5
6	92.0	4.0	1.2	2.9
7	3.2	0.1	96.6	0.1
8	93.3	4.3	0.4	2.1
9	94.7	3.7	0.7	0.9
10	88.5	0.6	0.7	10.2
11	96.3	2.4	0.5	0.7
12	2.0	0.1	97.9	0.1
13	92.4	5.3	0.6	1.6
14	87.9	1.0	0.5	10.6

Figure 77: Images and composition of phases identified in the outside position of the *sample manufactured through the Skin Stripes* geometric sintering strategy

	Intermediate
Light microscope 100x magnification	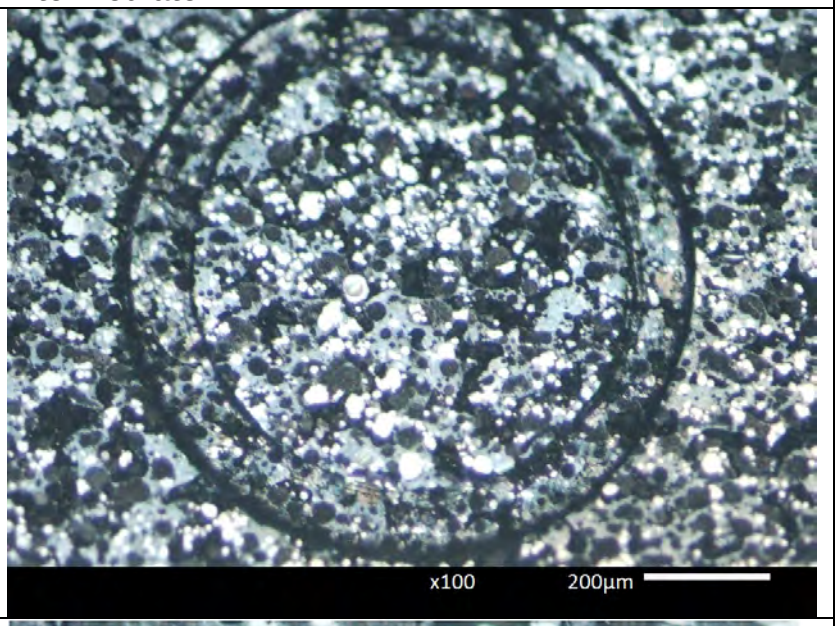
Light microscope 400x magnification	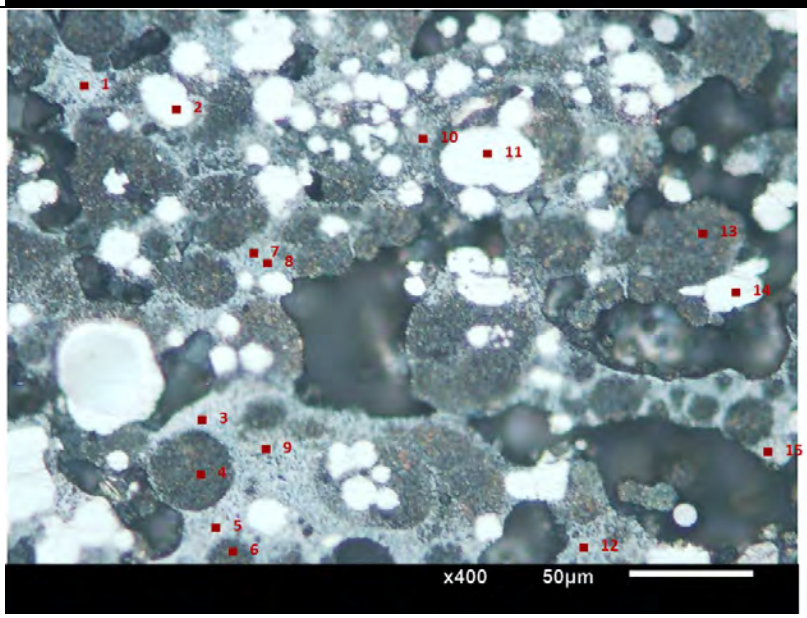

Electron Microscope 400x magnification

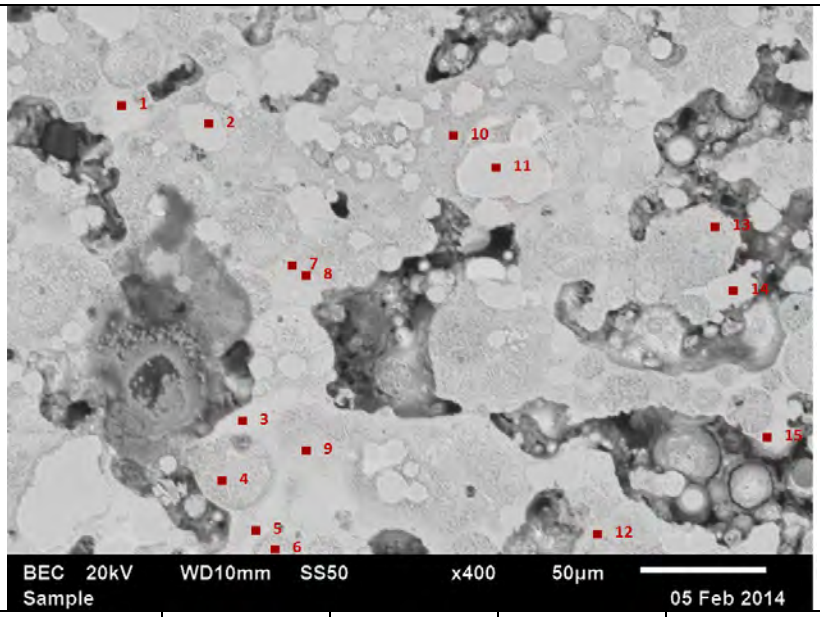

SEM EDS Analyses Results: Normalized weight %

	wt% **Cu**	wt% **P**	wt% **Ni**	wt% **Sn**
1	93.7	5.5	0.5	0.3
2	2.6	0.1	97.3	0.1
3	94.1	4.1	0.6	1.1
4	87.2	0.8	1.7	10.4
5	90.4	6.7	1.0	1.9
6	88.5	0.6	0.4	10.6
7	92.5	2.8	1.5	3.3
8	89.9	3.3	1.8	5.0
9	92.3	5.1	0.7	1.8
10	90.9	4.6	2.1	2.4
11	0.9	0.0	99.1	0.0
12	91.9	3.7	0.3	4.0
13	89.5	0.4	0.8	9.3
14	2.3	0.1	97.4	0.3
15	92.7	4.0	0.9	2.5

Figure 78: Images and composition of phases identified in the intermediate position of the sample manufactured through the *Skin Stripes* geometric sintering strategy

	Centre
Light microscope 100x magnification	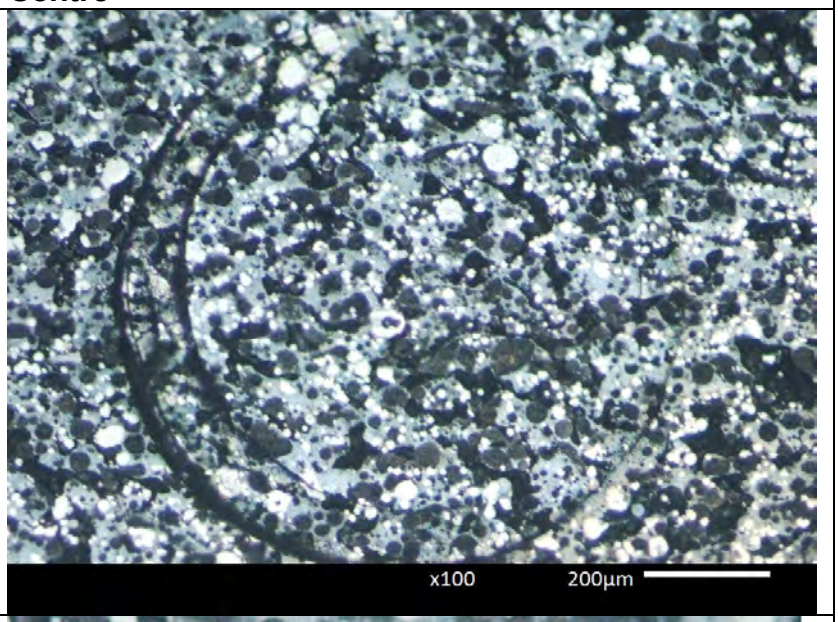
Light microscope 400x magnification	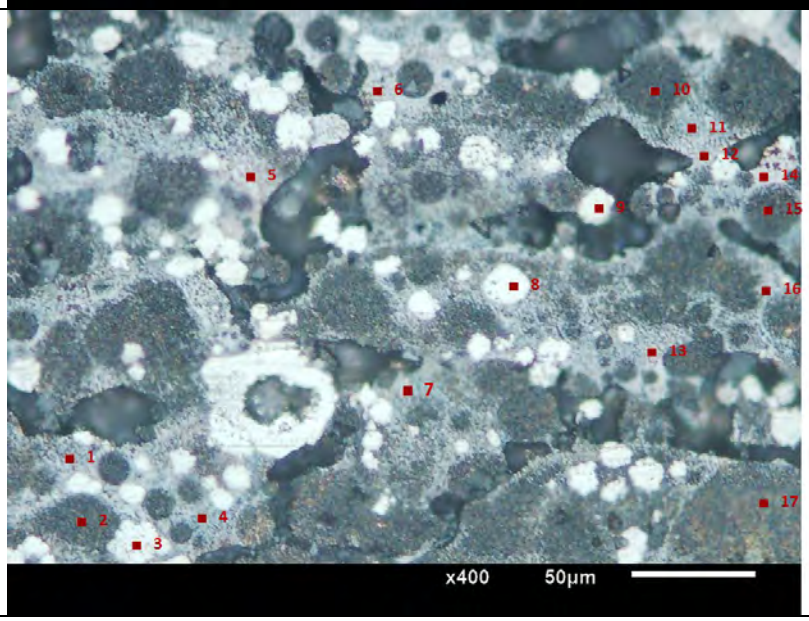

Electron Microscope 400x magnification

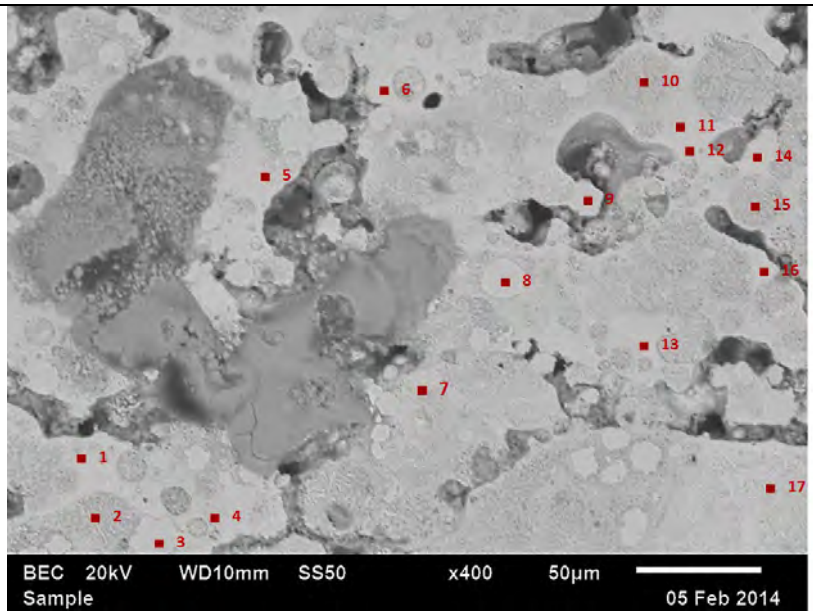

SEM EDS Analyses Results: Normalized weight %

	wt% **Cu**	wt% **P**	wt% **Ni**	wt% **Sn**
1	92.8	4.4	2.0	0.8
2	87.9	1.1	1.0	10.0
3	2.4	0.0	97.5	0.2
4	90.4	3.8	3.0	2.8
5	96.4	2.7	0.5	0.4
6	91.1	5.9	1.5	1.6
7	94.6	0.8	1.0	3.7
8	3.1	0.0	96.9	0.0
9	4.9	0.1	94.8	0.2
10	86.9	1.3	0.8	11.0
11	91.7	4.2	0.9	3.2
12	91.6	4.3	0.8	3.3
13	95.4	2.9	0.7	1.0
14	92.7	4.5	2.1	0.7
15	89.2	0.7	0.5	9.7
16	93.0	4.0	0.5	2.6
17	87.9	0.9	1.0	10.2

Figure 79: Images and composition of phases identified in the centre position of the sample manufactured through the *Skin Stripes* geometric sintering strategy

Skin Chess

	Outside
Light microscope 100x magnification	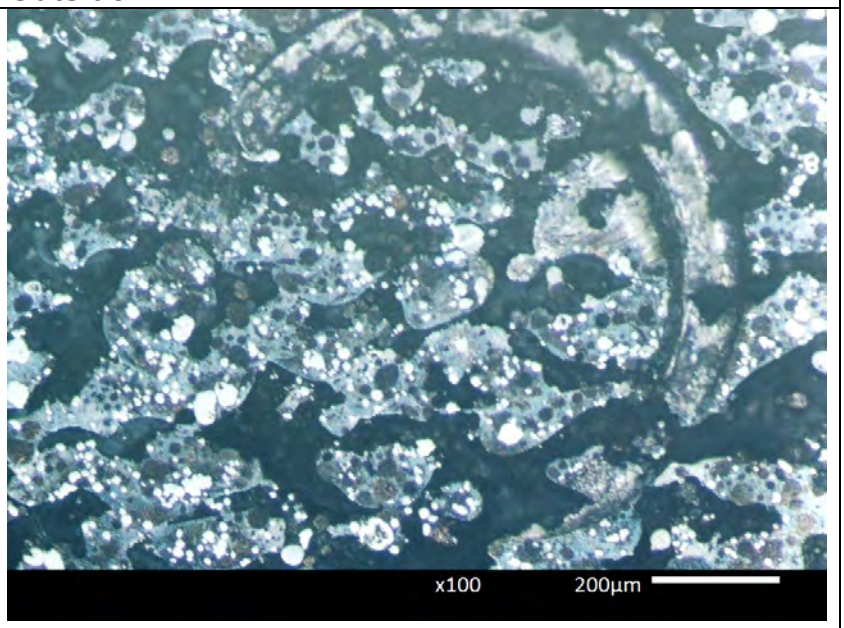
Light microscope 400x magnification	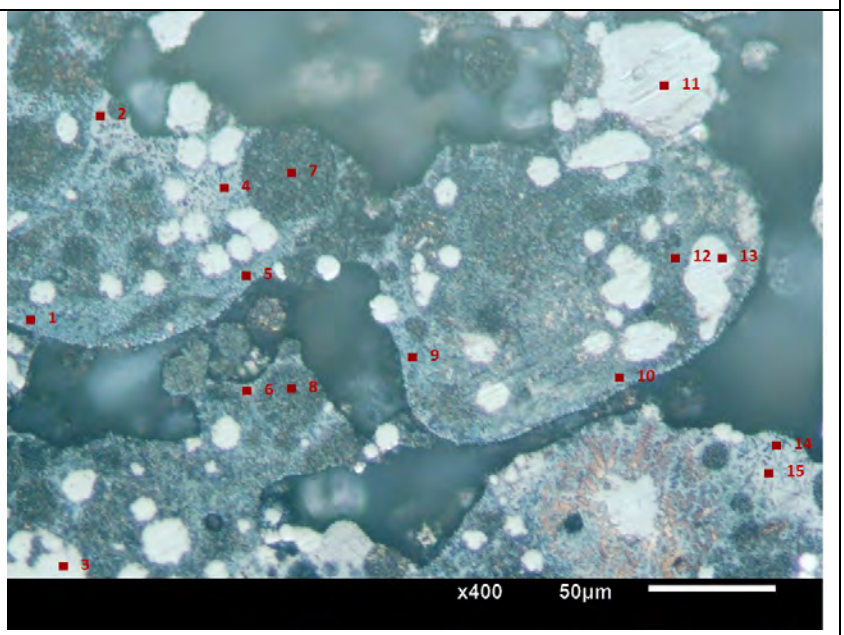

Electron Microscope 400x magnification

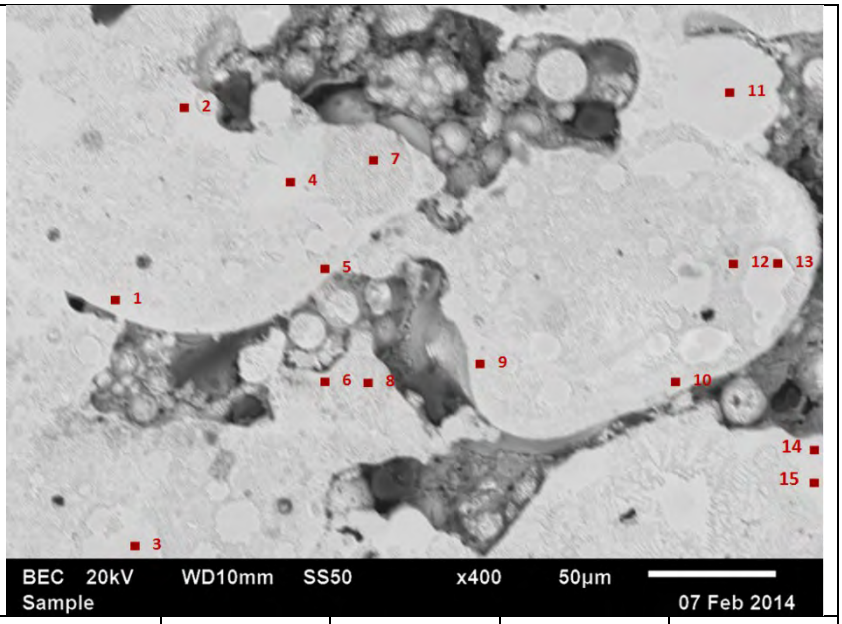

SEM EDS Analyses Results: Normalized weight %

	wt% **Cu**	wt% **P**	wt% **Ni**	wt% **Sn**
1	91.3	2.4	1.3	5.1
2	92.3	5.1	1.1	1.5
3	0.8	0.1	99.0	0.2
4	92.8	4.7	0.7	1.8
5	93.0	1.8	1.3	3.9
6	94.0	3.1	0.6	2.3
7	88.6	0.7	0.6	10.2
8	86.7	1.1	0.4	11.8
9	88.9	3.7	2.7	4.7
10	88.0	1.5	0.9	9.6
11	0.3	0.0	99.7	0.0
12	88.9	3.5	2.4	5.3
13	1.7	0.1	97.9	0.3
14	97.4	1.6	0.3	0.7
15	92.3	7.1	0.1	0.5

Figure 80: Images and composition of phases identified in the outside position of the sample manufactured through the *Skin Chess* geometric sintering strategy

	Intermediate
Light microscope 100x magnification	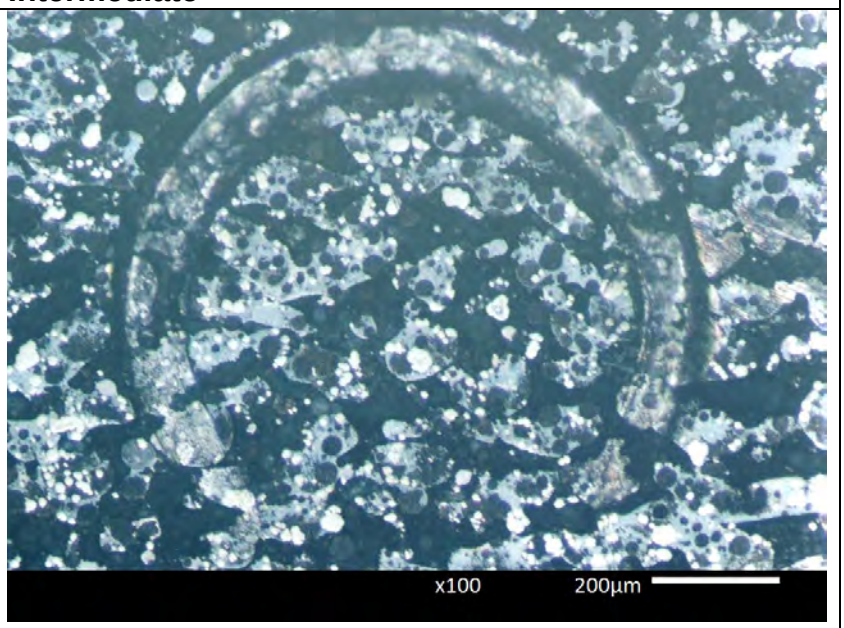
Light microscope 400x magnification	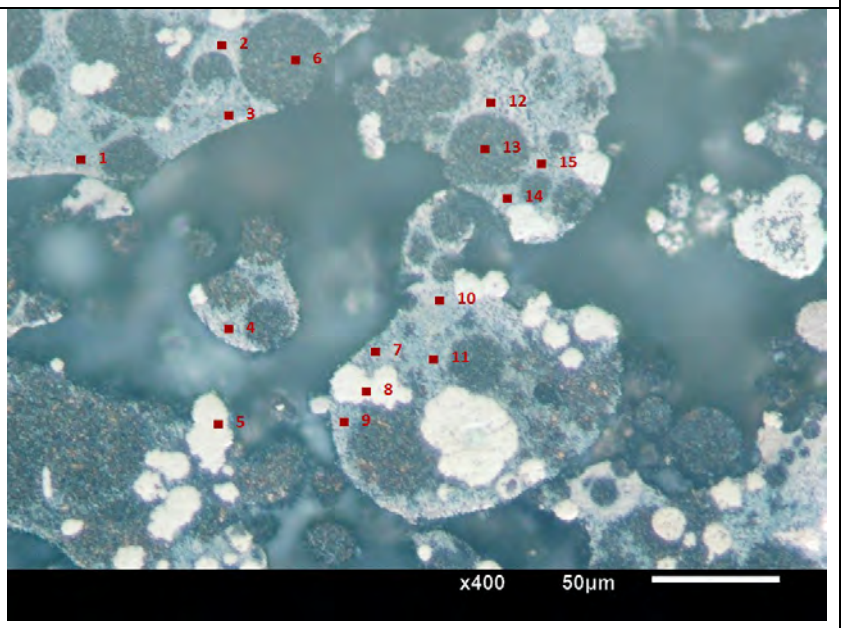

Electron Microscope 400x magnification

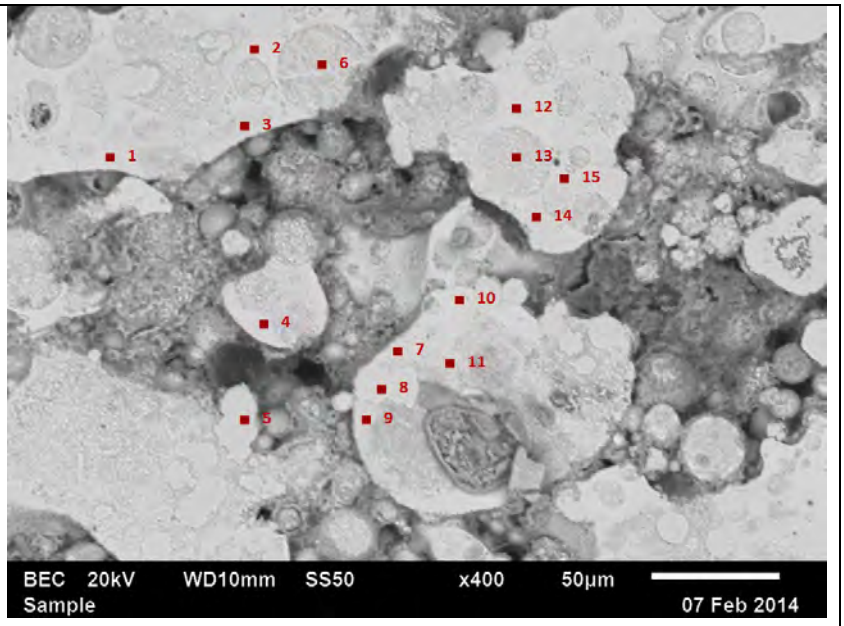

SEM EDS Analyses Results: Normalized weight %

	wt% **Cu**	wt% **P**	wt% **Ni**	wt% **Sn**
1	90.9	4.3	1.4	3.4
2	93.7	3.6	1.3	1.4
3	91.6	4.3	1.2	2.9
4	92.7	5.0	0.9	1.5
5	2.0	0.0	97.8	0.1
6	87.5	0.8	1.6	10.1
7	90.9	5.2	1.5	2.4
8	1.4	0.0	98.4	0.2
9	91.8	2.8	2.3	3.1
1	92.1	5.2	0.8	1.8
10	90.1	4.5	2.7	2.7
11	94.4	4.5	0.6	0.6
12	87.1	1.0	0.9	11.1
13	89.5	5.0	1.5	4.0
14	93.7	3.9	0.7	1.7
15	90.9	4.3	1.4	3.4

Figure 81: Images and composition of phases identified in the intermediate position of the Sample manufactured through the *Skin Chess* geometric sintering strategy

	Centre
Light microscope 100x magnification	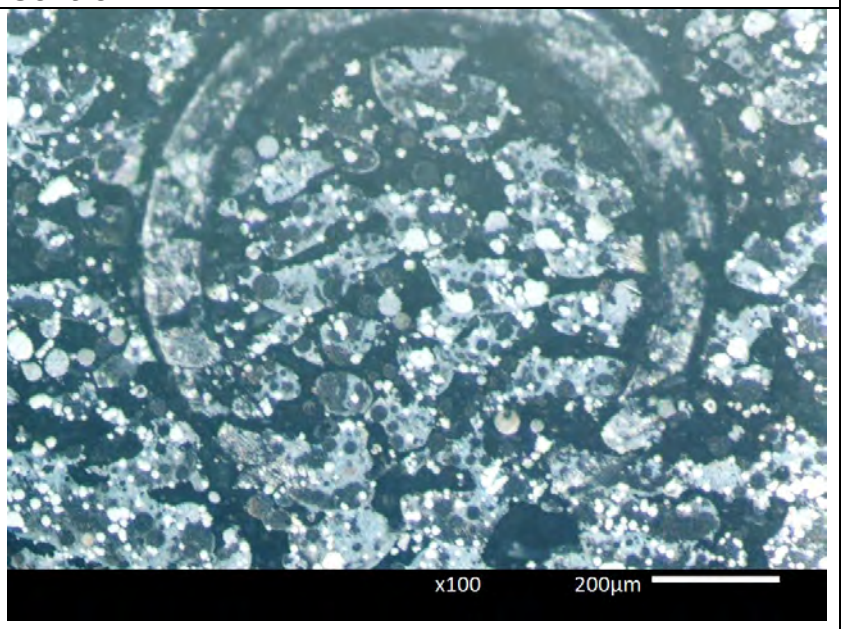
Light microscope 400x magnification	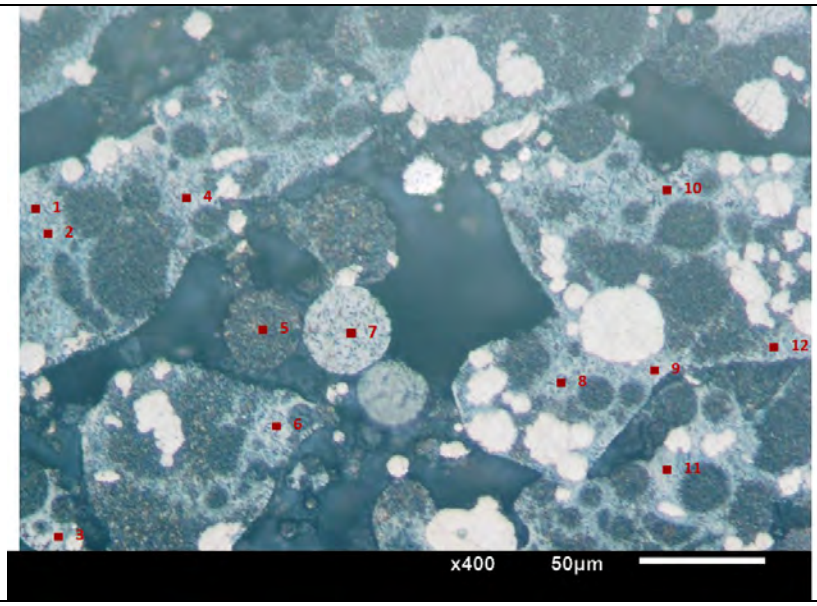

Electron Microscope 400x magnification

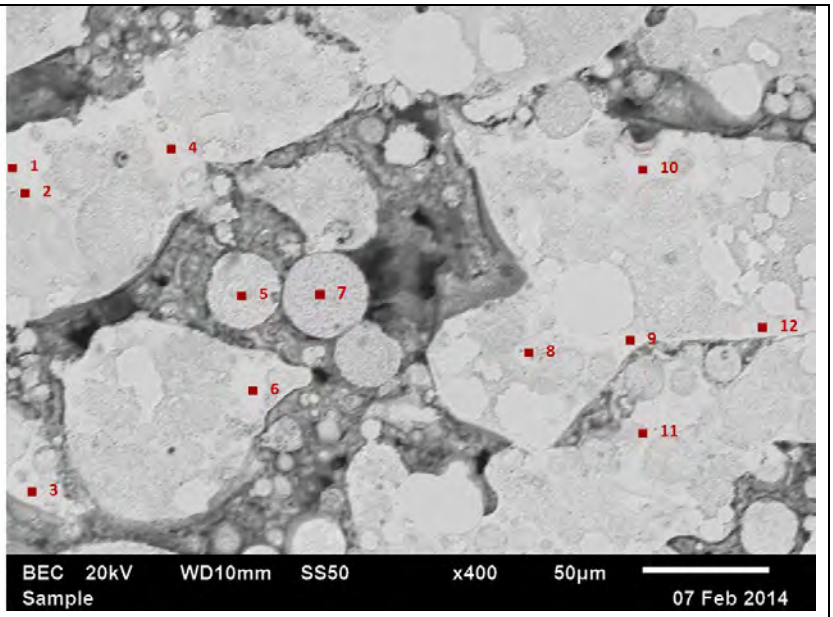

SEM EDS Analyses Results: Normalized weight %

	wt% **Cu**	wt% **P**	wt% **Ni**	wt% **Sn**
1	94.5	5.0	0.4	0.2
2	91.8	6.4	0.4	1.5
3	95.2	2.9	0.7	1.2
4	94.8	3.4	0.3	1.5
5	86.8	0.7	0.8	11.8
6	86.0	4.2	9.4	0.4
7	90.5	8.8	0.2	0.5
8	90.8	6.0	0.7	2.6
9	91.1	6.3	1.2	1.4
10	93.6	4.6	0.3	1.5
11	88.4	6.7	1.5	3.5
12	91.6	4.7	1.3	2.5

Figure 82: Images and composition of phases identified in the centre position of the Sample manufactured through the *Skin Chess* geometric sintering strategy

APPENDIX G: DIMENSIONAL DEFORMATION

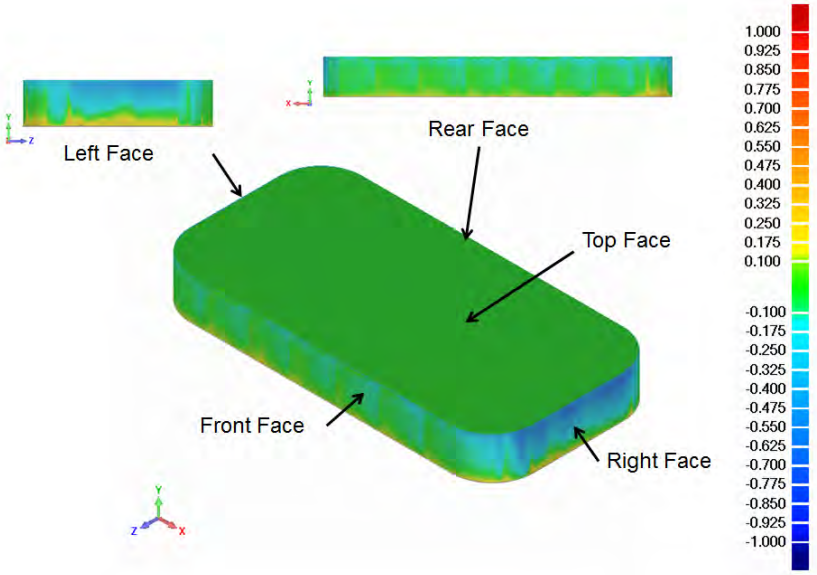

Figure 83: Variation in dimension on the different faces of the sample manufactured through the *Solid Skin* geometric sintering strategy while still attached to the base plate

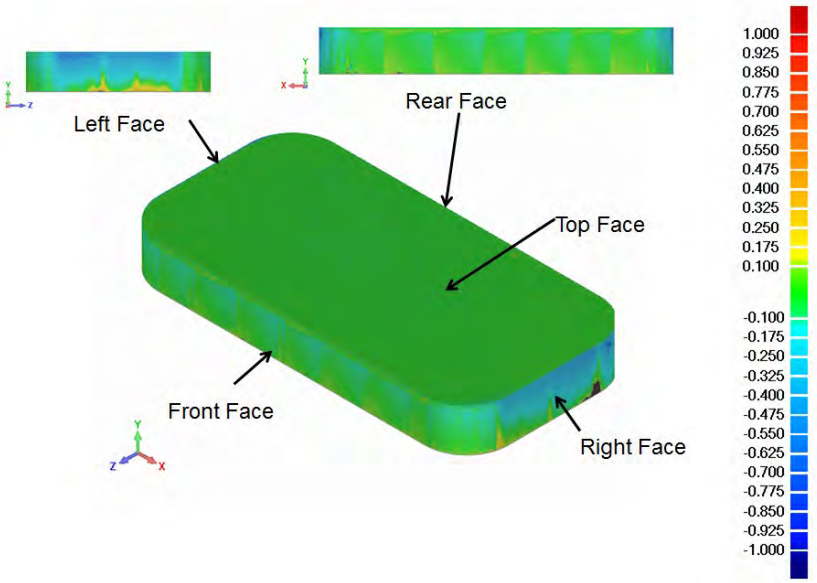

Figure 84: Variation in dimension on the different faces of the sample manufactured through the *Skin Stripes* geometric sintering strategy while still attached to the base plate

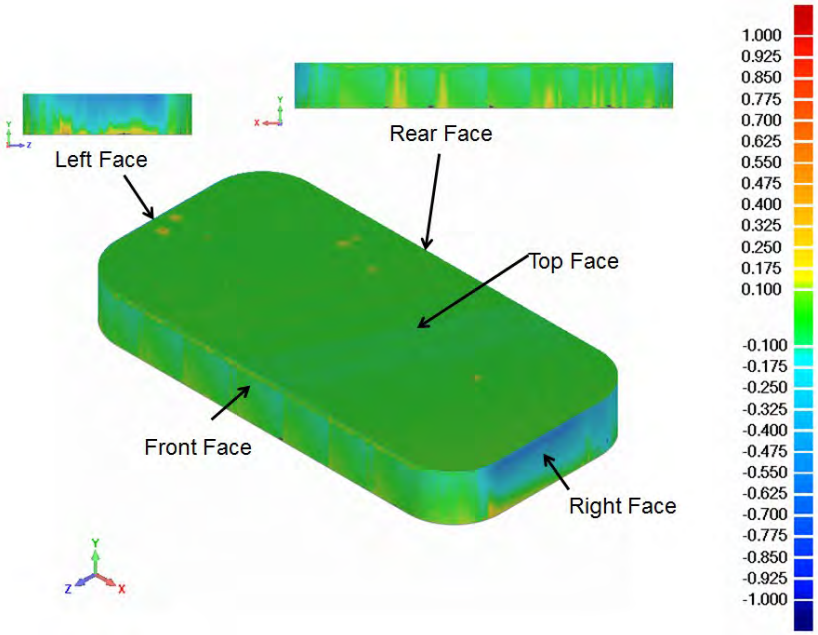

Figure 85: Variation in dimension on the different faces of the sample manufactured through the *Skin chess* geometric sintering strategy while still attached to the base plate

APPENDIX H: MACHINE AND MATERIAL SUPPLIER DATA

General Process Data

EOS (2004) recommends standard parameters for the sintering of *DM 20* for which they state that the mechanical properties will be fairly uniform in all directions. Table 21 below summarizes the recommend layer thickness, some restrictions and the typical achievable accuracy when applying these parameters and restrictions to *DM 20* as recommended.

Minimum recommended layer thickness	20 µm
Typical achievable part accuracy	± 50 µm
Accuracy specification for qualification	±(0.07% + 50) µm
Min. wall thickness	0.6 mm
Volume rate in mm^3/s:	
20 µm layer thickness	
- Skin: 20 µm layers	2 - 8
- Core: 60 µm layers	15
40 µm layer thickness	
- Skin: 40 µm layers	4 - 10
- Core: 80 µm layers	16
20 µm layer thickness	
- Skin: 60 µm layers	6 - 12
- Core: 60 µm layers	18

Table 21: General process data for DirectMetal 20 (EOS, 2004)

Direct Metal 20 Composition

The composition of *Direct Metal 20* can vary between different concentrations of the various ingredients in the powder, and can be seen in Table 22. The powder density is between 4.3 and 5.3 g/cm^3 (EOS, 2012).

Name of ingredient	Chemical Formula	Concentration (%)
Copper	Cu	70 - 90
Phosphorous	P	1 - 5
Tin	Sn	5 - 10
Nickel	Ni	10 - 30

Table 22: Composition of Direct Metal 20 powder (EOS, 2012)

Properties of the Laser Sintered Parts

For the standard parameters (20 µm layer thickness) specified in Table 21, the mechanical and thermal properties of the sintered parts are specified. These can be seen in the sections below and are applicable to the outer skin areas except where stated otherwise.

- **Mechanical Properties**

Density in skin areas	7.6 g/cm^3
Density in core areas	6.3 g/ cm^3
Minimum remaining porosity	8 %
Tensile strength	≤ 400 MPa
Yield strength	200 MPa
Young's Modulus	80 GPa
Hardness (no post-processing)	110 HB, 115 HV, ≈65 HRB
Surface roughness (no post-processing)	R_a = 9 µm R_z = 15 µm

Table 23: Mechanical Porperties of DirectMetal 20 (EOS, 2004)

- **Thermal Properties**

Coefficient of thermal expansion	18 x 10^{-6} /K
Thermal conductivity	30 W/mK at 50 ºC
Maximum operating temperature	400 ºC

Table 24: Thermal properties of DirectMetal 20 (EOS, 2004)

Laser Sintering of DirectMetal 20

When Direct Metal 20 is exposed to the laser beam the low copper-phosphide powder works together with the bronze as a low melting point binding agent. This developing melted mass is used for curing (EOS, 2007b). According to EOS, the copper-phosphide powder has a lower melting point and acts as a binder, while the bronze powder has a higher melting point and acts as the structure, when Direct Metal 20 is exposed to the laser beam. This developing melted mass is used for curing (EOS, 2007b). When the powder is heated to a temperature greater than 660 ºC, the liquid phase wets the bronze and nickel particles as it enters the surrounding cavities. An expansion of the macroscopical powder volume occurs above 850 ºC as the pores and mixed crystals develop in the now variety of phases. This expansion compensates for the sintering shrinkage that occurred prior to this point (EOS, 2007b).